LA-11980-MS

Prompt Air Fluorescence Induced by a High-Altitude Nuclear Explosion

Los Alamos

Los Alamos National Laboratory is operated by the University of California for the United States Department of Energy under contract W-7405-ENG-36.

Edited by Marge Wilson, SST-DO

An Affirmative Action/Equal Opportunity Employer

LA-11980-MS

UC-700
Issued: December 1990

Prompt Air Fluorescence Induced by a High-Altitude Nuclear Explosion

Henry G. Horak
David G. Collins
Redus F. Holland
C. Dexter Sutherland

Los Alamos Los Alamos National Laboratory
Los Alamos,New Mexico 87545

CONTENTS

LIST OF FIGURES

LIST OF FIGURES (cont)

LIST OF FIGURES (cont)

LIST OF TABLES

PROMPT AIR FLUORESCENCE INDUCED BY A HIGH-ALTITUDE NUCLEAR EXPLOSION

by

**Henry G. Horak, Dave G. Collins,
Redus F. Holland, and C. Dexter Sutherland**

ABSTRACT

A high-altitude (>100 km) nuclear explosion emits a large fraction of its energy yield in the form of x rays, approximately half of which are deposited in the atmospheric layers ~50-90 km, exciting prompt fluorescence. This paper examines four of the N_2^+ first negative bands that fluoresce strongly: $\lambda\lambda$ 3914(0,0), 4278(0,1), 4709(0,2), and 5228(0,3) Å. We developed both "forward" and "backward" Monte Carlo procedures and performed calculations using Los Alamos CRAY computers to simulate the physical problem for the variety of situations that are possible. We include the time-dependent treatment of x-ray energy deposition, both local and nonlocal excitation of fluorescence, multiple scattering and transmission of fluorescent photons with the resulting enhancement of the longer wavelength N_2^+ bands, and chemical reactions. A realistic atmospheric model is defined up to 800 km, including the troposphere and a Lambert reflecting ground surface with given albedo. To expedite such computations we use separate spatial meshes in which to carry out the x-ray deposition and fluorescence light scattering. Examples of our calculated results illustrate the effects of explosion yield, geometry, tropospheric scattering, ground albedo, and temperature of the fluorescing layer. A subsequent paper will discuss the results obtained in a parametric study of x-ray source temperature.

I. INTRODUCTION

This report summarizes recent Monte Carlo studies of the prompt optical fluorescence emitted by the atmospheric layers in the vicinity of 80-km altitude caused by excitation from a high-altitude (>100 km) nuclear explosion. Emphasis is placed on four of the principal N_2^+ first negative bands that fluoresce strongly, namely $\lambda\lambda$ 3914, 4278, 4709, and 5228 Å.

Our work complements that of Bennett and Holland (1966) in the sense that we emphasize the time-dependent optical signal incident on earth-satellite detectors, whereas they considered only ground and aircraft observing stations and obtained only time-integrated results. Therefore, in order to simulate the various situations that can arise, we began anew and developed both "forward" and "backward" Monte Carlo procedures. All calculations were performed on Los Alamos National Laboratory CRAY computers.

Figures 1 and 2 show the geometry of the problem. Figure 1 shows x-ray photon paths (dashed lines) from the nuclear explosion source. Such photons are deposited primarily in the ~60-90-km layer, creating excited molecular and atomic species, electrons, and fluorescent photons; in particular, N_2^+ ions and the N_2^+ first negative emission bands. These fluorescent photons (solid lines) are scattered by N_2^+ ions within the deposition layer and also by elastic molecular and aerosol scattering at lower altitudes. Furthermore, the ground surface and clouds reflect a certain portion of these photons back into the fluorescing region. We assume that a satellite- or ground-based photometer with fast electronics measures the time history of the fluorescence seen within its field of view (FOV). Figure 2 shows the earth's center E, burst location B, burst zenith Z, and satellites S. The zenith angle, θ, of a satellite is defined relative to a point directly beneath the burst (the sub-burst point) on the earth's surface. The FOV of a satellite's photometer encompasses somewhat more than the earth's hemisphere, e.g., from a "stationary" orbit ($r \sim 6.6$ earth radii) the FOV is about 17.5° (0.0731 sr).

The x-ray energy deposition in the atmosphere can be readily calculated as a function of time and position if we know the yield, emission spectrum, and burst altitude of the nuclear device. We have elected to use the Los Alamos MCNP (Monte Carlo Neutron Photon) program (Briesmeister 1986) for this purpose because the x-ray absorption and scattering cross sections are continually updated and conveniently accessible, and because we have confidence in the MCNP code itself, which has evolved over many years of rigorous testing.

The mechanism of fluorescence is well understood, and most of the physical parameters of N_2^+ have been carefully measured in the laboratory. However, because of absorption by the N_2^+ itself, the optical thickness of the excited region can be large at some of the fluorescing wavelengths, resulting in multiple resonance-fluorescence scattering of the photons; this has the interesting effect of enhancing bands for which the region is "thin" at the expense of those for which it is "thick."

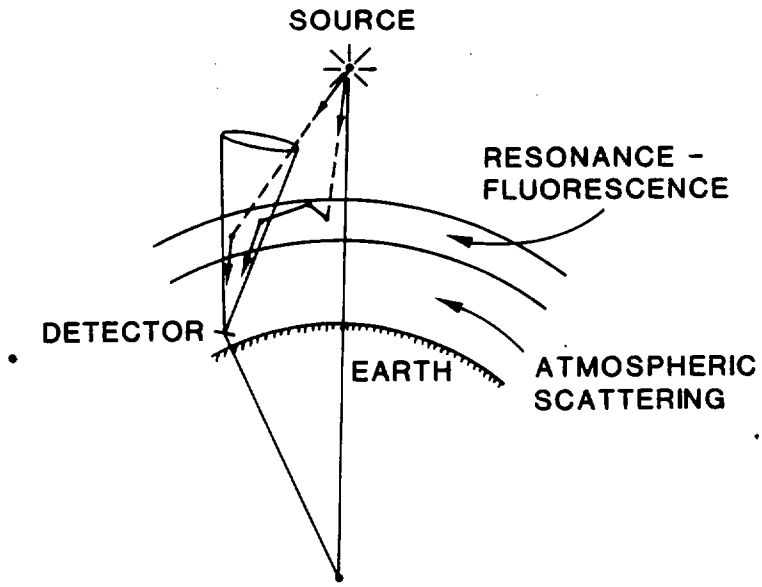

Fig. 1. The geometry of fluorescence for a detector close to the earth's surface.

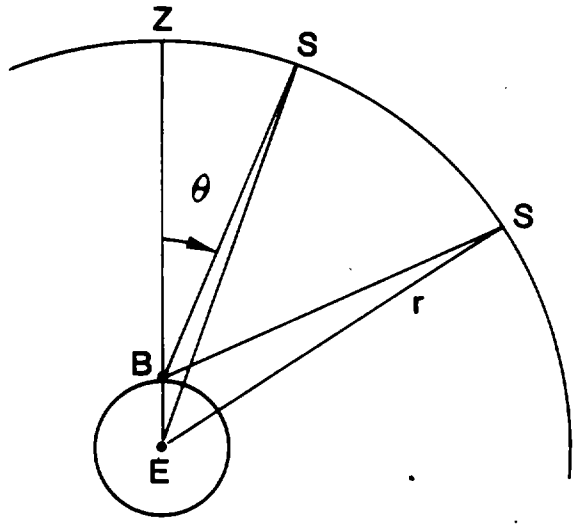

Fig. 2. The geometry of fluorescence for a satellite-borne detector.

The abundance of N_2^+ and the populations of its numerous energy states are time-varying quantities that depend upon kinetic chemical reactions and the changing radiation field, and we must determine the N_2^+ densities and populations of the absorbing levels. In air of normal composition, the initial N_2^+ concentration can be found approximately as one N_2^+ ion per 54.4 eV of x-ray energy deposited, though we use a more exact method in our computer program [see Eq. (1)]. The most important reactions removing N_2^+ are $N_2^+ + e \rightarrow N + N$ (dissociative recombination) and $N_2^+ + O_2 \rightarrow O_2^+ + N_2$ (charge transfer).

We designate the energy states of the N_2^+ ion by the letters X, V, J, where X represents the electronic state and V and J represent the vibrational and rotational quantum numbers, respectively. Transitions are indicated by the symbol "–" or a comma between quantum numbers for the initial and final states, with single primes on the letters for upper states and double primes for lower ($X'V'J' - X''V''J''$). Figure 3 is a schematic energy level diagram showing several vibrational levels and transitions of concern. The first negative (1N) emission bands are due to transitions of the type $B\,^2\Sigma_u^+(V' = 0) - X\,^2\Sigma_g^+(V'' = 0, 1, 2, \cdots)$ with $X' = B$, $X'' = X$; the Meinel bands are due to $A\,^2\Pi_u(V' = 0, 1, 2, \cdots) - X\,^2\Sigma_g^+(V'' = 0, 1, 2, \cdots)$ with $X' = A, X'' = X$.

The initial populations of the $N_2^+X(V'' = 0, 1, 2, 3)$ ground states are approximately in the ratios 0.662: 0.208: 0.077: 0.030, which are taken to be those produced by ionization of the N_2 by electrons, followed by emission in the N_2^+ first negative and Meinel transitions. These values are based on the laboratory measurements by Maier and Holland (1973), which indicate that the initial excitation of the $N_2^+X(V'')$ states from the ground state of $X(V = 0)$ of N_2 is primarily (57%) via the Meinel parent states $A(V')$. In time these ratios change because of charge-transfer deactivation with N_2, whereby $N_2^+X(V'' \geq 1) \rightarrow X(V'' = 0)$. Our calculations take into account this time-and-altitude effect. The populations above, corrected for vibrational deactivation, are used to derive $N_2^+(V'')$ column densities from which transmission values in desired spectral lines, branches, or bands are calculated whenever required during the run of the computer code. A somewhat more rigorous way of treating the V'' populations is described in Sec. III.B.2.

We also must calculate the emission in various lines and bands at given points in the fluorescing region. This is done by using experimental values of the fluorescence efficiency, η, which is defined by

$$\eta(V', V'') = \frac{\text{energy emitted by band } (V', V'')}{\text{x-ray energy deposited}}.$$

If we require the emission in a given rotational line, then we must multiply $\eta(V', V'')$ by a factor dependent on the temperature and the rotational quantum number [see Eq. (48)].

To simulate the multiple scattering of the lines, we have written programs based on both "forward" and "backward" Monte Carlo methods. The forward method follows representative photons from their creation in the medium through numerous scattering events; at each scattering point an estimate is made for each detector of the scattered contribution. The backward method follows representative photons in the reverse direction from the detector back to the source. In either application it is

necessary to choose properly the spectrum line emitted and allow for the possible change in the identity (wavelength) of the line at each scattering event. The time aspects are also important but can be handled with relative ease by the Monte Carlo method.

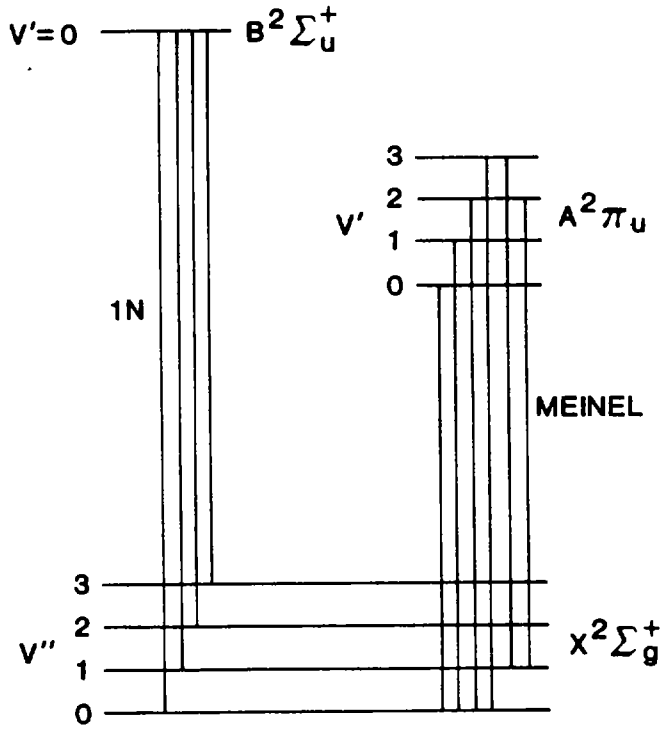

First Negative Bands	
V',V''	λ (Å)
0,0	3914
0,1	4278
0,2	4709
0,3	5228

Meinel Bands	
V',V''	λ (Å)
0,0	11 085
1,0	9179
2,0	7850
3,0	6872
3,1	8083
2,1	9471

Fig. 3. Schematic energy level diagram and wavelengths, λ, for some first negative and Meinel bands of N_2^+.

II. X-RAY DEPOSITION

A high-altitude nuclear explosion emits an angular distribution of x rays that we shall assume to be isotropic. If such a source is at an altitude higher than 800 km, the upper limit of the atmospheric model, then at least half the x rays are sent into space; the ratio of deposited to total x-ray energy is $\sim \Omega/4\pi$, where $\Omega = 2\pi(1 - \cos\theta)$, $\theta = \arcsin[7178/(6378 + h_B)]$, and $h_B(\geq 800)$ is the burst altitude (km).

A. X-Ray Source Spectrum

In *The Effects of Nuclear Weapons*, Glasstone (1962) writes: "Because of the enormous amount of energy liberated per unit mass in a nuclear weapon, very high temperatures are attained. These are estimated to be several tens of million degrees...". Such temperatures are as high as those found in star interiors, and for this report we shall assume a bomb temperature $\sim$ 20 000 000 K. The corresponding blackbody spectrum is shown in Fig. 4, where the abscissa ν is radiation frequency (Hz) and the ordinate is $\pi B_\nu/\pi B$ (Hz^{-1}); here πB_ν is the source emissive power per unit area per unit frequency interval given by Planck's equation, and $\pi B = \sigma\ \mathrm{T}^4$ (Stefan-Boltzmann) is the frequency-integrated emissive power per unit area.

B. Atmospheric Model, X-Ray Cross Sections, and Structure Factors

The air absorbs and scatters x-ray photons emitted by a nuclear explosion. To calculate the energy deposition, the initial number-density of N_2^+, and the optical source emissions in the first negative bands, it is necessary to use an atmospheric model combined with reliable x-ray photon cross-section and structure-factor data. The altitude profiles of temperature, pressure, density, and chemical species are obtained for h = 0-30 km from the US Standard Atmosphere (1962), for h = 30-80 km from the CIRA (Cospar International Atmosphere) 1965 Mean Reference Atmosphere (Cospar 1965), and for h = 120-800 km from the CIRA 1965 Model 5 Hour 8 (appropriate for a mean level of solar activity). The cross sections and structure factors are taken from the MCNP data base (Briesmeister, 1986) and the report by Livesay (1975); the latter contains data from 10 eV to 1 keV not usually found in similar tabulations. For photon energies above 1 keV, the Livesay data are very close to those given by MCNP.

C. Monte Carlo Program: MCNP

Because the x-ray temperature of an ordinary nuclear explosion is a few tens of million degrees Kelvin, the deposition is dominated by photoelectric absorption, which can be calculated by elementary methods. However, we have utilized the Monte Carlo program MCNP primarily because all the cross sections are readily available. The most recent version of MCNP is listed and discussed in the report by Briesmeister (1986). The program can be applied to a variety of geometries.

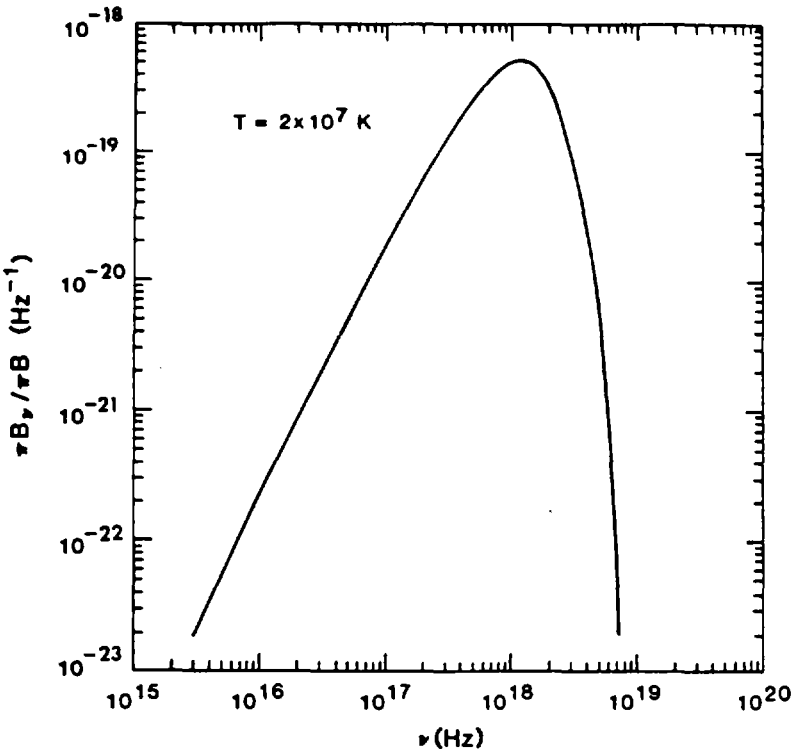

Fig. 4. Blackbody emission spectrum for 20 000 000 K.

1. Atmospheric Zones. To facilitate calculating x-ray deposition, the atmosphere is partitioned into spherical shells whose boundary surfaces are centered at the center of the earth. Within each shell the atmospheric properties are assumed constant. For altitudes h from 0-120 km, the thickness of each shell $\Delta h = 1$ km, for h = 120-130 km, $\Delta h = 10$ km, and for h = 300-800 km, $\Delta h = 20$ km.

2. Forced X-Ray Energy Deposition. In some problems such as determining instrumental thresholds, the very early time behavior of the fluorescent signal is important. This signal originates near the burst in highly rarified air, and it is difficult to obtain satisfactory x-ray deposition results with the ordinary Monte Carlo method. However, with MCNP it is possible to use a procedure that "forces" x-ray energy deposition of a given fraction (say 3%) of the photons incident on those spherical shells above a certain assigned altitude and thereby enables reasonable statistics to be obtained. There is a related problem, however: the energy deposition above ~110 km cannot be considered local because the electrons created by the x rays can travel long distances while creating optical fluorescence. The situation and its resolution are discussed in Leopard *et al.* (1970) (refer to Sec. III.B.4).

3. Axial Symmetry. The x-ray deposition must in principle display axial symmetry with respect to the line joining the center of the earth to the burst because the atmospheric parameters vary only with altitude, and the burst is assumed to radiate x rays isotropically. We can exploit this in the Monte Carlo calculation by transforming each deposition point into a circle about the axis of symmetry, along whose circumference the energy is deposited uniformly (Fig. 5). This procedure smooths the x-ray energy deposition over the spatial volumes involved.

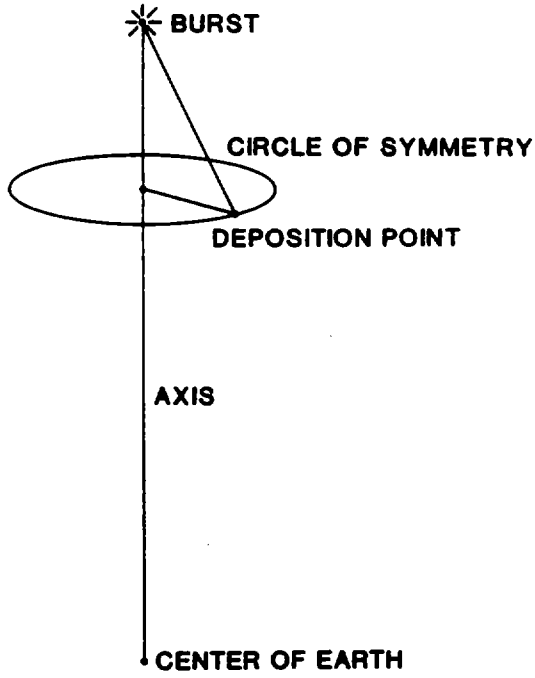

Fig. 5. Axial symmetry displayed by the x-ray deposition.

III. CREATION, EXCITATION, AND TIME VARIATION OF N_2^+

A. Production of N_2^+

Various molecules in the atmosphere are excited and ionized by electrons produced during the x-ray deposition phase of the explosion. The initial concentration of ionic species k is given by

$$n_k = [k] = \frac{E_x}{35}\left\{a(k,N_2)\frac{[N_2]}{[M]} + a(k,O_2)\frac{[O_2]}{[M]} + a(k,O)\frac{[O]}{[M]}\right\}, \tag{1}$$

where $a(k,N_2)$ is the fraction of the ions produced as species k due to interaction of x rays and concomitant electrons with N_2, $a(k,O_2)$ that due to interaction with O_2, and $a(k,O)$ that with O; $[N_2]$, $[O_2]$, and [O] are the ambient concentrations of these species; $[M] = [N_2] + [O_2] + [O]$, $E_x[eV]$ is the x-ray energy deposition/unit volume, and 35 eV is the average energy required per ion. At

altitudes below ~100 km, the concentrations of N_2^+ ions attained are very nearly those corresponding to an efficiency of one N_2^+ ion per 55 eV of x-ray energy deposited. Roughly 60% of all ions produced are N_2^+. For values of the production rates, refer to Myers and Schoonover (1976).

The N_2^+ ions undergo chemical reactions with the air, and consequently the N_2^+ concentration changes with time and altitude. Therefore, we must keep careful account of such variations in order to perform successful fluorescence calculations. In our computer program we use a special mesh, each cell of which has uniform physical properties. The cell boundaries are most conveniently chosen to be spheres and cones centered at the earth's center; consequently the cells are volumes of revolution possessing axial symmetry about the line from the center of the earth to the explosion.

B. Excitation of N_2^+

1. Fluorescence Efficiencies. The optical source emission for air excited by electrons is given in terms of the fluorescence efficiency, $\eta(\lambda)$, where λ is the wavelength of the band head and $\mathbf{p}$ is the air pressure at altitude h:

$$\eta(\lambda) = \frac{\text{energy/unit volume emitted in the band}}{\text{energy/unit volume deposited by electrons}} = \eta_o(\lambda)/(1 + K\mathbf{p} + C\mathbf{p}^2) \tag{2}$$

(Stern-Vollmer equation). The low-pressure efficiencies η_o and the air-quenching constants K and C are known (Mitchell 1970). Table I gives $\eta_o(\lambda)$ for the first negative bands of N_2^+. If $\mathbf{p}$ is expressed in torr (mm of Hg), then $K = 1.08$ and $C = 4.4 \times 10^{-4}$. The fraction of the emission that appears in each of the P, Q, R branches of a vibrational band, or, if required, in a single rotational line, can be found by applying appropriate factors (refer to Sec. IV.B.2).

TABLE I

FLUORESCENCE EFFICIENCIES FOR N_2^+ FIRST NEGATIVE BANDS

λ(Å)	V', V''	η_o
3914	0,0	0.0053
4278	0,1	0.00158
4709	0,2	0.00033
5228	0,3	5.6×10^{-5}

2. Production of Ground-State N_2^+. The energy level diagrams for N_2 and N_2^+ are shown in Fig. 6 (Gilmore 1964; Green and Wyatt 1965). The excitation of the vibrational levels of the ground state $X^2\Sigma_g^+$ ($V'' = 0, 1, \ldots$) of N_2^+ comes from (a) direct excitation from the ground state $X^1\Sigma_g^+$ of N_2, (b) indirect excitation via the Meinel parent state $A^2\Pi_u$ of N_2^+, and (c) indirect excitation from the

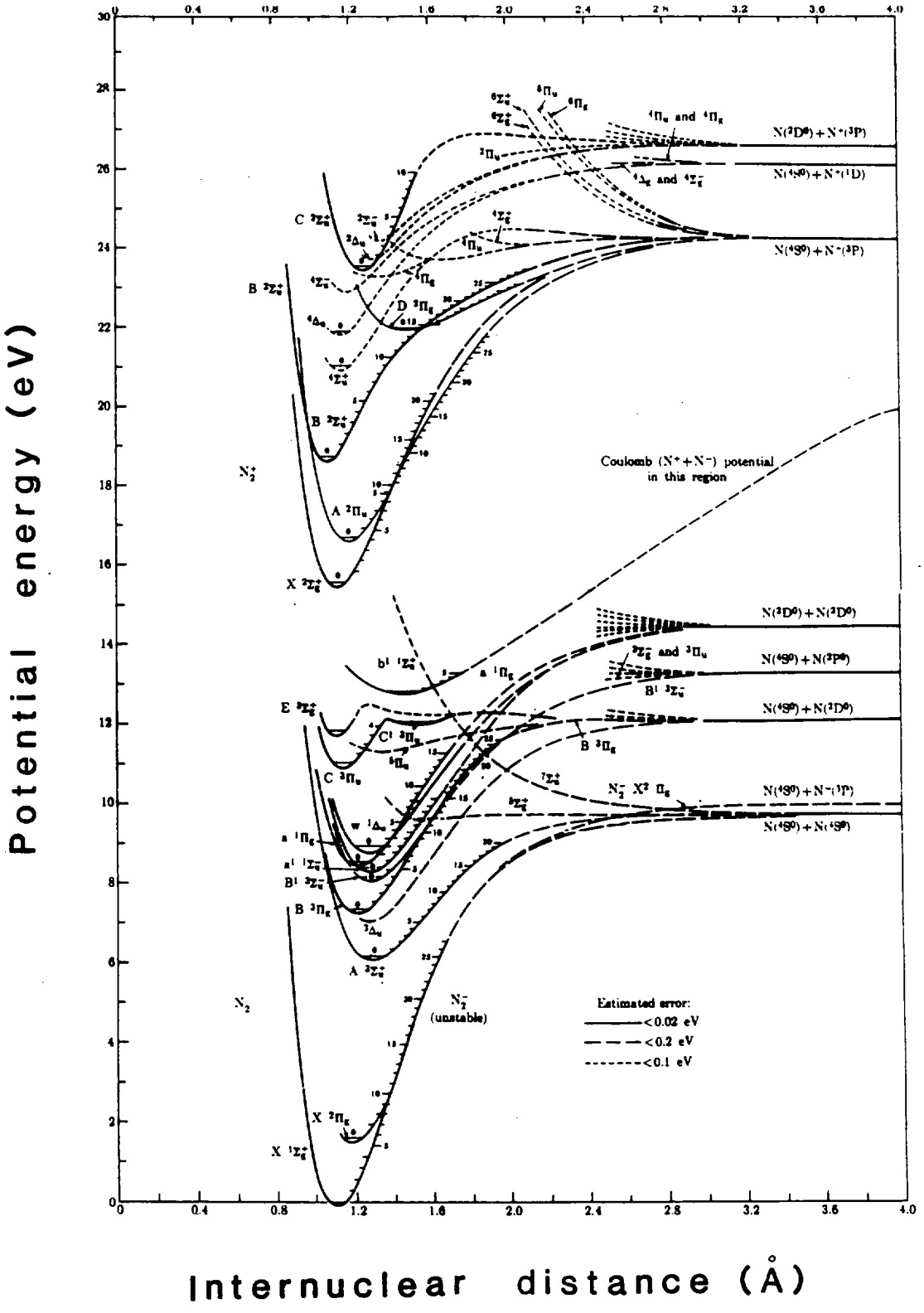

Fig. 6. Energy level diagrams for nitrogen molecules and ions.

$B^2\Sigma_u^+$ upper state of the N_2^+ first negative band. Contributions from other states such as the upper states of the N_2^+ second negative ($C^2\Sigma - X^2\Sigma$), the Janin-d'Incan bands ($D^2\Pi - A^2\Pi$), and the quartet states of N_2^+ are not significant. The initial populations can be related with some confidence to the total number of N_2^+ ions produced by energetic electrons in air. Based on populations of Maier and Holland (1973), and on earlier observations [see the "Erratum" by Holland and Maier (1973) and the paper to which it refers], we conclude that ~57% of the N_2^+ is initially in the Meinel parent A-state. Based on N_2^+ first negative efficiency measurements by Mitchell (1970), we estimate that ~14% of the N_2^+ is initially in the parent B-state of the first negative. We then assume that the remaining 29% of the N_2^+ is initially in the ground X-state.

The Franck-Condon factors $q(V, V'')$ for direct ionization of $N_2X(V = 0)$ to $N_2^+X(V'')$ (Nicholls 1961) are the following:

V''	=	0	1	2	3
$q(0, V'')$	=	0.902	0.0906	0.00651	0.000454

We take these to be the relative populations of the vibrational levels of the X-state of N_2^+ as a result of direct ionization.

The initial production of $N_2^+B^2\Sigma_u^+$ is followed by rapid first negative emission. To determine its contribution to the ground-state vibrational populations, we require relative probabilities for the excitation and subsequent radiative transitions. Stanton and St. John (1969) give relative populations $P(BV')$ for the initial ionization of N_2 to the $N_2^+B(V')$ states:

V'	=	0	1	2	3
$P(BV')_{t=0}$	=	0.885	0.103	0.0083	0.0036

Einstein coefficients $\mathbf{A}(V', V'')$ for the spontaneous N_2^+ first negative emission are given in Table II. Most of these values were derived by Skumanich and Stone (1960) from the lifetime of the $B^2\Sigma_u^+$ ($V' = 0$) level, 6.58×10^{-8} s, reported by Bennett and Dalby (1959), from the intensity measurements of Wallace (1954), and the resulting expression for the electronic transition moment R_e as a function of internuclear distance r (Wallace and Nicholls 1955):

$$R_e(r) = const[10.134r^2 - 23.49r + 14.473].$$

Shemansky and Broadfoot (1971) obtained slightly different $\mathbf{A}(V', V'')$ from this expression and the same lifetime. They used different Franck-Condon factors than those used by Wallace and Nicholls in deriving the expression and so may have introduced a small error. The $\mathbf{A}(V', V'')$ given by Jain and Sahni (1967), also based on Wallace's data but on their own Franck-Condon factors and $R_e(r)$, have relative values in better agreement with the $\mathbf{A}(V', V'')$ of Skumanich and Stone, but utilized lifetimes of Jeunehomme (1966), which are too high. Numbers in brackets in Table II are based on relative values of Jain and Sahni, but we have altered their absolute magnitude to be consistent with the lifetimes

TABLE II

BAND HEAD WAVELENGTHS, λ, BRANCHING RATIOS, b, AND EINSTEIN EMISSION COEFFICIENTS, A, FOR THE N_2^+ FIRST NEGATIVE BANDS

V'	V''	$\lambda(V',V'')$ (Å)	$b(V',V'')^{a,b}$	$\mathbf{A}(V',V'')^{a,c}$ (10^7 s^{-1})
0	0	3914	0.7050	1.071
	1	4278	0.2304	0.350
	2	4709	0.0529	0.0804
	3	5228	0.0099	0.0150
	4		0.0016	0.0024
	5		[0.0002]	[0.0003]
1	0	3582	0.3309	0.534
	1	3884	0.2794	0.451
	2	4236	0.2577	0.416
	3	4651	0.0991	0.160
	4	5148	0.0260	0.042
	5		[0.0056]	[0.009]
2	0	3308	0.0706	0.118
	1	3564	0.4545	0.760
	2	3858	0.0736	0.123
	3	4199	0.2183	0.365
	4	4599	0.1316	0.220
	5	5076	0.0514	0.086
3	0		[0.0024]	[0.004]
	1		0.1740	0.293
	2		0.4869	0.820
	3		[0.0030]	[0.005]
	4		[0.1663]	[0.280]
	5		[0.1675]	[0.282]

[a] Quantities in brackets derived from Jain and Sahni (1967).

[b] $b(V',V'') = \mathbf{A}(V',V'')/\sum_{V''} \mathbf{A}(V',V'')$.

[c] Skumanich and Stone (1960).

of Bennett and Dalby. The initial first negative emission produces a contribution to the $N_2^+ X(V'')$ relative populations

$$P_B(XV'') = \sum_{V'} b(V', V'') P(BV'),$$

and

V''	=	0	1	2	3	4	5
$P_B(XV'')_{t=0}$	=	0.659	0.237	0.076	0.021	0.006	0.002

At early times after the first negative emission, but before any appreciable contribution from the longer-lived Meinel A-states, and ignoring early quenching or vibrational deactivation, the fractions of the *total* N_2^+ in the $X(V'')$ states are

V''	=	0	1	2	3	4	5
$P(XV'')_{t=0}$	=	0.354	0.0595	0.0125	0.0030	0.0008	0.0003

These populations were obtained by multiplying relative values for the direct ionization and B-state excitation by 0.29 and 0.14, respectively, and adding. The corresponding densities of N_2^+ in the $X(V'')$ vibrational states are $[X(V'')]_{t=0} = P(XV'')_{t=0}[N_2^+]_{t=0}$.

The relative populations $P(AV')$ for excitation to the $A(V')$ vibration states by energetic electrons are given by Maier and Holland (1973):

V'	=	0	1	2	3	4	5	6	7	8
$P(AV')$	=	0.2384	0.3027	0.2195	0.1159	0.0599	0.0259	0.0122	0.0069	0.0040

The initial populations are therefore given by

$$[A(V')]_{t=0} = 0.57 P(AV')_{t=0}[N_2^+]_{t=0}.$$

Branching ratios for emission in the Meinel bands are given in Table III (Maier and Holland 1973). They permit a calculation of the Meinel emission contribution to the ground-state vibrational populations. The relative values obtained from the populations $P(AV')$ and ratios $b(V', V'')$ are

V''	=	0	1	2	3	4	5	6	7
$P_A(XV'')$	=	0.5402	0.2604	0.1127	0.0472	0.0193	0.0081	0.0060	0.0023

When these values are multiplied by 0.57 and added to those previously obtained for the direct ionization and N_2^+ first negative emission, we obtain, for the levels of greatest interest

V''	=	0	1	2	3	4
$P(XV'')$	=	0.6617	0.2078	0.0767	0.0299	0.0118

These values approximate the vibrational populations in the ground state produced by direct ionization and by subsequent emission in the N_2^+ first negative and Meinel systems.

TABLE III

WAVELENGTHS, λ, LIFETIMES, τ, BRANCHING RATIOS, b, AND EINSTEIN EMISSION COEFFICIENTS, A, FOR THE MEINEL BAND SYSTEM OF N_2^+

V'	V''	λ(Å)	$\tau(V')(\mu s)$	$b(V',V'')$	$A(V',V'')(10^4\,s^{-1})$
0	0	11 090.9	16.97	0.7544	4.445
	1	14 616.5		0.2251	1.326
	2	21 279.3		0.0199	0.117
	3	38 610.0		0.0005	0.003
1	0	9182.9	14.22	0.7684	5.404
	1	11 474.5		0.0482	0.339
	2	15 214.2		0.1543	1.085
	3	22 404.4		0.0283	0.199
	4	41 893.6		0.0009	0.006
2	0	7853.5	12.33	0.4496	3.646
	1	9471.1		0.4418	3.583
	2	1181.8		0.0133	0.108
	3	15 855.9		0.0678	0.550
	4	23 638.4		0.0264	0.214
	5	45 718.5		0.0011	0.009
3	0	6874.4	10.94	0.2024	1.850
	1	8082.9		0.5543	5.063
	2	9775.5		0.1331	1.235
	3	12 315.0		0.0680	0.622
	4	16 545.9		0.0190	0.174
	5	24 995.6		0.0199	0.182
	6	30 221.0		0.0012	0.011
4	0	6123.7	9.91	0.0787	0.794
	1	7064.5		0.3957	3.993
	2	8324.3		0.4117	4.154
	3	10 097.3		0.0122	0.123
	4	12 776.0		0.0861	0.869
	5	17 288.8		0.0017	0.017
	6	26 492.9		0.0128	0.129
	7	55 589.5		0.0011	0.011

TABLE III (cont)

V'	V''	λ(Å)	$\tau(V')(\mu s)$	$b(V',V'')$	$\mathbf{A}(V',V'')(10^4\,\mathrm{s}^{-1})$
5	0	5529.9	9.08	0.0273	0.301
	1	6285.9		0.2148	2.362
	2	7264.1		0.4597	5.063
	3	8578.5		0.2148	2.366
	4	10 437.8		0.0052	0.057
	5	13 267.0		0.0696	0.767
	6	18 089.7		0.0007	0.008
	7	28 150.8		0.0071	0.078
	8	62 081.0		0.0008	0.009
6	0	5048.8	8.45	0.0092	0.109
	1	5671.5		0.0966	1.143
	2	6455.9		0.3388	4.009
	3	7473.6		0.3965	4.692
	4	8846.4		0.0730	0.864
	5	10 798.1		0.0353	0.418
	6	13 790.4		0.0420	0.497
	7	18 954.8		0.0047	0.056
	8	29 992.2		0.0033	0.039
	9	70 062.4		0.0005	0.006
7	0	4651.1	7.93	0.0031	0.039
	1	5174.5		0.0397	0.501
	2	5819.6		0.1945	2.453
	3	6634.0		0.3972	5.009
	4	7693.8		0.2698	3.402
	5	9128.8		0.0097	0.122
	6	11 179.7		0.0577	0.728
	7	14 349.1		0.0186	0.235
	8	19 890.2		0.0082	0.103
	9	32 044.1		0.0012	0.015
	10	80 083.3		0.0004	0.005

TABLE III (cont)

V'	V''	λ(Å)	$\tau(V')(\mu s)$	$b(V',V'')$	$\mathbf{A}(V',V'')(10^4\,\mathrm{s}^{-1})$
8	0	4317.1	7.50	0.0010	0.013
	1	4764.4		0.0156	0.208
	2	5306.0		0.0964	1.285
	3	5974.7		0.2893	3.856
	4	6820.9		0.3774	5.031
	5	7925.4		0.1428	1.903
	6	9426.7		0.0017	0.023
	7	11 584.1		0.0609	0.812
	8	14 945.4		0.0050	0.067
	9	20 902.6		0.0094	0.125
	10	34 339.5		0.0003	0.004
9	0	4032.7	7.12	0.0003	0.004
	1	4420.4		0.0059	0.083
	2	4882.8		0.0441	0.619
	3	5443.5		0.1709	2.400
	4	6137.2		0.3485	4.895
	5	7017.0		0.3022	4.244
	6	8168.9		0.0528	0.742
	7	9741.0		0.0200	0.281
	8	12 012.9		0.0496	0.697
	9	15 582.4		0.0003	0.004
	10	21 999.8		0.0085	0.119
10	1	4128.7	6.83	0.0022	0.032
	2	4528.3		0.0193	0.283
	3	5006.5		0.0908	1.329
	4	5587.3		0.2464	3.607
	5	6307.4		0.3538	5.180
	6	7222.8		0.1998	2.925
	7	8425.1		0.0092	0.135
	8	10 072.7		0.0394	0.577
	9	12 467.4		0.0320	0.468
	10	16 263.1		0.0006	0.009
	11	23 190.0		0.0066	0.087

The Meinel emission takes $\lesssim$10-17 μs, which permits some time for photons to move 3-5 km and also strong deactivation of the Meinel parent state ($A^2\Pi_u$) below ~80 km. It may eventually be possible to include the time dependence due to the Meinel emission and deactivation, just as effects of the vibrational deactivation due to charge transfer with N_2^+ are presently included.

The question of the time decay of the N_2^+ concentration itself is discussed in Sec. III.B.3. Here we will briefly discuss the vibrational population changes of $N_2^+X(V'')$ that are due to the following:

$$N_2^+X(V''\geq 1)+N_2 \rightarrow N_2+N_2^+X(V''=0), \tag{3}$$

$$N_2^+A(V')+M \rightarrow M+N_2^+X(V''), \tag{4}$$

$$N_2^+A(V')-h\nu(AV',XV'') \rightarrow N_2^+X(V''). \tag{5}$$

(M represents an air molecule.)

Provided we ignore the population changes due to resonance scattering, the following equations hold:

$$\frac{d}{dt}[X(V''>0)] = -\alpha(V'')[N_2][X(V''>0)] + \sum_{V'}\mathbf{A}(AV',V'')[A(V')] + \mathbf{C}(AV',V'')[A(V')][M], \tag{6}$$

$$\frac{d}{dt}[X(V''=0)] = \sum_{V''>0}\alpha(V'')[N_2][X(V''>0)] + \sum_{V'}\mathbf{A}(AV',V''=0)[A(V')] + \mathbf{C}(AV',V''=0)[A(V')][M]; \tag{7}$$

where

$[X(V'')]$ is the number density of $N_2^+X(V'')$,

$[N_2]$ is the ambient N_2 number density,

$[M]$ is the ambient air number density,

$[A(V')]$ is the number density of $N_2^+A(V')$,

$\alpha(V'')$ is the rate for deactivation of the $N_2^+X(V'')$ state by charge transfer with N_2,

$\mathbf{A}(AV',V'')$ is the Einstein spontaneous-emission coefficient for the transition $A(V')\rightarrow X(V'')$, and

$\mathbf{C}(AV',V'')$ is the rate constant for collisional deactivation in the transition $A(V')\rightarrow X(V'')$.

The sum $\Sigma_{V''}\mathbf{A}(AV',V'') = 1/\tau(V')$, where $\tau(V')$ is the radiative lifetime of the state $A(V')$. The sum $\sum_{V''}\mathbf{C}(AV',V'') = \mathbf{C}(V')$ is the rate constant for collisional deactivation of the state $A(V')$.

The numerical values of various quantities are given in Table III (Maier and Holland 1973). The $b(V',V'')$ are branching ratios for emission in the Meinel vibrational bands. Values of $[N_2]$ and $[M]$ are given in tables of atmospheric models (US Standard Atmosphere 1962, Cospar 1965). Charge-transfer vibrational deactivation rates are given by Fox and Dalgarno (1985): $\alpha(V'' = 1) = 6 \times 10^{-10}\,\mathrm{cm}^3/\mathrm{s}$, $\alpha(V'' > 1) = 2 \times 10^{-10}\,\mathrm{cm}^3/\mathrm{s}$.

The deactivation branching rates, $\mathbf{C}(V',V'')$, are not presently known; however, the rates $\mathbf{C}(V')$ for deactivation of the upper states by N_2 and O_2 have been estimated by Cartwright *et al.* (1975) from quenching coefficients and lifetimes and can be expressed reasonably well for normal air by

$$\mathbf{C}(V') = \sum_{V''}\mathbf{C}(AV',V'') \doteq (5 + V') \times 10^{-10}\,\mathrm{cm}^3/\mathrm{s} \tag{8}$$

(our approximation for the Cartwright *et al.* data).

Vibrational populations of the Meinel parent state can be expressed as an explicit function of time:

$$\begin{aligned}\frac{d[A(V')]}{dt} = &-\sum_{V''}\mathbf{A}(AV',V'')[A(V')] \\ &- \mathbf{C}(AV',V'')[A(V')][M],\end{aligned} \tag{9}$$

whence

$$[A(V')] = [A(V')]_{t=0}\,\exp -\left\{\frac{1}{\tau(V')} + [M]\mathbf{C}(V')\right\} t. \tag{10}$$

Putting this into Eqs. (6) and (7) gives

$$\begin{aligned}\frac{d[X(V'' > 0)]}{dt} = &-\alpha(V'')[N_2]\,[X(V'' > 0)] \\ &+ \sum_{V'}[A(V')]_{t=0}\,\{\mathbf{A}(AV',V'') + \mathbf{C}(AV',V'')[M]\} \\ &\times \exp -\left\{\frac{1}{\tau(V')} + [M]\mathbf{C}(V')\right\} t,\end{aligned} \tag{11}$$

and

$$\begin{aligned}\frac{d[X(V'' = 0)]}{dt} = &\sum_{V''>0}\alpha(V')[N_2]\,[X(V'' > 0)] \\ &+ \sum_{V'}[A(V')]_{t=0}\,\{\mathbf{A}(AV',V'') + \mathbf{C}(AV',V'')[M]\} \\ &\times \exp -\left\{\frac{1}{\tau(V')} + [M]\mathbf{C}(V')\right\} t.\end{aligned} \tag{12}$$

These equations need to be solved simultaneously with the chemical rate equations (refer to the following section and Table V).

Unfortunately, as mentioned above, the branching ratios $C(AV', V'')$ for the collisional deactivation of the $A(V')$ states to produce $X(V'')$ levels are unknown. A possible set of dummy parameters to permit a rough assessment of the effect of the Meinel collisional deactivation are the Franck-Condon factors for the A to X transitions (Table IV); they probably are a factor in the effect but may not represent the $C(AV', V'')$ even approximately.

We have usually performed the fluorescence calculations by the simple method in which the effect of the Meinel system on the X-state populations was allowed for only as emission in producing the initial conditions, namely $P(V'' = 0) = 0.6617$; $P(V'' = 1) = 0.2078$; $P(V'' = 2) = 0.0767$; and $P(V'' = 3) = 0.0299$. This implies ~57% of the N_2^+ ground-state vibrational excitation takes place via Meinel emission, ~29% by direct excitation, and ~14% from the upper states of N_2^+ first negative bands. The rest of the computation was then carried out without reference to the Meinel system. Refer to the remarks at the beginning of Chap. IV.

3. Chemical Reactions Relevant to N_2^+. Several chemical reactions take place after the initial deposition and formation of ions that affect the abundance of N_2^+ and/or the population distribution of its energy states. These reactions are listed in Table V, along with values of the reaction rate constants (Bortner and Baurer 1978).

The initial concentration of N_2^+ and other chemical species, and the relative populations in the A- and X-vibration states, are assumed known. The appropriate simultaneous set of differential equations can be readily written down, but their solution requires special techniques applicable to "stiff" equations. It is not our object to discuss these techniques; they are well treated by Gear (1971) and Shampine and Gear (1976).

4. Transport of Electrons. At altitudes above ~100 km, the electron ranges can become significantly large so that the x-ray energy deposition no longer determines local production and excitation of N_2^+. Table VI gives electron ranges vs altitude for electron energies of 1 and 4 keV. The preponderance of the deposition takes place below 100 km where the excitation is essentially local.

A discussion of the method we used for calculating nonlocal, time-dependent electron energy deposition is given in a report by Leopard *et al.* (1970). The erratic motion of the electron and the presence of the earth's magnetic field complicate the problem. Quoting from the report:

> "The mathematical model selected ... assumes that the x-ray energy lost ... is given up in whole or part to an ejected primary electron. At each x-ray collision,

TABLE IV

FRANCK-CONDON FACTORS FOR THE MEINEL BANDS[a]

V'	V''	$q(V', V'')$
0	0	0.49718
	1	0.37090
	2	0.11218
	3	0.01799
1	0	0.31927
	1	0.43299
	2	0.34775
	3	0.22553
	4	0.05660
2	0	0.12647
	1	0.23616
	2	0.01459
	3	0.20365
	4	0.29002
	5	0.10950
3	0	0.04069
	1	0.19431
	2	0.09131
	3	0.09703
	4	0.07506
	5	0.29574
	6	0.16660
4	0	0.01184
	1	0.09678
	2	0.17682
	3	0.01059
	4	0.15489
	5	0.00924
	6	0.25512
	7	0.21780
5	0	0.00329
	1	0.03837
	2	0.13484
	3	0.11205
	4	0.00517
	5	0.15584
	6	0.00377
	7	0.18932
	8	0.25536

TABLE IV (cont)

V'	V''	$q(V',V'')$
6	0	0.00090
	1	0.01353
	2	0.07138
	3	0.13846
	4	0.04602
	5	0.04159
	6	0.11568
	7	0.03528
	8	0.11916
7	0	0.00025
	1	0.00450
	2	0.00314
	3	0.09814
	4	0.11136
	5	0.00709
	6	0.08241
	7	0.06310
	8	0.07767
	9	0.06008
8	3	0.05340
	4	0.10875
	5	0.06940
	6	0.00145
	7	0.10427
	8	0.02129
	9	0.11158

[a] Albritton *et al.* (1972).

the initial direction and kinetic energy are obtained from a knowledge of the incident photon direction, the type of collision that has occurred, and the amount of energy lost by the incident photon. The primary electron and subsequent secondary electrons thereafter dissipate energy by excitation and ionization of the air as they migrate through the atmosphere. The amount of energy given up along the transport path is calculated as a function of position and time from a continuous slowing down model based on the range-energy data of Berger and Seltzer (1964), and the electron energy dissipation data of Spencer (1959)."

TABLE V

CHEMICAL REACTIONS RELEVANT TO N_2^+ [a]

Reaction	Reaction Rate ($cm^3 \cdot s^{-1}$)
$N_2^+ + e \rightarrow N + N$	$1.8 \times 10^{-7}(300/T)^{.4}$
$O_2^+ + e \rightarrow O + O$	$2.1 \times 10^{-7}\ (300/T)^{.6}$
$NO^+ + e \rightarrow N + O$	$4.0 \times 10^{-7}\ (300/T)$
$N_2^+ + O_2 \rightarrow N_2 + O_2^+$	$5.0 \times 10^{-11}\ (300/T)^{.8}$
$N_2^+ + O \rightarrow N + NO^+$	$1.3 \times 10^{-10}\ (300/T)^{.5}$
$N_2^+ + O \rightarrow N_2 + O^+$	$1.0 \times 10^{-11}\ (300/T)^{.2}$
$N_2 + O^+ \rightarrow N + NO^+$	$1.2 \times 10^{-12}\ (300/T)$
$N_2^+(X, V'' \geq 1) + N_2 \rightarrow N_2^+(X, V'' = 0) + N_2$	4.0×10^{-10}
$N_2^+(B) + N_2 \rightarrow N_2^+(X) + N_2$ $N_2^+(B) + O_2 \rightarrow N_2^+(X) + O_2$	5.0×10^{-10}
$N_2^+(A) + N_2 \rightarrow N_2^+(X) + N_2$ $N_2^+(A) + O_2 \rightarrow N_2^+(X) + O_2$	$(5.0 + V') \times 10^{-10}$

[a] Bortner and Baurer (1978).

TABLE VI

ELECTRON RANGES IN AIR

Altitude (km)	Air Density (g/cm^3)	Range (km)	
		1 keV	4 keV
120	2.490×10^{-11}	2	24
150	2.176×10^{-12}	23	275
180	5.283×10^{-13}	95	1136
210	1.857×10^{-14}	269	3231

We shall restrict the discussion to photoelectric absorption and the applicable equations. Figure 7 shows the basic rectangular coordinate frame $\vec{i}$, $\vec{j}$, $\vec{k}$ at the center of the earth with unit vector $\vec{k}$ directed toward the burst; $\vec{j}$ is assumed to be located in the plane that contains the detector, and $\vec{i} = \vec{j} \times \vec{k}$. The position vector of the collision point between an x ray and an air molecule is given by

$$\vec{r} = x\vec{i} + y\vec{j} + z\vec{k} = r\sin\theta\cos\phi\vec{i} + r\sin\theta\sin\phi\vec{j} + r\cos\theta\vec{k}, \tag{13}$$

where x, y, z are rectangular and r, θ, ϕ polar coordinates, and we define $\vec{R} = \vec{r}/r$. Also, we shall let $\vec{X}$ be the direction the x ray is moving before collision and $\vec{e}$ the direction of motion of the primary electron produced by the interaction. We require $\vec{R}$, $\vec{X}$, $\vec{e}$ to be unit vectors. The angles Θ and Φ are assumed given by the circumstances of the collision; the manner of obtaining their values will be discussed later.

The geometrical problem is to find $\vec{e}$, given $\vec{R}$, $\vec{X}$, $\Theta(0 \leq \Theta \leq 180°)$ and $\Phi(0 \leq \Phi \leq 360°)$. (Refer to Fig. 8.) $\vec{e}$ is a linear combination of $\vec{R}, \vec{X}, \vec{R} \times \vec{X}$, namely

$$\vec{e} = A\vec{R} + B\vec{X} + C\vec{R} \times \vec{X}. \tag{14}$$

We shall express A, B, C in terms of the known angles Θ, Γ, Φ by spherical trigonometry or vectorial methods. It can be shown that

$$\begin{aligned} A &= (n \sin\Gamma - \ell \cos\Gamma)/\sin\Gamma, \\ B &= \ell/\sin\Gamma, \\ C &= m/\sin\Gamma, \end{aligned}$$

where ℓ, m, n are direction cosines of $\vec{e}$ relative to $\vec{I}, \vec{J}, \vec{R}$ given by

$$\begin{aligned} \ell &= \cos\Theta \sin\Gamma - \sin\Theta \cos\Gamma \cos\Phi, \\ m &= \sin\Theta \sin\Phi, \\ n &= \cos\Theta \cos\Gamma + \sin\Theta \sin\Gamma \cos\Phi. \end{aligned}$$

It remains to express $\vec{R}, \vec{X}$, and $\vec{e}$ in terms of $\vec{i}, \vec{j}, \vec{k}$:

$$\begin{aligned} \vec{R} &= R_1\vec{i} + R_2\vec{j} + R_3\vec{k}; \\ \vec{X} &= \vec{x}/\mid \vec{x} \mid = X_1\vec{i} + X_2\vec{j} + X_3\vec{k}, \end{aligned}$$

where

$$\begin{aligned} \vec{x} &= r\vec{R} - r_B\vec{k} = rR_1\vec{i} + rR_2\vec{j} + (rR_3 - r_B)\vec{k} \\ &= x_1\vec{i} + x_2\vec{j} + x_3\vec{k} \\ |\vec{x}| &= \sqrt{x_1^2 + x_2^2 + x_3^3}, \quad r_B = r_E + h_B \end{aligned}$$

and

$$\begin{aligned} \vec{R} \times \vec{X} &= (R_2X_3 - R_3X_2)\vec{i} + (R_3X_1 - R_1X_3)\vec{j} \\ &\quad + (R_1X_2 - R_2X_1)\vec{k}, \end{aligned}$$

with

$$|\vec{R} \times \vec{X}| = \sin\Gamma.$$

It follows that

$$\vec{e} = e_1\vec{i} + e_2\vec{j} + e_3\vec{k}, \tag{15}$$

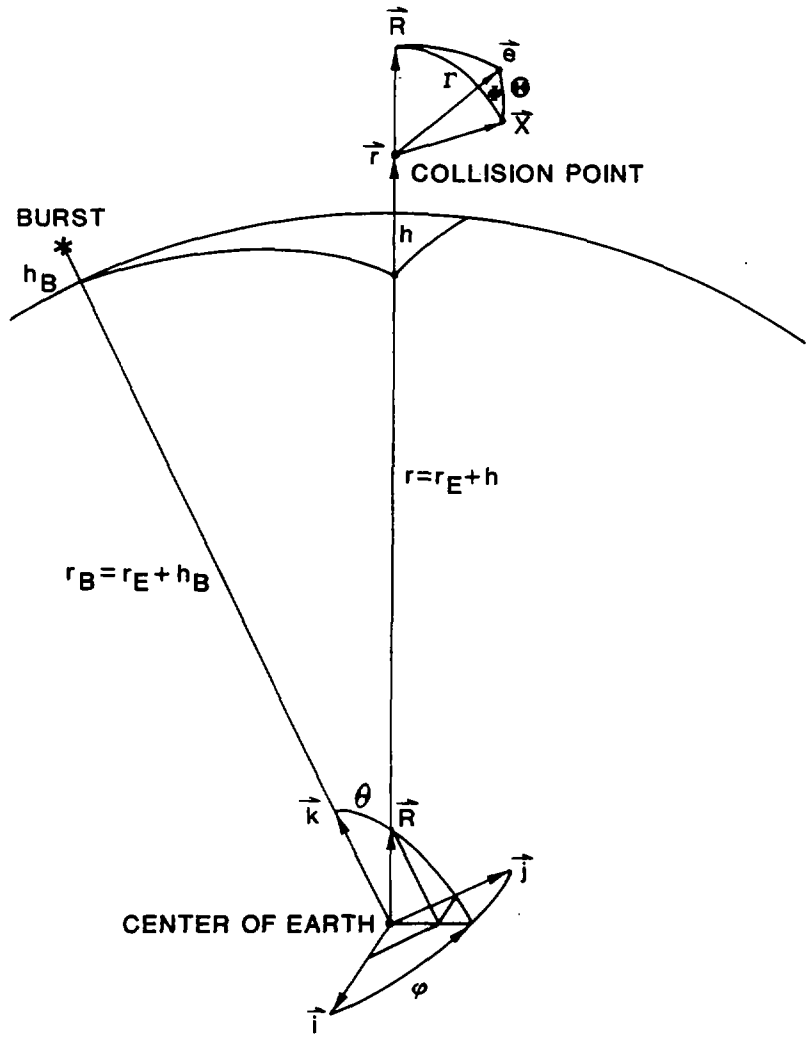

Fig. 7. Geometry of an x-ray-molecule interaction where the origin is the center of the earth. $\vec{R}$ is the radial unit vector, $\vec{X}$ is the unit vector in the direction of x-ray motion, and $\vec{e}$ is the direction of motion of the resultant electron. Angles Θ, Γ, Φ are known from the circumstances of the interaction.

where

$$e_1 = AR_1 + BX_1 + C(R_2X_3 - R_3X_2),$$
$$e_2 = AR_2 + BX_2 + C(R_3X_1 - R_1X_3),$$
$$e_3 = AR_3 + BX_3 + C(R_1X_2 - R_2X_1).$$

The angles Θ and Φ can be calculated by a Monte Carlo sampling technique. The angular function $q(\Theta,\Phi)$ for the probability of electron emission into a given direction depends upon the energy, and

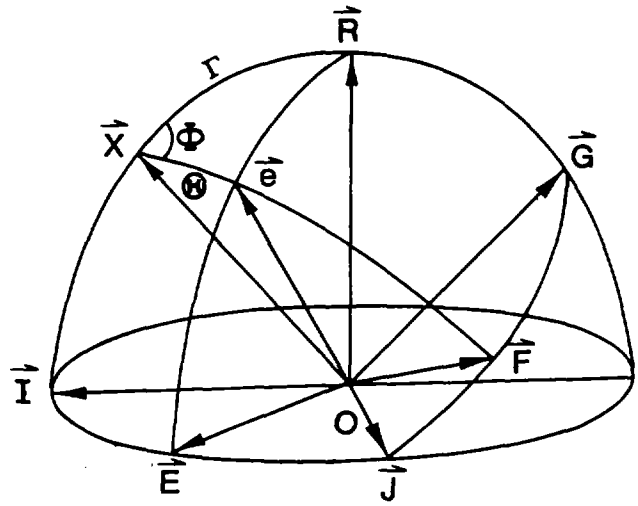

Fig. 8. Geometry of an x-ray-molecule interaction where the origin O is the interaction point and $\vec{I}$, $\vec{J}$, $\vec{R}$ is an auxiliary orthogonal reference triad.

as the energy increases, the function becomes more peaked in the forward direction. The simplest formula, applicable to low energies $\left(\beta = \frac{v}{c} \ll 1\right)$, is

$$q_1(\Theta,\Phi) = K_1 \sin^2 \Theta \cos^2 \Phi. \tag{16}$$

Neglecting relativity and spin, Fischer (1931) derived

$$q_2(\beta;\Theta,\Phi) = K_2 \sin^2 \Theta \cos^2 \Phi / \left[1 + \left(E/2m_e c^2\right) - \beta \cos \Theta\right]^4; \tag{17}$$

and a more rigorous relativistic expression for high energies was derived by Sauter (1931):

$$\begin{aligned} q_3(\beta;\Theta,\Phi) &= K_3 \beta^2 \sin^2 \Theta \\ &\left\{ \frac{1-\beta^2)^{1/2} \cos^2 \Phi}{(1-\beta\cos\Theta)^4} - \frac{\left[1-(1-\beta^2)^{1/2}\right]\cos^2\Phi}{2(1-\beta^2)^{1/2}(1-\beta\cos\Theta)^3} \right. \\ &\left. + \frac{\left[1-(1-\beta^2)^{1/2}\right]^2}{4(1-\beta^2)(1-\beta\cos\Theta)^3} \right\} (\beta \sim 1), \end{aligned} \tag{18}$$

where

$$\beta = \frac{\left[\frac{E}{m_e c^2}\left(\frac{E}{m_e c^2}+2\right)\right]^{1/2}}{\left(\frac{E}{m_e c^2}+1\right)},$$

and E is the kinetic energy and m_e the mass of the electron. E is obtained by taking the amount of x-ray energy deposition $h\nu$ and reducing it by the electron binding energy E_B for the particular constituent of air involved in the interaction. Then $q(\beta;\Theta,\Phi)$ can be normalized such that

$$\int_0^{\pi}\int_0^{2\pi} q(\beta;\Theta',\Phi')\sin\Theta'\,d\Theta'\,d\Phi' = 1, \tag{19}$$

so that $K_1 = \frac{3}{4\pi}$, $K_2 = \frac{3\left(a^2-\beta^2\right)^2}{4\pi}$, with $a = 1+(E/2m_e c^2)$ and

$$K_3 = \frac{3}{8\pi\beta^2}\sqrt{1-\beta^2}(1-\beta^2)^3 \Big/ \left\{\left[\left(1-\sqrt{1-\beta^2}\right)\left(1-2\sqrt{1-\beta^2}\right)\right]\left[2-\frac{1-\beta^2}{\beta}\ell n\left(\frac{1+\beta}{1-\beta}\right)\right]\right\}.$$

The primary electron and subsequent secondary electrons are assumed to dissipate energy continuously along the straight line in the direction Θ,Φ. The electron energy dissipation (deposition) along an element of air mass Δz (g/cm^2) from z to $z+\Delta z$ is given by

$$\Delta E = \int_z^{z+\Delta z} I(E_o, z)dz = r_o\left(\frac{dE}{dr}\right)_{E_o}\int_x^{x+\Delta x} J(E_o, x)dx \quad \text{[keV]}, \tag{20}$$

where

$E =$ electron kinetic energy [keV],

$E_o =$ initial electron kinetic energy [keV],

$z =$ $\int_0^s \rho(s)ds$ = column density of air measured from the source [g/cm^2],

$\rho =$ air density [g/cm^3],

$s =$ path length from source [cm],

$r_o =$ $r(E_o)$ = (residual) range in air for electrons with (initial) kinetic energy E_o [g/cm^2],

$r =$ $\int_0^E \frac{dE}{(dE/dr)}(0 < E < E_o)$ = residual range of electrons of energy E [g/cm^2],

$\left(\frac{dE}{dr}\right)_{E_o} =$ stopping power of air for electrons with energy E_o [keV/(g/cm^2)],

$x =$ z/r_o = dimensionless column density of air measured from the source ($-1 \le x \le +1$), or fractional range,

$I(E_o, z) =$ energy dissipation/unit column density of air for a source emitting electrons of energy E_o $[\mathrm{keV}/(\mathrm{g/cm^2})]$, and

$J(E_o, x) =$ normalized energy dissipation function for a source emitting electrons of energy E_o (a tabulation is required) $= \left(\frac{dE}{dr}\right)^{-1}_{E_o} I(E_o, z)$.

Note: $\int_{-1}^{+1} J(E_o, x)dx = (E_o/r_o)/(dE/dr)_{E_o}$; contributions to $J(x)$ at negative values of x are due to backscattering.

We define the cumulative energy dissipation function by

$$\varepsilon(E_o, x) = \frac{r_o}{E_o}\left(\frac{dE}{dr}\right)_{E_o} \int_{-1}^{x} J(E_o, x)dx. \tag{21}$$

Therefore the energy deposited along an increment of normalized air mass column density from x to $x + \Delta x$ is equal to

$$\Delta E = E_o\left[\varepsilon(E_o, x + \Delta x) - \varepsilon(E_o, x)\right]. \tag{22}$$

Spencer (1959) tabulated the quantity $J(E_o, x)$ for plane perpendicular and point isotropic sources for $0.025 \leq E_o \leq 10\,(\mathrm{MeV})$; he obtained his results by solving the requisite transfer equations by the method of expansion in spatial moments and spherical harmonics. Leopard *et al.* (1970) tabulated the quantity $\varepsilon(E_o, x)$ based on Spencer's results. For our use, we must extrapolate Spencer's tables to lower values of E_o.

The time required for electrons to travel the increment Δx is given by

$$\Delta t = \frac{r_o \Delta x}{\overline{\rho}\,\overline{v}}, \tag{23}$$

where $\overline{\rho}$ is the mean density of air,

$$\overline{v} = \frac{c\sqrt{\gamma(\gamma+2)}}{(\gamma+1)}, \tag{24}$$

$$\gamma = \frac{\overline{E}(x + \Delta x)}{m_e c^2}, \tag{25}$$

and $\overline{E}(x + \Delta x)$ is the mean kinetic energy of the electrons after penetrating $x + \Delta x$. Let $Q(x)$ represent the electron kinetic energy remaining after penetrating x so that

$$Q(x) - Q(x + dx) = E_o[\varepsilon(x + \Delta x) - \varepsilon(x)];$$

it then follows that

$$\overline{E}(x + \Delta x) = \frac{Q(x)}{\left(E_o\left[\varepsilon(x + \Delta x) - \varepsilon(x)\right]/\varepsilon_o\right)}, \tag{26}$$

where ε_o is the deposition energy required to produce one air ion and one electron ($\sim 0.034\,\text{keV}$). The optical emission from Δx during the time t to $t + \Delta t$ is given by $\eta \Delta E$, where η is the appropriate fluorescence efficiency and ΔE is properly scaled by the x-ray yield. It is sufficient to assume that the energy is deposited at a single point within each interval Δx.

IV. RESONANCE-FLUORESCENCE OF THE N_2^+ FIRST NEGATIVE BANDS

In this paper we are primarily concerned with the resonant-fluorescent scattering of the N_2^+ first negative bands within the region of x-ray dosed air. However, there are other transitions, especially the Meinel ($A^2\Pi_u - X^2\Sigma_g^+$), that indirectly affect the brightness of the first negative bands. Our present method, which can be likened to a "slot machine" model, uses a reasonably exact treatment for the radiative transfer of the first negative spectral lines combined with an approximate allowance for the Meinel in the initial conditions. We have made estimates indicating that insofar as effects on the first negative bands are concerned, it might be necessary to include explicitly radiative transfer in the Meinel light for the optically very thick cases, such as 1 Mt at 150 km. We are presently investigating the feasibility of doing this.

A. Spectrum of N_2^+ First Negative Bands

1. Spectroscopic Constants. The electronic potential energy curves of N_2 and N_2^+ are shown in Fig. 6. The spectroscopic data for the N_2^+ first negative system are summarized in Table VII. These are means of the values given by Huber and Herzberg (1979) and Lofthus and Krupenie (1977).

2. Einstein Coefficients of Spontaneous Emission. Table VIII gives values of the Einstein spontaneous emission coefficients $\mathbf{A}\,[B(V'=0), X(V''=0,1,2,3)]$ for the N_2^+ first negative bands.

These coefficients are defined such that the energy spontaneously emitted per unit volume per second into all directions is given by $n(V') \cdot h\nu(V',V'') \cdot \mathbf{A}(V',V'')$, where $n(V')$ is the number density of N_2^+ molecules in the upper V' state, $h\nu(V',V'')$ is the quantum energy associated with the V',V'' transition, and $\mathbf{A}(V',V'')$ is the spontaneous emission coefficient for the transition. This definition is the same as that used by Herzberg (1950).

B. Mechanisms of Resonance-Fluorescence

1. Excitation and Transfer of Resonant-Fluorescent Light. The interaction of the air molecules with the wave of x-ray photons and its concomitant electrons causes the initial creation and excitation of N_2^+ in the atmosphere. The column density of N_2^+ along a given line through the atmosphere depends primarily upon x-ray yield, x-ray spectrum, and altitude of the device. The third column of Table IX gives some calculated N_2^+ vertical column densities for a few burst yields and altitudes.

TABLE VII

SPECTROSCOPIC DATA FOR N_2^+ FIRST NEGATIVE SYSTEM

Electronic State	Electronic Term[a] (cm^{-1})	ω_e (cm^{-1})	$\omega_e x_e$ (cm^{-1})	$\omega_e y_e$ (cm^{-1})
B	150 631.4	2419.84	23.19	−0.269
X	125 117.8	2207.09	16.12	−0.040

	$D_V(cm^{-1})$				
V	0	1	2	3	4
B	2.073	2.049	2.025	2.002	1.968
X	1.922	1.904	1.884	1.865	1.846

	$10^6 B_V(cm^{-1})$				
V	0	1	2	3	4
B	-	-	-	-	-
X	5.92	6.60	5.93	6.1	6.8

[a] Measured from the ground state of N_2.

TABLE VIII

SPONTANEOUS EMISSION COEFFICIENTS A[B($V' = 0$) − X($V'' = 0, 1, 2, 3, 4$)] (s^{-1})

V''	0	1	2	3	4
A[a]	1.07 + 7	3.50 + 6	8.04 + 5	1.50 + 5	2.40 + 4
A[b]	1.04 + 7	3.76 + 6	8.38 + 5	1.47 + 5	2.23 + 4
A(mean)	1.06 + 7	3.63 + 6	8.21 + 5	1.48 + 5	2.32 + 4

[a] Shemansky and Broadfoot (1971).

[b] Jain and Sahni (1967).

TABLE IX

MAXIMUM N_2^+ VERTICAL COLUMN DENSITY[a] AND REPRESENTATIVE OPTICAL THICKNESS IN THE FIRST NEGATIVE BANDS

Burst Altitude (km)	X-Ray Yield (kt)	Vertical Column Density (N_2^+/cm^2)	Optical Thickness for $\lambda(V', V'')$ (0,0) (3914)	(0,1) (4278)	(0,2) (4709)	(0,3) (5228)
150	0.96	1.0 + 15	4.4	0.63	0.069	0.0089
	119.0	1.0 + 17	440.0	63.0	6.9	0.89
	870.0	6.0 + 17	2600.0	378.0	41.0	5.3
2000	0.96	1.4 + 12	0.0062	8.8−04	9.7−05	1.2−05
	119.0	1.7 + 14	0.75	0.11	0.012	0.0015
	2000.0	1.1 + 15	4.8	0.69	0.076	0.0098

[a] Along the vertical through the burst.

Holland estimates (see Sec. III.B.2) that the initial relative populations of the $X^2\Sigma$-state of N_2^+ are in the ratios $0.662(V''=0)$: $0.208(V''=1)$: $0.0767(V''=2)$: $0.0299(V''=3)$: $0.0118(V''=4)$. These populations assume that the N_2^+ ground state is populated by direct ionization from N_2 and by N_2^+ first negative and N_2^+ Meinel emission. Charge-transfer deactivation, especially at altitudes below ~70 km, readjusts these populations in time by depleting the vibrationally excited states $X(V''>0)$. Also, there is some collisional deactivation of the upper $B(V'=0)$ state. The effect of Meinel deactivation is more difficult to judge and is not presently included in our calculations. Meanwhile, primarily because of chemical reactions, the total N_2^+ ion population decreases with time in a manner that favors its persistence at altitudes above 80-90 km (Table X).

The N_2^+ ions in any one of the states $X(V'')$ can absorb the respective optical band $[B(V'=0), X(V'')]$ by resonance absorption. Re-emission can then take place in any one of the bands. This process of absorption followed by emission is called resonant-fluorescent scattering. The number of such scattering events that occurs depends upon the optical thickness of the x-ray dosed region in each of the four wavelength bands. Absorption cross sections for representative rotational lines are shown in Table XI; from these we can estimate the optical thickness corresponding to any given column density. The reader can refer to the last four columns of Table IX where we give results for two burst altitudes and three x-ray yields (Collins and Wells 1982). It is evident that high yield and low altitude favor an optical thickness large enough to produce multiple scattering. This in turn complicates the solution because the various radiative processes must be treated simultaneously in all four bands.

TABLE X

ABUNDANCES OF N_2^+ AND e^- IN THE VERTICAL THROUGH THE BURST AT VARIOUS ALTITUDES AS A FUNCTION OF TIME (Y_X = 150 kt at H_B = 145 km)

Altitude (km):	51		63		74	
Time (s)	$[N_2^+]$	$[e^-]$	$[N_2^+]$	$[e^-]$	$[N_2^+]$	$[e^-]$
0.00+00	2.17+11	3.50+11	3.55+11	5.73+11	4.91+11	7.93+11
5.00−06	5.70+10	2.57+11	1.72+11	3.69+11	2.43+11	4.67+11
1.00−05	1.61+10	2.01+11	9.66+10	2.67+11	1.50+11	3.29+11
5.00−05	1.50+06	7.70+10	3.69+09	8.32+10	2.00+10	1.02+11
1.00−04	2.46+01	3.91+10	1.41+08	4.33+10	4.27+09	5.99+10
5.00−04			1.78+02	8.23+09	1.36+06	1.14+10
1.00−03					3.95+02	4.59+09
Altitude (km):	81		86		93	
Time (s)	$[N_2^+]$	$[e^-]$	$[N_2^+]$	$[e^-]$	$[N_2^+]$	$[e^-]$
0.00+00	8.28+11	1.34+12	6.64+11	1.07+12	5.10+11	8.23+11
5.00−06	3.05+11	6.42+11	2.86+11	5.74+11	2.60+11	4.95+11
1.00−05	1.66+11	4.48+11	1.67+11	4.18+11	1.64+11	3.73+11
5.00−05	1.55+10	1.58+11	1.65+10	1.85+11	2.03+10	1.86+11
1.00−04	3.09+09	1.00+11	2.89+09	1.27+11	3.38+09	1.50+11
5.00−04	1.90+06	3.79+10	1.77+06	5.67+10	3.15+05	7.86+10
1.00−03	8.32+03	1.54+10	3.88+03	3.87+10	2.18+02	5.65+10
Altitude (km):	100		114			
Time (s)	$[N_2^+]$	$[e^-]$	$[N_2^+]$	$[e^-]$		
0.00+00	3.12+11	5.16+11	1.11+11	1.90+11		
5.00−06	1.98+11	3.69+11	9.40+10	1.70+11		
1.00−05	1.41+11	2.96+11	8.12+10	1.54+11		
5.00−05	2.65+10	1.55+11	3.41+10	9.63+10		
1.00−04	6.20+09	1.28+11	1.59+10	7.45+10		
5.00−04	6.31+05	9.74+10	2.02+08	5.55+10		
1.00−03	6.37+01	7.84+10	1.34+06	5.40+10		

Significantly, optical thickness of the medium varies so much between the different molecular bands that photons existing in one optically thick molecular band can switch by scattering to another band for which the medium is optically thinner and consequently become more capable of escaping from the medium. This process results in an enhancement of the radiation for which the medium is optically thin at the expense of that for which it is optically thick (Fig. 9). We define the enhancement as the time-integrated emission in a given band divided by the emission without resonant-fluorescent absorption or scattering.

TABLE XI

N_2^+ FIRST NEGATIVE BAND MEAN-ABSORPTION CROSS SECTIONS FOR T = 200 K

λ(Å)	cm^2/N_2^+
3914	4.4 - 15
4278	6.0 - 16
4709	6.6 - 17
5228	6.7 - 18

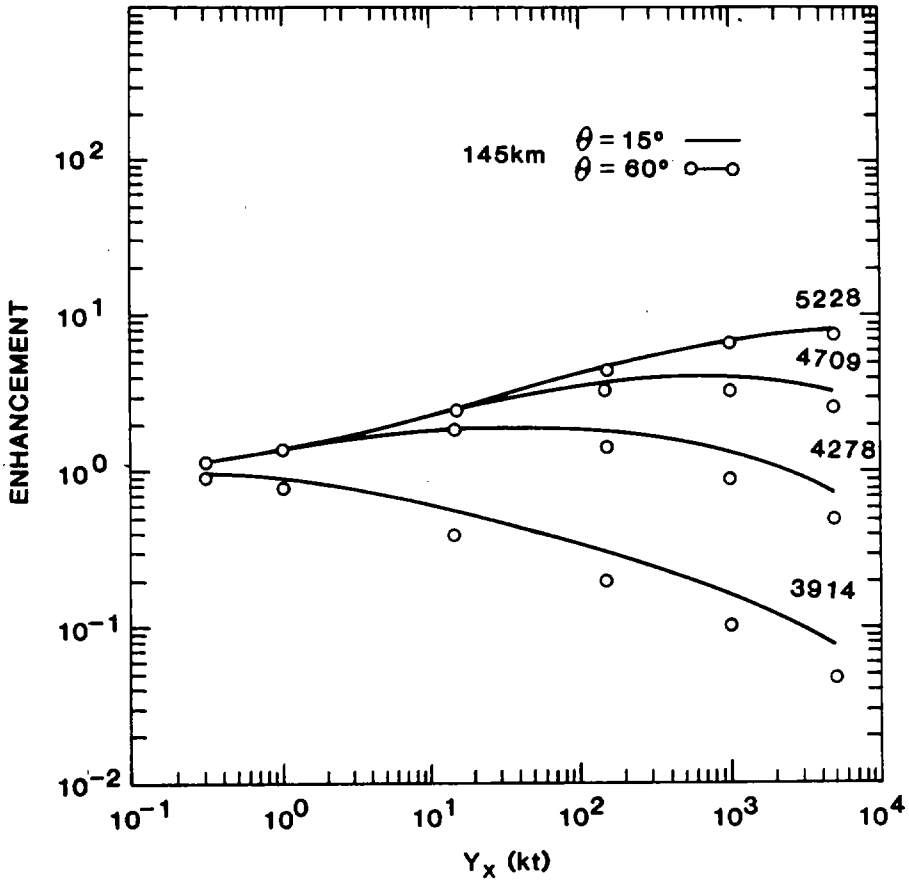

Fig. 9. Enhancement of first negative bands as a function of x-ray yield Y_x. Two satellite receiver zenith angles are considered: $\theta = 15°$ and $\theta = 60°$. The burst altitude is 145 km.

To model these processes, we chose to perform radiative transfer calculations for the individual rotational lines that constitute each band. Alternatively, it is much simpler to use mean-absorption

cross sections averaged over each band. However, this is not a rigorous procedure, and it is likely to give inaccurate results. The most accurate method is to transport the individual frequencies that make up each rotational line; this is necessary if detailed line profiles are to be calculated inside the medium or on emergence from the medium (not the purpose of this study). Many frequency points are required, but the transmission factor has the simple exponential form.

2. Equations of the Problem

a. Definitions and the Transmission Function for a Single Rotational Line. A molecular energy level is identified by the quantities X, V, J: X specifies the electronic state, V and J the vibrational and rotational levels, respectively. We assume that transitions $(X'V'J', X''V''J'')$ take place within an element of volume dV located at position $\vec{r}$. The flux [ergs/s] in the frequency interval ν to $\nu + d\nu$ spontaneously emitted by dV into the directions confined to the element of solid angle $d\Omega$ is $E_\nu^{(s)} d\nu dV d\Omega$, where $E_\nu^{(s)}$ is the spontaneous emission coefficient. This emission is assumed to be isotropic with respect to direction. Let $I_\nu(\vec{r}, \vec{\Omega})$ be the spectral intensity (radiance) of radiation of frequency ν incident on dV in the direction $\vec{\Omega}$. The flux absorbed by dV is given by $I_\nu(\vec{r}, \vec{\Omega}) K_\nu d\nu dV d\Omega$, where K_ν is the volume absorption coefficient. Similarly the flux of induced emission is $I_\nu(\vec{r}, \vec{\Omega}) E_\nu^{(i)} d\nu dV d\Omega$, where $E_\nu^{(i)}$ is the induced emission coefficient; such induced emission travels in the same direction $\vec{\Omega}$ as the incident light. These coefficients are related to the Einstein transition probabilities $\mathbf{A}(V'J' \to V''J'')$, $\mathbf{B}(V''J'' \to V'J')$ and $\mathbf{B}(V'J' \to V''J'')$ as follows:

$$4\pi E_\nu^{(s)} = n(V'J')\mathbf{A}(V'J' \to V''J'')h\nu\chi_\nu = 4\pi E^{(s)}\chi_\nu, \tag{27}$$

$$K_\nu = n(V''J'')\mathbf{B}(V''J'' \to V'J')h\nu\phi_\nu = K\phi_\nu, \tag{28}$$

$$4\pi E_\nu^{(i)} = n(V'J')\mathbf{B}(V'J' \to V''J'')h\nu\psi_\nu = 4\pi E^{(i)}\psi_\nu, \tag{29}$$

where $\chi_\nu, \phi_\nu, \psi_\nu$ are spectral line profile functions whose integrals over frequency are normalized to unity. Certain relations exist between the Einstein coefficients that remain valid under non-LTE conditions, namely

$$\frac{\mathbf{B}(V'J' \to V''J'')}{\mathbf{B}(V''J'' \to V'J')} = \frac{g(V''J'')}{g(V'J')}, \tag{30}$$

$$\frac{\mathbf{A}(V'J' \to V''J'')}{\mathbf{B}(V'J' \to V''J'')} = \frac{8\pi h\nu^3}{c^2}, \tag{31}$$

where g is the statistical weight, h is Planck's constant, and c is the speed of light. It is also convenient in radiative transfer theory to use some additional quantities:

$$j_\nu = E_\nu^{(s)} \text{ the volume emission coefficient [ergs/s} \cdot \text{cm}^3 \cdot \text{sr} \cdot \text{Hz}], \tag{32}$$

$$k_\nu = K_\nu - E_\nu^{(i)} \text{ the volume extinction coefficient [cm}^2/\text{cm}^3 \cdot \text{Hz}], \tag{33}$$

$$S_\nu = j_\nu / k_\nu \text{ the source function [ergs/s} \cdot \text{cm}^2 \cdot \text{sr} \cdot \text{Hz}], \tag{34}$$

and

$$\tau_\nu(s) = \int_o^s k_\nu(s')ds' \tag{35}$$

(s is path length along the light ray) the optical distance (not to be confused with τ used for lifetimes, as in Chap. III).

The time-independent monochromatic form of the equation of radiative transfer is written

$$\frac{dI_\nu(\vec{r},\vec{\Omega})}{ds} = -k_\nu I_\nu(\vec{r},\vec{\Omega}) + j_\nu(\vec{r}), \tag{36}$$

or

$$\frac{dI_\nu(\vec{r},\vec{\Omega})}{d\tau_\nu} = -I_\nu(\vec{r},\vec{\Omega}) + S_\nu(\vec{r}), \tag{37}$$

where $\vec{\Omega}$ is the direction of the light path at point $\vec{r}$. The formal solution of the equation of transfer for the case of no radiation incident on the boundary of the medium is

$$\begin{aligned} I_\nu(s,\vec{\Omega}) &= \int_0^s j_\nu(s')\exp\left[-\int_{s'}^s k_\nu(s'')ds''(\vec{\Omega})\right]ds'(\vec{\Omega}) \\ &= \int_0^{\tau_\nu(s)} S[\tau_\nu(s')]\exp[-\tau_\nu(s)+\tau_\nu(s')]d\tau_\nu(s'). \end{aligned} \tag{38}$$

We shall modify this equation into the necessary form to evaluate the transmission of a single spectrum line and alternatively of an entire vibration-rotational band. Integrating over the frequency in the line gives

$$\begin{aligned} I(s,\vec{\Omega}) &= \int_0^s ds' \int_0^\infty d\nu j_\nu(s')\exp\left[-\int_{s'}^s k_\nu(s'')ds''\right] \\ &= \int_0^s ds' E^{(s)}(s')T(s-s'), \end{aligned} \tag{39}$$

where

$$T(s-s') = \int_0^\infty d\nu\chi_\nu(s')\exp - \int_{s'}^s \left[K(s'')\phi_\nu(s'') - E^{(i)}(s'')\psi_\nu(s'')\right]ds'' \tag{40}$$

is the transmission function for the spectrum line. This expression considers only self-absorption, and the effects of overlap with other nearby lines have not been included. To proceed further, we shall assume that induced emission can be neglected compared with spontaneous emission and that $\phi_\nu = \chi_\nu = \psi_\nu$, which is the law of complete frequency redistribution. This law is obeyed only on the microscopic scale, the actual line profile showing deformation in shape within the medium. Therefore, we have the following simplified equation for the transmission of a single line

$$T(s-s') = \int_0^\infty d\nu\phi_\nu(s')\exp\left[-\int_{s'}^s K(s'')\phi_\nu(s'')ds''\right]. \tag{41}$$

At altitudes above ~30 km we shall assume that the Doppler line shape function is appropriate; namely, $\phi_\nu = e^{-x^2}/\sqrt{\pi}\Delta\nu_D$, where $x = (\nu-\nu_0)/\Delta\nu_D$, $\Delta\nu_D = V_0\nu_0/c$, $V_0 = \sqrt{2kT/M}$, ν_0 is the central frequency of the line, M the molecular weight of nitrogen, k the Boltzmann constant, T the absolute temperature, V_0 the most-probable speed of the nitrogen molecules, and $\Delta\nu_D$ the Doppler half-width of the spectral line.

Let us next consider a point source of emission strength $\Im(\vec{s} = 0, \vec{\Omega}; X'V'J', X''V''J'')$ [ergs/s· sr] within a homogeneous atmosphere. We shall ignore the time dependence for the present. It is readily handled by the Monte Carlo technique. However, we shall consider the possibility of wavelength overlap by line profiles near the emitted line, and it must be kept in mind that each overlapping line must also be considered an emitter in turn. Indeed, an alternative way of treating overlap is to consider the line profile in question (both in emission and absorption) to be composed of a properly normalized superposition of all the line profiles involved.

The following factorizations are used when convenient (Herzberg 1950; Gardiner 1982):

$$n(X,V,J) = n(X,V)f(X,V,J), \tag{42}$$

$$\mathbf{A}(X'V'J', X''V''J'') = \mathbf{A}(X'V', X''V'') \cdot \frac{S_J(J', J'')}{(2J'+1)}, \tag{43}$$

$$\mathbf{B}(X''V''J'', X'V'J') = \mathbf{A}(X'V', X''V'') \times \frac{c^2}{8\pi h\nu^3} \cdot \frac{S_J(J', J'')}{(2J''+1)}, \tag{44}$$

where

$$f(X,V,J) = \frac{(2J+1)}{Q(XV)} W(XVJ) exp[-F(XVJ)], \tag{45}$$

$$Q(XV) = \sum_{J=0}^{J_{MAX}} (2J+1) W(XVJ) exp[-F(XVJ)] \tag{46}$$

(partition function),

$W(XVJ)$ is the nuclear spin weighting function,

$$F(XVJ) = J(J+1)[B_V - D_V \cdot J(J+1)]\frac{hc}{k\mathbf{T}} \tag{47}$$

(B_V, D_V are rotational constants; $\mathbf{T}$ is the rotational temperature), and

$S_J(J', J'')$ is the line strength factor.

It follows that

$$\Im(\vec{s}=0; V'J', V''J'') = \Im(\vec{s}=0; V', V'') \left[f(\vec{s}=0; J') \cdot \frac{S_J(J', J'')}{(2J'+1)} \cdot \frac{h\nu(J', J'')}{h\nu(V', V'')} \right]. \tag{48}$$

This emission is produced by complex processes that are impractical to model in detail, and it is simplest to make use of the fluorescence efficiency. We have

$$4\pi\Im(\vec{s}=0; V', V'') = \eta(\vec{s}=0; V', V'')E_X, \tag{49}$$

where η is the band fluorescence efficiency and E_X the x-ray energy deposition rate. The factor in the brackets of Eq. (48) when multiplied by η gives in effect the rotation-line fluorescence efficiency.

The irradiance at $\vec{s} = s\vec{\Omega}$ is given by

$$H(\vec{s} = s\vec{\Omega}; V'J', V''J'') = \frac{\Im(0; V', V'')}{s^2}\left[f(0, J') \cdot \frac{S_J(J', J'')}{(2J'+1)} \cdot \frac{h\nu(J', J'')}{h\nu(V', V'')}\right]$$

$$\times\left\{\int_0^\infty d\nu\phi_\nu(s=0; J', J'')exp - \left[\frac{c^2\mathbf{A}(V', V'')}{8\pi}\sum_{J_L, J_U}\frac{1}{\nu^2(J_L, J_U)} \cdot \frac{S_J(J_L, J_U)}{(2J_L+1)}\right.\right.$$

$$\left.\left. \times \int_0^s ds' n(s'; V'')f(s'; J_L)\phi_\nu(s'; J_L, J_U)\right]\right\} \text{ [ergs/cm}^2 \cdot \text{s]}. \tag{50}$$

The summation is taken over all transitions J_L, J_U (J_L refers to the lower state, J_U to the upper state) that contribute appreciable absorption to the emission line J', J''. The line center frequencies are indicated by $\nu(J', J'')$ or $\nu(J_L, J_U)$, etc., while $\nu(V', V'')$ refers to the band "center." This equation is derived by Gardiner [1982; Eq. (15)]; in his program TRNSM, overlapping is assumed to occur when the centers of the two lines are less than 5.6 $\Delta\nu_D$ apart. If the atmosphere is homogeneous, the line form Doppler, and only self-overlap is considered, the above equation assumes the form

$$H(s; J', J'') = \frac{\Im(0; V', V'')}{s^2}\left[f(0, J') \cdot \frac{S_J(J', J'')}{(2J'+1)} \cdot \frac{h\nu(J', J'')}{h\nu(V', V'')}\right]$$

$$\times \frac{1}{\sqrt{\pi}}\int_{-\infty}^{+\infty} dx\ \exp\left[-x^2 - \tau(J', J'')e^{-x^2}\right], \tag{51}$$

where $\tau(J', J'')$ is the optical distance at the line center defined by

$$\tau(J', J'') = \frac{c^2\mathbf{A}(V', V'')}{8\pi\sqrt{\pi}}\left[\frac{1}{\nu^2(J', J'')}) \cdot \frac{S_J(J', J'')}{(2J''+1)} \cdot \frac{f(J'')}{\Delta\nu_D(J', J'')}\right] n_+(V'') \tag{52}$$

with

$$n_+(V'') = \int_0^s n(s'; V'')ds'.$$

The integral over x is sometimes called the Holstein transmission function, $T_H(\tau)$ (refer to Holstein 1947). Various methods can be used to compute this integral for the values of τ required; for example, see Ivanov and Shcherbakov (1965). In Fig. 10 we compare graphs of T_H and $e^{-\tau}$: the exponential falls more rapidly with τ than does the Holstein function.

To carry out radiative transfer calculations, we use the effective absorption coefficient for a spectral line defined by $[-d\ell nT/ds]$ evaluated at s in direction $\vec{\Omega}$. To justify this, consider the following: the effective absorption coefficient $\beta(s)$ is related to intensity $I(s, \vec{\Omega})$ by

$$I(s, \vec{\Omega})\beta(s, \vec{\Omega})\delta s = I(s, \vec{\Omega}) - I(s+\delta s, \vec{\Omega}) = I(0)[T(0; s) - T(0; s+\delta s)],$$

(integrated over the spectral line) where $T(0; s)$ is the transmission from $s = 0$ to s, and δs is an increment of path length. Solving for $\beta(s)$, we have

$$\beta(s) = \frac{T(0; s) - T(0; s+\delta s)}{\left[\frac{I(s)}{I(0)}\right]\delta s} = \frac{T(0; s) - \left[T(0; s) + \frac{dT(0; s)}{ds}\delta s\right]}{T(0; s)\delta s},$$

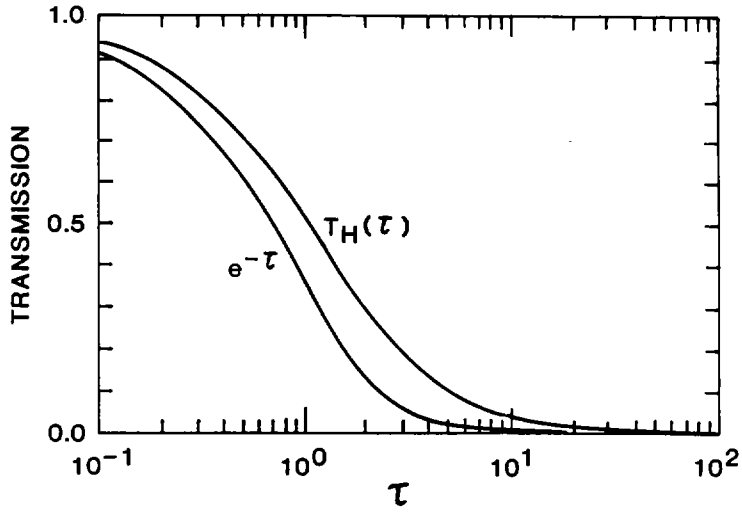

Fig. 10. Comparison of exponential transmission with that given by the Holstein function, T_H.

or

$$\beta(s,\vec{\Omega}) = -\left[\frac{d\ell nT(0;s)}{ds}\right]_{s,\vec{\Omega}}.$$

Consider a volume element dV at location $s\vec{\Omega}$. The intensity [ergs/cm^2·sr] scattered into any assigned direction $\vec{\Omega}^*$ is expressed by

$$\Im(s,\vec{\Omega}^*,J',J'') = H(s;J',J'')dV\left[-\frac{d\ell nT}{ds}\right]_{s,\vec{\Omega}}\cdot b\cdot\frac{1}{4\pi},$$

where the effective scattering coefficient is

$$\beta_{sc}(J',J'') = b\cdot\left[-\frac{d\ell nT}{ds}\right]_{s,\vec{\Omega}},$$

and the branching ratio is $b = \mathrm{A}(J',J'')/\sum_{J''}\mathrm{A}(J',J'')$, the sum being taken over all possible transitions originating from the upper level J'.

b. Details for N_2^+ First Negative Bands. A schematic diagram of rotational levels for the N_2^+ first negative bands is shown in Fig. 11 (Gardiner 1982, p. 17; Herzberg 1950, pp. 247–250). The rotational energy levels are spin doublets, each level of which possesses a J-value (J' or J''), the total angular momentum quantum number. The quantum number N (N' or N$''$) for angular momentum exclusive of spin identifies each doublet and is the mean of the J-values of the two levels involved. Transitions can only occur between J' and $J'' = J'$ (a Q-branch line), between J' and $J'' = J' + 1$ (a P-branch line), and between J' and $J'' = J' - 1$ (an R-branch line). Close to each P- or R-branch doublet is a Q-branch line belonging to a P-like Q-branch ($^PQ_{12}$) or an R-like Q-branch line ($^RQ_{21}$), respectively.

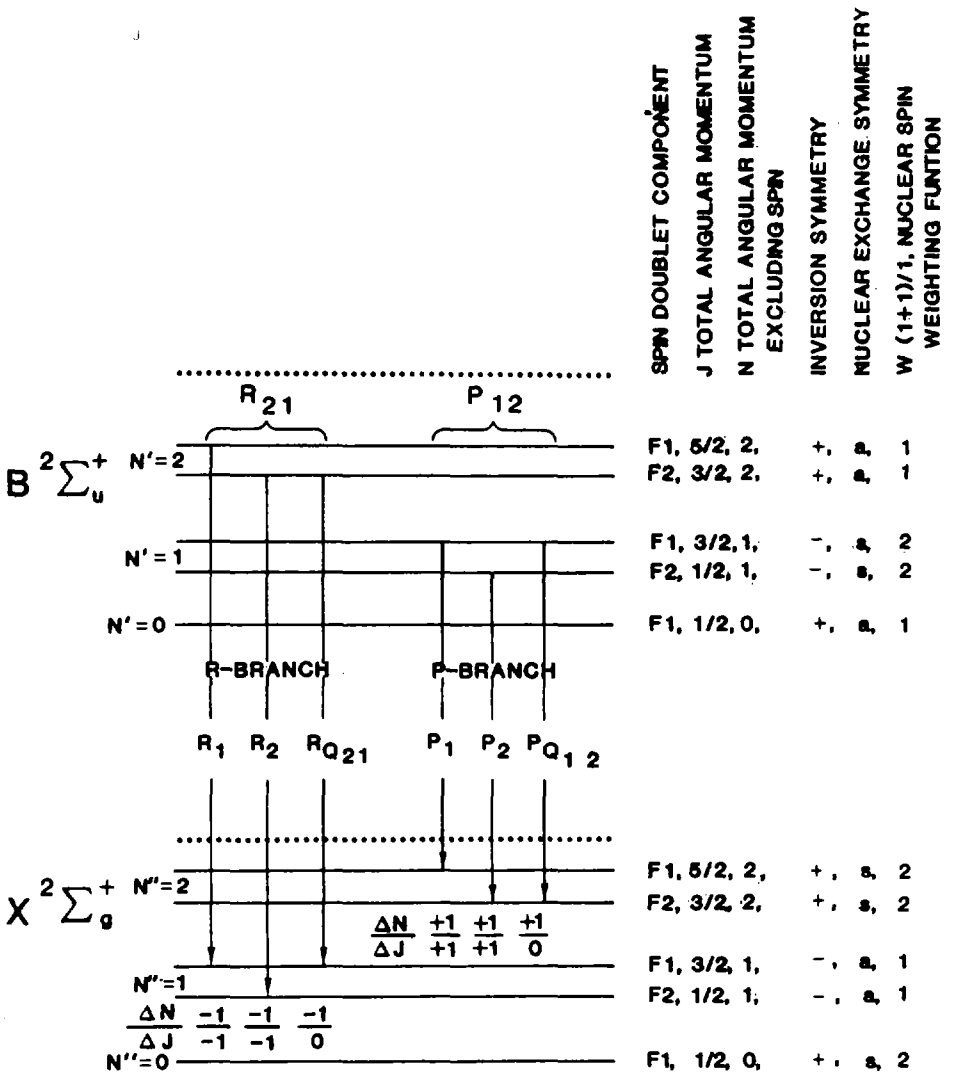

Fig. 11. Schematic of rotational levels (spin doublet spacing greatly exaggerated) for the N_2^+ first negative bands.

The measurements by Childs (1932) show that the doublet splitting amounts to 0.013 N' [cm^{-1}] for $V' = 0$ and 0.002N''[cm^{-1}] for $V'' = 0, 1$. Now most of the radiative transfer in the 70-90-km region takes place with an ambient temperature $\sim$ 200 K. This means that the rotational energy states have their maximum population at $N' \sim 5, 6$. The wavelength difference between an R_1 and R_2 line at $N' = 5$ amounts to 0.009 Å, which is about two Doppler half-widths at λ 3914 Å and 200 K. At $N' = 10$ the wavelength difference amounts to 0.017 Å, which is also about two half-widths for a temperature of 700 K. The R-like Q-component is slightly farther away of course, but weak. Similar arguments apply to the P-branch.

A rigorous calculation of transmission requires that the rotational lines for $J' \rightarrow J''(J'' = J', J' \pm 1)$ be treated individually rather than clumped together into the single line $N' \rightarrow N''(N'' = N' \pm 1)$ with the upper and lower doublet levels each replaced by a single "equivalent" level. Nevertheless, the value of the transmission integral is not seriously compromised by this procedure. We have (Gardiner 1982):

$$\begin{aligned} S_J^P(N', N'') &= S_J(P_1) + S_J(P_2) + S_J({}^PQ_{12}) \\ &= \frac{4J''^2 - 1}{4J''} + \frac{4(J'' - 1)^2 - 1}{4(J'' - 1)} + \frac{2(J'' - 1) + 1}{4(J'' - 1)J''} \\ &= 2N'', \end{aligned} \tag{53}$$

and

$$\begin{aligned} S_J^R(N', N'') &= S_J(R_1) + S_J(R_2) + S_J({}^RQ_{21}) \\ &= \frac{(J'' + 1)^2 - \frac{1}{4}}{J'' + 1} + \frac{J''^2 - \frac{1}{4}}{J''} + \frac{2J'' + 1}{4J''(J'' + 1)} \\ &= 2(N'' + 1). \end{aligned} \tag{54}$$

Because we are interested in two single lines, each of which represents the sum of three rotational lines, the effective transmission for the triads can be written

$$T(P) = T(P_1) + T(P_2) + T({}^PQ_{12}), \quad (N', N''), \tag{55}$$

and

$$T(R) = T(R_1) + T(R_2) + T({}^RQ_{21}), \quad (N', N''), \tag{56}$$

where in the homogeneous case we have

$$T(P; N', N'') = \int_0^\infty d\nu \phi_\nu(N', N'') \times exp\left[- \sum_{N_L, N_U} \sigma_\nu^P(N_L, N_U) \int_0^{s'} ds'' n(s''; X''V'') \right], \tag{57}$$

$$T(R; N', N'') = \int_0^\infty d\nu \phi_\nu(N', N'') \times exp\left[- \sum_{N_L, N_U} \sigma_\nu^R(N_L, N_U) \int_0^{s'} ds'' n(s''; X''V'') \right], \tag{58}$$

$$\sigma_\nu^P(N_L, N_U) = \frac{c^2}{8\pi} \frac{\mathbf{A}(X'V', X''V'')}{\nu^2(N_L, N_U)} \cdot \phi_\nu(N_L, N_U) \times \frac{2N_L \cdot W(N_L)}{Q(X''V'')} \cdot exp[-F(N_L)], \tag{59}$$

$$\sigma_\nu^R(N_L, N_U) = \frac{c^2}{8\pi} \frac{\mathbf{A}(X'V', X''V'')}{\nu^2(N_L, N_U)} \cdot \phi_\nu(N_L, N_U) \times \frac{2N_L + 1) \cdot W(N_L)}{Q(X''V'')} \cdot \exp[-F(N_L)], \tag{60}$$

ϕ_ν is the normalized Doppler line-form, and the partition function is given by

$$Q(X''V'') = \sum_{N_L} 2(2N_L + 1) \cdot W(N_L) \cdot \exp[-F(N_L)]. \tag{61}$$

The transitions (N_L, N_U) are those that overlap the emission features $(V'N', V''N'')$.

The initial emission factor is

$$\left[f(0,J')\frac{S_J(J',J'')}{2J'+1}\cdot\frac{h\nu(J',J'')}{h\nu(V',V'')}\right], \tag{62}$$

which assumes the following forms:

$$\frac{h\nu(N',N'')}{h\nu(V',V'')}\cdot\frac{(2N')\cdot W(N')}{Q(X'V')}\exp[-F(N')] \quad (R\text{-branch line triad}), \tag{63}$$

$$\frac{h\nu(N',N'')}{h\nu(V',V'')}\cdot\frac{(2N'+1)\cdot W(N')}{Q(X'V')}\exp[-F(N')] \quad (P\text{-branch line triad}), \tag{64}$$

where

$$Q(X'V') = \sum_{N'} 2(2N'+1)\cdot W(N')\exp[-F(N')], \text{ and} \tag{65}$$

$$F(N') \sim N'(N'+1)B_{V'}\, c_2/\mathbf{T}. \tag{66}$$

$B_{V'}$ is a rotational constant ($\sim 2\ \mathrm{cm}^{-1}$ for $N_2^+ - 1N$), $c_2 = 1.439(\mathrm{cm}\cdot K)$, $\mathbf{T}$ is the absolute temperature (K), and $W(N_L)$ and $W(N')$ are the nuclear spin functions for the states involved, namely

$$W(N') = 1 + \mathrm{MOD}((I+N'),2), \tag{67}$$

where $I = 2$ for the B-state and $I = 1$ for the X-state.

Gardiner (1982) gives a computer FORTRAN program in the Appendix section of his report to calculate the transmissions for the N_2^+ first negative vibration-rotational bands. In our Monte Carlo rotational calculations, we are concerned more with the transmission of lines $(V'N', V''N'')$; this requires minor modifications of his program.

C. Monte Carlo Methods to Calculate Time-Dependent Fluorescence

The multiple scattering aspects of the fluorescence problem are too complicated to be solved by analytical methods. Therefore, we apply the Monte Carlo method, which is well suited to this kind of situation and is especially effective in handling the time dependence. The various integrals are written down giving the contributions at a detector that are due to (i) direct-transmitted light, (ii) single-scattered fluorescence, (iii) double-scattered fluorescence, etc. The forms of the integrals are the same as if the problem were time independent. The time-dependent aspects can then be examined separately, which greatly simplifies the problem. These scattering calculations are carried out for an environment where rapid changes are taking place that must be followed by the computer program. Furthermore, at every scattering event it is necessary to apply the probability $(1 + K\mathbf{p})^{-1}$ [Eq. (2)] that the excited N_2^+ radiates before being deactivated by collisions.

In the next five sections we present the basic equations, the sampling techniques, and the time aspects. The first section is devoted to "forward" Monte Carlo, wherein representative photons are

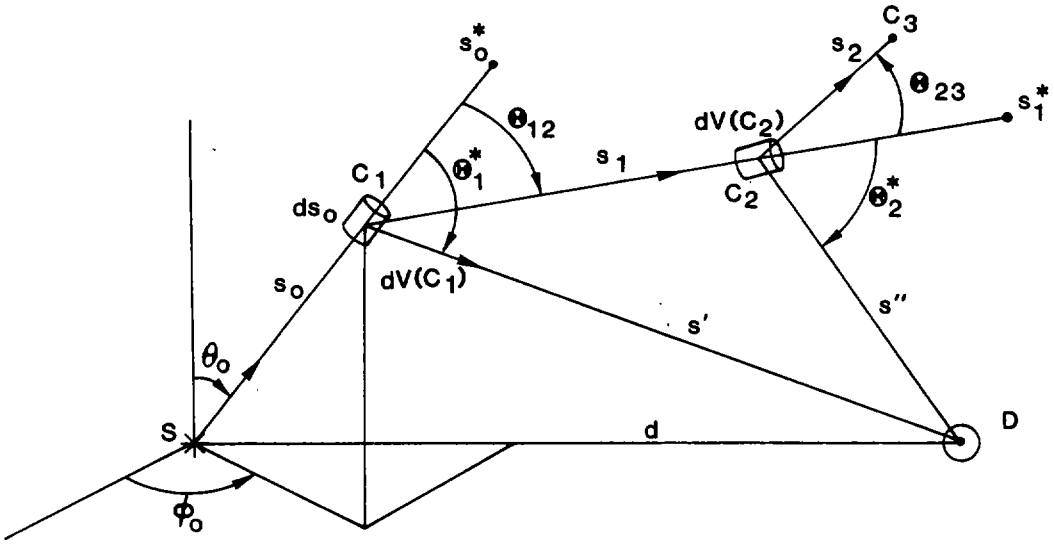

Fig. 12. The geometry of forward Monte Carlo.

traced from selected source points in the fluorescing air via scattering events until the photons escape from the medium; the second section considers the "backward" Monte Carlo procedure, wherein photons are traced from the detector in directions confined to the solid angle corresponding to the FOV, then "backwards" via collisions to source emission points. Each of the two procedures has its own domain of optimal applicability. The third and fourth sections discuss the time aspects. The fifth section considers the method of selecting a rotational spectrum line at either an emission or a collision point.

1. Forward Monte Carlo. The forward Monte Carlo method is well suited for calculating the irradiance in various fluorescent bands at a satellite detector; this is because the FOV of the detector is wide enough for a large number of the scattering events in the fluorescing volume to be detected, and consequently many statistical estimates can be made. However, if the FOV is small, it is more advantageous to use the backward Monte Carlo method.

Consider an isotropically radiating point source of fluorescence at S and an omnidirectional receiver of unit cross section at D (Fig. 12). The source emissive power for a rotational line ℓ' (ℓ' is selected as explained in Sec. IV.C.5.) is $E_{\ell'}$, [power into 4π sr], and the single-scattered flux in a line ℓ incident on D is given by

$$F_\ell^{(1)} = \sum_{\ell'} \frac{E_{\ell'}}{4\pi} \int_{s_o=0}^{s_o^*} \int_{\phi_o=0}^{2\pi} \int_{\theta_o=0}^{\pi} \frac{T_{\ell'}(s_o)}{s_o^2} \cdot \frac{\beta_{\ell'}(s_o, C_1)}{4\pi} \cdot p(C_1, \ell' \to \ell) \cdot \frac{T_\ell(s')}{s'^2} \cdot dV(C_1), \qquad (68)$$

where $T_{\ell'}(s_o)$ is the transmission for line ℓ' evaluated from 0 to s_o, i.e., S to C_1 in the figure, and $T_\ell(s')$ that for line ℓ from 0 to s' (C_1 to D), $\beta_{\ell'}(s_o, C_1) = -[d\ell n T_{\ell'}/ds]_{C_1}$, $p(C_1, \ell' \to \ell)$ is the probability at the scattering point C_1 of creating line ℓ, and $dV(C_1)$ is the volume element $s_o^2 \sin\theta_o d\theta_o d\phi_o ds_o$. The summation is taken over those eight lines with the same upper level N', which on scattering have finite probabilities of creating the line ℓ. The Monte Carlo method evaluates this integral by sampling

(i) ℓ',

(ii) θ_o from $\sin\theta_o d\theta_o/2$,

(iii) ϕ_o from $d\phi_o/2\pi$,

(iv) s_o from $\beta_{\ell'}(s_o, C1)T_{\ell'}(s_o)ds_o = \left[\frac{dT_{\ell'}}{ds}\right]_{C_1} ds_o$.

The estimating function then consists of

(v) $\hat{F}_\ell^{(1)} = p(C_1, \ell' \to \ell) \cdot \frac{T_\ell(s')}{4\pi s'^2} \cdot \sum_{\ell'} E_{\ell'}$. (69)

The double-scattered flux of line ℓ received at D is given by (refer again to Fig. 12)

$$F_\ell^{(2)} = \sum_{\ell''} \frac{E_{\ell''}}{4\pi} \int_{s_o=0}^{s_o^*} \int_{\phi_o=0}^{2\pi} \int_{\theta_o=0}^{\pi} \int_{s_1=0}^{s_1^*} \int_{\phi_1=0}^{2\pi} \int_{\theta_1=0}^{\pi} \frac{T_{\ell''}(s_o)}{s_o^2} \cdot \frac{\beta_{\ell''}(s_o, C_1)}{4\pi} \cdot \sum_{\ell'} p(C_1, \ell'' \to \ell') \cdot \frac{T_{\ell'}(s_1)}{s_1^2} \cdot \frac{\beta_{\ell'}(s_1, C_2)}{4\pi} \cdot p(C_2, \ell' \to \ell) \frac{T_\ell(s'')}{s''^2} dV(C_1) dV(C_2), \quad (70)$$

where $dV(C_2) = s_1^2 \sin\theta_1 d\theta_1 d\phi_1 ds_1$. This integral can be evaluated by sampling

(i) ℓ'',

(ii) θ_o from $\sin\theta_o d\theta_o/2$,

(iii) ϕ_o from $d\phi_o/2\pi$,

(iv) s_o from $\beta_{\ell''}(s_o, C1)T_{\ell''}(s_o)ds_o = \left[\frac{dT_{\ell''}}{ds}\right]_{C_1} ds_o$,

(v) ℓ',

(vi) θ_1 from $\sin\theta_1 d\theta_1/2$,

(vii) ϕ_1 from $d\phi_1/2\pi$,

(viii) s_1 from $\beta_{\ell'}(s_1, C_2)T_{\ell'}(s_1)ds_1 = \left[\frac{dT_{\ell'}}{ds}\right]_{C_2} ds_1$.

The estimating function then consists of

(ix) $$\hat{F}_\ell^{(2)} = p(C_2, \ell' \to \ell) \cdot \frac{T_\ell(s'')}{4\pi s''^2} \cdot \sum_{\ell''} E_{\ell''}. \quad (71)$$

This estimating function has the same form for all orders of scattering. Finally, the direct flux from the source is given by

$$F_\ell^{(o)} = \frac{E_\ell}{4\pi} \cdot \frac{T_\ell(d)}{d^2}, \quad (72)$$

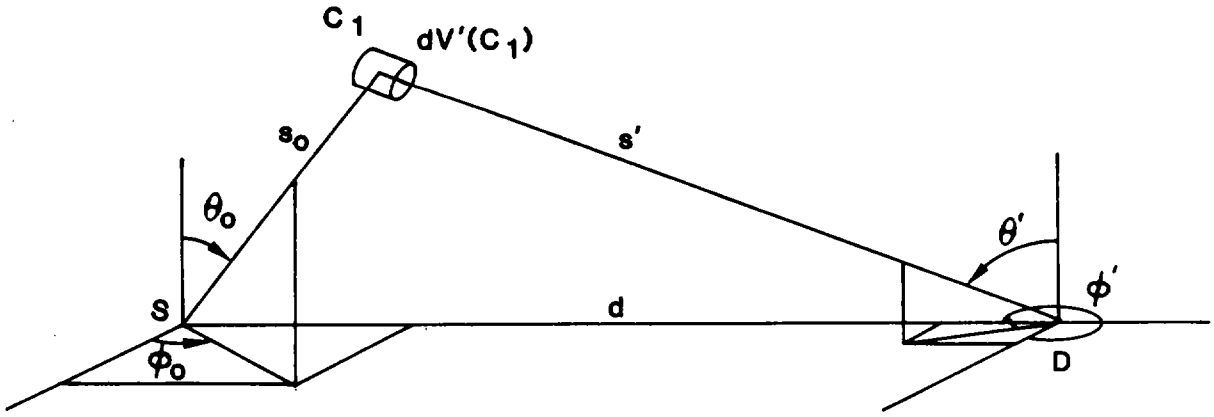

Fig. 13. The geometry of backward Monte Carlo—single scattering.

where d is the distance from source to detector.

2. Backward Monte Carlo. Again, as in the forward method, we first consider the time-independent case. For single scattering, refer to Fig. 13. The flux per unit area at the omnidirectional detector is given by

$$F_\ell^{(1)} = \sum_{\ell'} \frac{E_{\ell'}}{4\pi} \int_{s'=0}^{s'_\infty} \int_{\phi'_o=0}^{2\pi} \int_{\theta'_o=0}^{\pi} \frac{T_{\ell'}(s_o)}{s_o^2} \cdot \frac{\beta_{\ell'}(s_o, C_1)}{4\pi} \cdot p(C_1, \ell' \to \ell) \cdot \frac{T_\ell(s')}{s'^2} \cdot dV'(C_1), \qquad (73)$$

where the integration variables are defined at the detector instead of the source, and $dV'(C_1) = s'^2 \sin\theta' d\theta' d\phi' ds'$. The Monte Carlo procedure evaluates this integral by adopting ℓ and sampling

(i) θ' from $\sin\theta' d\theta'/2$,

(ii) ϕ' from $d\phi'/2\pi$,

(iii) s' from $\beta_\ell(s', C_1) T_\ell(s') ds' = \left[\frac{dT_\ell(s')}{ds'}\right]_{C_1} ds'$.

The estimating function consists of

(iv) $\hat{F}_\ell^{(1)} = \sum_{\ell'} \left\{ \frac{E_{\ell'}}{4\pi} \cdot \frac{T_{\ell'}(s_o)}{s_o^2} \cdot \frac{\beta_{\ell'}(s_o, C_1)}{\beta_\ell(s', C_1)} \cdot p(C_1, \ell \to \ell') \right\}$. (74)

The double-scattered flux per unit area of spectrum line ℓ received at D is given by (refer to Fig. 14)

$$F_\ell^{(2)} = \sum_{\ell''} \frac{E_{\ell''}}{4\pi} \int_{s_1=0}^{s_1^*} \int_{\theta'_1=0}^{\pi} \int_{\phi'_1=0}^{2\pi} \int_{s''=0}^{s''_\infty} \int_{\theta''=0}^{\pi} \int_{\phi''=0}^{2\pi} \frac{T_{\ell''}(s_o)}{s_o^2} \cdot \frac{\beta_{\ell''}(s_o, C_1)}{4\pi} \cdot$$
$$\sum_{\ell'} p(C_1, \ell'' \to \ell') \cdot \frac{T_{\ell'}(s_1)}{s_1^2} \cdot \frac{\beta_{\ell'}(s_1, C_2)}{4\pi} \cdot p(C_2, \ell' \to \ell) \cdot \frac{T_\ell(s'')}{s''^2} dV'(C_1) dV'(C_2), \qquad (75)$$

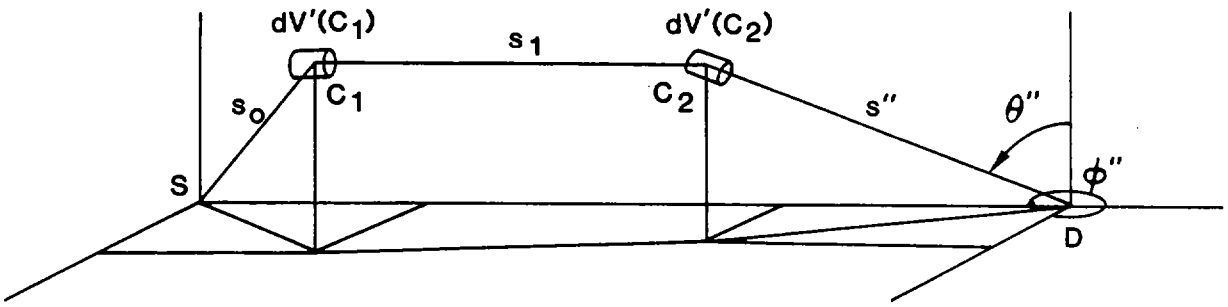

Fig. 14. The geometry of backward Monte Carlo—double scattering.

where $dV'(C_2) = s''^2 \sin\theta'' d\theta'' d\phi'' ds''$, and $dV'(C_1) = s_1^2 \sin\theta' d\theta' d\phi' ds_1$. The Monte Carlo procedure evaluates this integral by adopting ℓ and sampling

(i) θ'' from $\sin\theta'' d\theta''/2$,

(ii) ϕ'' from $d\phi''/2\pi$,

(iii) s'' from $T_\ell(s'')\beta_\ell(s'', C_2)ds'' = [dT_\ell/ds]_{C_2} ds''$,

(iv) ℓ' from $p(C_2, \ell' \to \ell)$,

(v) θ' from $\sin\theta' d\theta'/2$,

(vi) ϕ' from $d\phi'/2\pi$,

(vii) s_1 from $T_{\ell'}(s_1)\beta_{\ell'}(s_1, C_1)ds_1 = [dT_{\ell'}/ds]_{C_1} ds_1$.

The estimating function is given by

$$\text{(viii)} \quad \hat{F}_\ell^{(2)} = \sum_{\ell''} \left\{ \frac{E_{\ell''}}{4\pi} \frac{T_{\ell''}(s_o)}{s_o^2} \frac{\beta_{\ell''}(s_o, C_1)}{\beta_{\ell'}(s_1, C_1)} \cdot \frac{\beta_{\ell'}(s_1, C_2)}{\beta_\ell(s'', C_2)} p(C_1, \ell'' \to \ell') \right\}, \tag{76}$$

where

$$\beta_{\ell''}(s_o, C_1) = \frac{1}{T_{\ell''}(s_o)} \left[\frac{dT_{\ell''}}{ds}\right]_{C_1}, \beta_{\ell'}(s_1, C_1) = \frac{1}{T_{\ell'}(s_1)} \left[\frac{dT_{\ell'}}{ds}\right]_{C_1}$$

and

$$\beta_\ell(s'', C_2) = \frac{1}{T_\ell(s'')} \left[\frac{dT_\ell}{ds}\right]_{C_2}, \beta_{\ell'}(s_1, C_2) = \frac{1}{T_{\ell'}(s_1)} \left[\frac{dT'_\ell}{ds}\right]_{C_2}.$$

3. Time Dependence in Forward Monte Carlo. It is assumed that all x-ray photons are created instantaneously at (absolute) time $t = 0$. Let $t_1 = d_1/c$ be the time of arrival of an x-ray photon at the point P_1 (Fig. 15); this instant also corresponds to the creation of fluorescent light

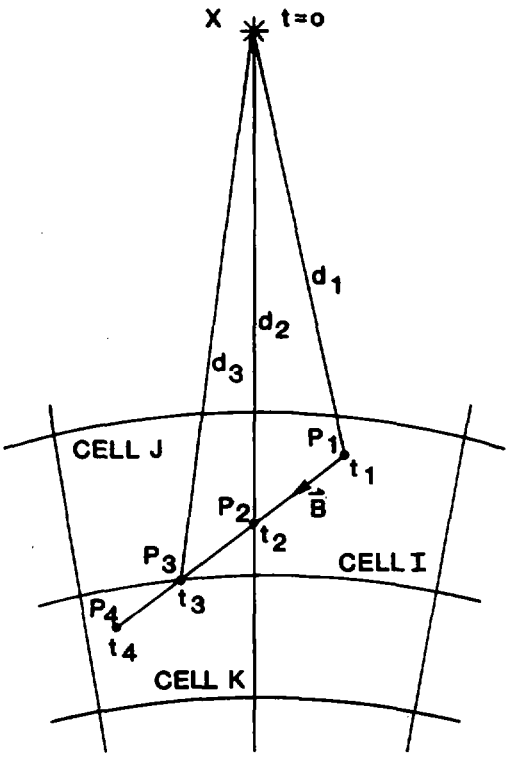

Fig. 15. Evaluation of transmission—absolute vs retarded time.

at P_1 (this assumption is discussed in Sec. III.B.4). Such light is emitted isotropically, the amount being the product of the x-ray energy deposition multiplied by the fluorescence efficiency. The optical fluorescence region is conveniently divided into volume cells with boundaries that are either spherical or conical surfaces with centers coinciding with the earth's center. Atmospheric properties, such as temperature and N_2^+ abundance, are assumed constant within each cell at any given time, though their values are permitted to change in magnitude with time. The dimensions of the cells are assigned primarily on the basis of energy deposition, consistent with the requirement that cell boundaries must be continuous.

Let the N_2^+ concentration be created by the x-ray energy deposition of amounts ϵ_j at various points within cell J, and for simplicity's sake in this discussion we shall assume local creation of optical fluorescent radiation. In cell J the amount of x-ray energy deposited per unit volume is $E_J = \sum_{j=1}^{N_J} \epsilon_j / V_J$, where N_J is the number of x-ray photons depositing energy in cell J and V_J is the cell volume. If we divide E_J(eV) by 54.4 eV, the energy required to create an N_2^+ ion-electron pair, we obtain the *initial* number of N_2^+ ions/unit volume created in cell J.* We assume that this concentration is uniform throughout the cell, and furthermore that it decays with time in accordance with the chemical reactions taking place there (Sec. III.B.3), somewhat like $n(N_2^+;t_R) = \alpha/[\beta \exp(\gamma t_R) - 1]$, where α, β, γ

* We usually use a more elaborate procedure (refer to Sec. III.A).

TABLE XII
ABSOLUTE VS RETARDED TIME

Point on Photon Path	Absolute Arrival Time of Fluorescent Photon	Retarded Arrival Time of Fluorescent Photon
P_1	t_1	$t_{R1} = t_1 - \frac{d_1}{c} = 0$
P_2	t_2	$t_{R2} = t_2 - \frac{d_2}{c} = (t_1 + \frac{P_1P_2}{c}) - \frac{d_2}{c}$
P_3	t_3	$t_{R3} = t_3 - \frac{d_3}{c} = (t_1 + \frac{P_1P_2+P_2P_3}{c}) - \frac{d_3}{c}$
P_4	t_4	$t_{R3} = t_4 - \frac{d_4}{c} = (t_1 + \frac{P_1P_2+P_2P_3+P_3P_4}{c}) - \frac{d_4}{c}$

are reaction constants for each mesh cell, and t_R is the *retarded* time, that is, for a given absolute time, t, measured at some point P: $t_R = t - \frac{d}{c}$.

Consider a fluorescent photon emitted at P_1 in the direction $\vec{B}$ (refer again to Fig. 15); this direction may be chosen by Monte Carlo sampling or alternatively might be the direction toward one of several receivers. Our problem is to evaluate the transmission $T_\ell(P_1P_4)$ of a spectrum line ℓ from point P_1 to a final point P_4 with P_2, P_3 being the intermediate cell boundary intersections. We can readily construct Table XII, which gives the relations between absolute and retarded times at these points.

The column density $n_+(P_1P_4)$ of N_2^+ between P_1 and P_4, allowing approximately for the time of transit of the photons, is given by

$$\begin{aligned} n_+(P_1P_4) = {} & (P_1P_2)n_I(N_2^+; \bar{t}_{R12}) \\ & + (P_2P_3)n_J(N_2^+; \bar{t}_{R23}) \\ & + (P_3P_4)n_K(N_2^+; \bar{t}_{R34}), \end{aligned} \tag{77}$$

where $\bar{t}_{Ri\ i+1} = (t_{Ri} + t_{Ri+1})/2$ (i = 1,2,3), n_I is the concentration of N_2^+ in cell I at retarded time $\bar{t}_{R12}$, n_J in cell J at time $\bar{t}_{R23}$, and n_K in cell K at time $\bar{t}_{R34}$. It is necessary to tabulate n_I vs t_R for every mesh cell I. For a given column density, and assuming a mean temperature along the path, it is possible then to compute the transmission of spectrum line ℓ (Sec. IV.B.2). This procedure is not quite rigorous, but it represents a reasonable practical compromise.

The inverse problem to that just discussed concerns calculating the distance s corresponding to a given value of the transmission function $T_\ell(s)$. Let s_i be the distance from the initial point P_1 in a given direction $\vec{B}$ to the mesh cell boundaries (i) encountered in succession. We compute $T_\ell(s_1), T_\ell(s_2), \ldots, T_\ell(s_i)$, using the mean temperature along each path length s_i, and compare with $T_\ell(s)$ until we satisfy the condition $T_\ell(s_i) \geq T_\ell(s) \geq T_\ell(s_{i+1})$. Then an approximate value of s can be obtained by interpolation. A more refined value of s can be derived by successive approximation.

The Monte Carlo procedure consists in evaluating the scattering integrals [Eqs. (68) and (70)] by sampling the direction and distance to find those points $\vec{r}_j$ at which the successive orders of scattering occur; the totality of this set of points constitutes a single history. At each scattering point $\vec{r}_j$, the estimation function is evaluated with respect to the detector location $\vec{r}_D$; the result is accumulated in the appropriate retarded time bin, $t_{Rk+1} - t_{Rk}$. The accumulated estimates, divided by the number of histories (assumed large), give the Monte Carlo values for the irradiance as a function of time. The absolute time that the light reaches the detector after n scatters is

$$t_n(\vec{r}_D) = t_x(\vec{r}_o - \vec{r}_x) + \sum_{k=1}^{n} t(\vec{r}_k - \vec{r}_{k-1}) + t(\vec{r}_D - \vec{r}_n), \qquad (n = 0, 1, \ldots), \tag{78}$$

and the corresponding retarded time

$$t_{Rn}(\vec{r}_D) = t_n(\vec{r}_D) - t_x(\vec{r}_D - \vec{r}_x), \tag{79}$$

where t_x refers to x-ray travel time and $\vec{r}_x$ to the x-ray source location. We see that accounting for time is a simple matter with the Monte Carlo method. Because axial symmetry in x-ray deposition, and consequent fluorescence light emission, must exist about the line from the center of the earth through the x-ray source, each fluorescent history can be imagined to consist of a set of points attached rigidly to the lines that join them. This rigid body can then be rotated about the symmetry axis in small angular increments, and estimates and times at the detector can be computed from each new rigid body position. The exploitation of symmetry enables the maximum amount of data to be derived from each history.

At each scattering point, the identity of the spectrum line can change (refer to Sec. IV.C.5). Therefore, it is necessary to subtabulate the estimates in each time bin to separate the contributions from each of the four vibration bands N_2^+(0,0), (0,1), (0,2), (0,3). We can also subtabulate for the P- and R-branches, or even for individual rotation lines.

The timing aspects can be interpreted in geometric fashion. In Fig. 16 X is the x-ray source, D is the detector, and S is a source of fluorescence that emits light at time $t_x(XS) = | \vec{r}_o - \vec{r}_x | /c$. Construct an ellipsoidal surface of revolution through S with foci X and D. The x-ray pulse forms a uniformly expanding sphere that intersects this ellipsoid; the intersection points are sources of fluorescence such that the *direct* light photons from them reach the detector simultaneously at the retarded time $t_x(XS) + t(SD) - t_x(XD)$. Furthermore, those points of single scattering from which light simultaneously arrives at D must lie on an ellipsoid whose foci are S and D. In Fig. 16 one such ellipsoid is shown through the point C_1 for which the retarded time of arrival at the detector is $t_x(XS) + t(SC_1) + t(C_1D) - t_x(XD)$. Similarly, the second-order scattering contributions for a certain retarded time arrive from scattering points located on the ellipsoid confocal with C_1 and D. Indeed,

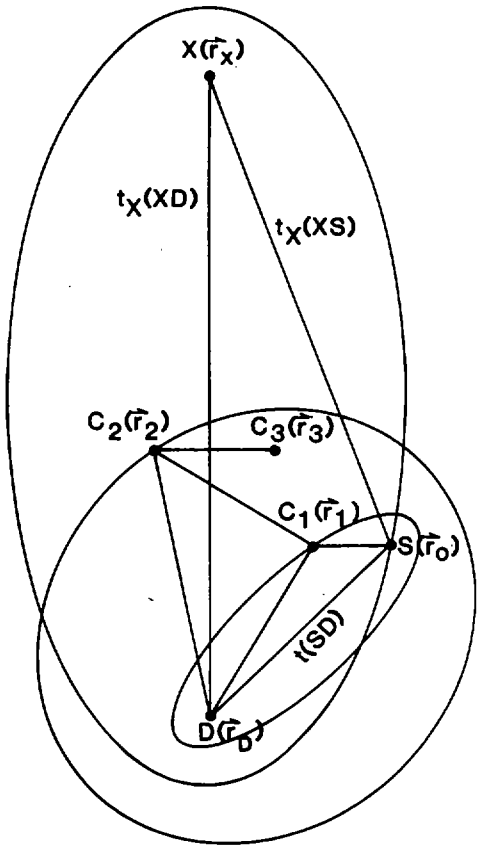

Fig. 16. Geometrical interpretation of timing for the forward Monte Carlo method.

every such ellipsoid has two numbers associated with it: (i) the order of scattering, and (ii) the retarded time of arrival at the detector.

4. Time Dependence in Backward Monte Carlo. In "backward" Monte Carlo the history of a photon begins at the detector rather than the source, and the random walk proceeds opposite to that in the "forward" method. Estimates of irradiance at the detector are made from each collision point using an estimating function [Eq. (74) or (76)], which is different from that used in the forward case.

Instead of using timing bins, we can calculate irradiance values corresponding to certain assigned values of the retarded time. The timing aspects require the use of geometrical arguments. In Fig. 17 X is the x-ray source, D is the detector, and the scattering points determined by tracing the history in the backward direction are designated $C_o, C_1, C_2, ...$ Related fluorescent source points are $S_o, S_1, S_2, ...,$ and their significance can be understood from the following discussion. The direction DC_oS_o is defined by the axis of the optical detector whose FOV is assumed very narrow. The retarded time value at which we wish to determine the irradiance is t_R.

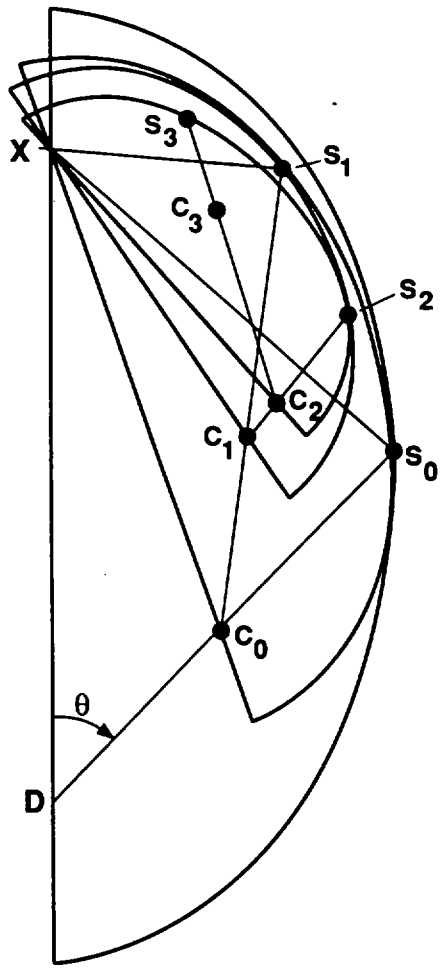

Fig. 17. Geometry of time dependence in the backward Monte Carlo method.

The only *direct* light that can arrive at the detector at time t_R must have originated at an emission point S_o such that

$$t_R = t_x(XS_o) + t(S_oD) - t(XD),$$

or

$$t_x(XS_o) + t(S_oD) = t_R + t(XD). \tag{80}$$

The right-hand side is known, so we can find $(XS_o + S_oD)$. Let us extend the line segment DS_o to S_o' such that $S_oS_o' = XS_o$. We then have an isosceles triangle XS_oS_o' for which it can be shown that

$$XS_o = \frac{1}{2} \cdot \frac{(XS_o + S_oD)^2 + (XD)^2 - 2(XD)(XS_o + S_oD)\cos\theta_o}{(XS_o + S_oD) - (XD)\cos\theta_o}, \tag{81}$$

where θ is $\angle XDS_o$. Then, $t_x(XS_o) = (XS_o)/c$.

Let us next find the location of the single-scattering collision point C_o on the line DS_o, subject to the condition $DC_o \leq DS_o$. If RN is a quasi-random number, then

$$RN = \frac{\int_o^{DC_o} \left[\frac{dT_\ell(s'')}{ds''}\right] ds''}{\int_o^{DS_o} \left[\frac{dT_\ell(s'')}{ds''}\right] ds''},$$

whence

$$T_\ell(DC_o) = 1 + RN[T_\ell(DS_o) - 1]. \tag{82}$$

DC_o can be found by inverse interpolation.

Next we choose a random direction $\vec{B}(\theta', \phi')$, where $\cos\theta' = 1 - 2 \cdot RN_1$ and $\phi' = 2\pi \cdot RN_2$. The emission point S_1 is given by $\vec{r}(C_o) + (C_oS_1)\vec{B}$ and is not generally located in the plane XDC_o. The distance C_oS_1 is found from timing considerations that require the single-scattered signal to arrive at the detector at the same retarded time as the direct light, i.e., the x-ray wave must reach S, at the time $t_x(XS_1)$ such that

$$t_R = t_x(XS_1) + t(S_1C_o) + t(C_oD) - t_x(XD), \tag{83}$$

or

$$t(S_1C_o) + t_x(XS_1) = t_R + t_x(XD) - t(C_oD).$$

The right-hand side is known, so we can find $(S_1C_o + XS_1)$. Similar to direct light, we can extend S_1 to S_1', etc., and derive the length XS_1, whence $t_x(XS_1) = XS_1/c$. It will be noticed that S_1 lies on an ellipsoid of revolution whose foci are X and C_o, and such that $XS_1 + S_1C_o = XS_o + S_oC_o$.

The same procedure can be used for all the higher orders of scattering. For second-order scattering we begin by choosing a point C_1 between C_oS_1 and a direction $\vec{B}(C_1S_2)$; then the emission point S_2 can be found from timing considerations.

At each of the scattering points, we use the estimating function and accumulate the results appropriate to the time t_R. Because the spectrum line usually changes its identity (wavelength) at each collision, it is necessary to segregate such results for each vibration band. In the forward Monte Carlo method, each x-ray deposition point serves as a fluorescence emission point. But in the backward method, the points of emission are determined such that they usually don't correspond with x-ray deposition points; in which case the source function can be given by E_ℓ^*, the emission/unit volume. The intensity I_ℓ [power/unit area·sr] of the direct light contributed to the detector is given by

$$I_\ell \doteq \frac{E_\ell^*(s)}{4\pi} T_\ell(s) \left(\frac{ds}{dt}\right)_s dt, \tag{84}$$

where ds/dt is the appropriate velocity that varies with position s along the line of sight. The emission volume element is selected in accordance with the timing requirements given by Eq. (80). To evaluate

ds/dt we have $t = (r+s)/c$, $r^2 = s^2 + d^2 - 2sd\cos\theta = (ct-s)^2$, where (Fig. 17) $r = XS_o$, $s = S_oD$, $d = XD$, and therefore

$$s = \frac{(ct)^2 - d^2}{2(ct - d\cos\theta)}. \tag{85}$$

Differentiating with respect to t, it is simple to derive the expression

$$\frac{ds}{dt} = \frac{c}{2}\left[\frac{(ct - d\cos\theta)^2 + (d\sin\theta)^2}{(ct - d\cos\theta)^2}\right], \tag{86}$$

where $ct = d + ct_R$. Similar arguments apply to the emission and intensity associated with each of the various scattering points along a backward photon track.

5. Monte Carlo Selection of an Emitted Spectrum Line. The relative distribution of populations in the excited rotational levels $B^2\Sigma(V'=0, N')$ characterized by quantum number N' is given by

$$P(N') = \frac{n(N')}{n(V'=0)} = \frac{(2N'+1)\cdot W(N')}{Q(V'=0)} \exp - [N'(N'+1)B_0c_2/\mathrm{T}], \tag{87}$$

where B_0 is the rotational constant for the $V'=0$ vibrational level of the B-state, $B_0 = 2.073\ \mathrm{cm}^{-1}$, $c_2 = hc/k = 1.4387$ [cm·K], and T is the ambient absolute temperature. $n(N')$ is the concentration of N_2^+ molecules in the state $(V'=0,\ N')$, and $n(V'=0)$ is the concentration summed over all rotational states. $Q(V'=0)$ is the partition function (sum-over-states) and $W(N')$ is the nuclear spin function. Let us define

$$p(N') = \frac{\sum_{N'=0}^{N'} n(N')}{\sum_{N'=0}^{N'MAX} n(N')}. \tag{88}$$

We generate a random number, RN, and determine N' from the condition $RN \cdot \sum_{N'=0}^{N'MAX} n(N') \simeq \sum_{N'=0}^{N'} n(N')$.

There are four vibrational bands V', V'' of interest with $V'=0$, $V''=0,1,2,3$. For the selected N' and for each V'' we can have $N'' = N'+1$, a P-branch line, or $N'' = N'-1$, an R-branch line. The probability of choosing one of the eight possible lines is

$$p[(V'=0,N'),(V'', \begin{matrix} N'+1 \\ N'-1 \end{matrix})] = \frac{\mathbf{A}[(V'=0,N'),(V'', {}^{N'+1}_{N'-1})]}{\sum_{V''=0}^{3}\{\mathbf{A}^P[(V'=0,N'),(V'',N'+1)] + \mathbf{A}^R[(V'=0,N'),(V'',N'-1)]\}}, \tag{89}$$

where $\mathbf{A}$ is the spontaneous emission coefficient for a given rotational line, and by the factorization principle (Sec. IV.B.2)

$$\mathbf{A}\left[(V'=0,N'),\left(V'', \begin{matrix} N'+1 \\ N'-1 \end{matrix}\right)\right] = \mathbf{A}(0,V'')\cdot\frac{S_J\left(N', {}^{N'+1}_{N'-1}\right)}{2(2N'+1)}, \tag{90}$$

where $\mathbf{A}(0, V'')$ is the vibrational spontaneous emission coefficient and S_J the line strength factor given by $S_J(N', N'+1) = S_J^P(N') = 2(N'+1)$ and $S_J(N', N'-1) = S_J^R(N') = 2N'$. From Table VIII we have

A(0,0) = 1.07+07,	$p(0,0) = 0.705$
A(0,1) = 3.50+06,	$p(0,1) = 0.230$
A(0,2) = 8.04+05,	$p(0,2) = 0.0529$
A(0,3) = 1.50+05,	$p(0,3) = 0.0099$

It follows that

$$\mathbf{A}\left[(0,N'),\binom{V'', N'+1}{N'-1}\right] = \mathbf{A}(0,V'') \cdot \frac{\left[\begin{smallmatrix}2(N'+1)\\ 2N'\end{smallmatrix}\right]}{2(2N'+1)},$$

$$\sum_{V''=0}^{3} \{\mathbf{A}^P[(0,N'),(V'',N'+1)] + \mathbf{A}^R[(0,N'),(V'',N'-1)]\} = \sum_{V''=0}^{3} \mathbf{A}(0,V''), \tag{91}$$

whence

$$p^P[(0,N'),(V'',N'+1)] = p(0,V'') \cdot \frac{N'+1}{2N'+1}, \tag{92}$$

and

$$p^R[(0,N'),(V'',N'-1)] = p(0,V'') \cdot \frac{N'}{2N'+1} \tag{93}$$

with $\sum_{V''=0}^{3} p(0,V'') = 1$.

V. RESULTS OF CALCULATIONS

The calculated results shown in Figs. 18-38 are graphs of irradiance [photons/cm^2·s], or intensity [photons/cm^2·s·sr], vs retarded time [s]. Retarded time is the time measured from the instant the first x ray reaches the detector.

Irradiance is the photometric quantity usually measured by a satellite sensor, which is designed to monitor the entire face of the earth directed toward the satellite. On the other hand, intensity is the appropriate quantity measured by a collimated (narrow FOV) sensor, such as would be flown on board an aircraft. On occasion, the "all sky" photometer has been used in the field; this instrument has a nearly hemispherical FOV and measures irradiance.

Above each diagram, or in some cases several related diagrams, we give the x-ray yield (Y) in kilotons, band wavelength (WAVELENGTH) in angstroms, burst altitude (H) in kilometers, the detector zenith angle (THETA) in degrees as measured from the sub-burst point on the earth's surface, and the Lambert ground albedo (ALBEDO) if different from zero. It was deemed advisable to separate various geometrical and/or physical effects in the diagrams. For example, one curve may represent the irradiance vs time in a given molecular band calculated on the basis of fluorescence theory alone, while another curve additionally includes the effects of troposphere scattering with attenuation and ground

reflection. The tropospheric model we use is that given by Elterman (1968) for clear (noncloudy) conditions with a surface visibility of 26 km. The inclusion of clouds was not attempted as it would have expanded the results far beyond our more limited objectives; in any event, a rough estimate of cloud effects can be found by using a high ground albedo. Finally, and primarily for numerical checking purposes, we always give the direct-attenuated component (the bottom curve in each figure); furthermore, it then is possible to judge the relative importance of scattering.

The x-ray source spectrum is the same for all the examples shown, viz., a blackbody with a temperature of 20 000 000 K (Fig. 4). It is assumed that the x rays are generated instantaneously at the moment of detonation and isotropically in direction. The approximate burst altitudes chosen are 150, 200, 600, and 2000 km. The detector locations and other information are given in the figure captions and in the relevant text.

For most of the calculations the optical emission is assumed to be created at the same place and time that the x-ray energy is deposited. However, some of the examples, such as Fig. 22, show the effects of nonlocal production and excitation of N_2^+ (important only above ~100 km; refer to Sec. III.B.4), which depresses the irradiance-time curve at very early times and can be important for determining instrumental thresholds.

We have chosen to present irradiance calculations for only those satellites that occupy circular geosynchronous orbits (orbital radius = 6.6 earth radii = 42 100 km, Fig. 2). The results can be easily scaled to other satellite distances, provided the satellites are not too near the earth.

The calculations for a ground-based sensor are for an observer located at the sub-burst point. However, this is not an essential restriction. Our code is programmed to handle any observing location with given line of sight and FOV.

A. Burst Altitude of 145 km

In this section we consider a fixed burst altitude H = 145 km. In Fig. 18 the x-ray yield is 150 kt and the satellite receiver is 15° from the zenith of the burst. The upper curve of each graph gives the irradiance vs retarded time history at the receiver under the assumption of emission without attenuation of any kind, and the irradiance (photons/cm^2·s) in a given N_2^+ band is proportional to the altitude-dependent fluorescence efficiency multiplied by the band wavelength. The lower curve of each graph gives the direct irradiance that is due to fluorescent emission followed by resonance-absorption alone along the line to the detector. These curves show some statistical deviations as the x-ray deposition was performed with the Monte Carlo code MCNP. The variation of N_2^+ concentration with time, due primarily to collisions with electrons, affects the attenuation of the fluorescent bands, accounting for the peak-time delay shown by the bottom curve (especially marked at λ 3914); by ~3 ms most of the N_2^+ ions have disappeared with the two curves coming together. The total signal in any band can never be less than the direct-attenuated component.

Figure 19 shows irradiance vs retarded time curves with the total (direct plus multiple scattering) above and the direct attenuated below. The effect of fluorescent scattering is to shift photons from λ 3914 and λ 4278 to the other bands, which gain relatively in strength (refer to Fig. 9 and the pertinent text concerning enhancement).

The effect of temperature on the calculations can be seen in Fig. 20; in Fig. 20(a) the temperature used to compute fluorescence is everywhere 200 K; in Fig. 20(b) the temperature is 800 K. With the higher temperature the spectrum lines are broadened and attenuation is lower; consequently the scattered component is also less, and there is less enhancement of the other bands (not shown). Figure 20(c) shows the resulting curves for the case in which the temperature varies with altitude (US Standard Atmosphere), both for computing emission and transmission; the resulting curves lie between those for 200 and 800 K.

In Fig. 21 we show the computed results of the fluorescent irradiance vs time incident on a satellite at 6.6 earth radii. A tropospheric aerosol and molecular atmosphere [Elterman (1968) clear atmosphere model with ground visibility 26 km] combined with a Lambert ground reflection are included in the simulation. The Lambert albedo is zero for the left-hand figures and unity for the right-hand figures. The first reflected photon to reach the detector does so at a time $\sim$1 ms; this reflection effect is evident with the albedo of unity, causing the curve to be considerably extended in time. The random number sequence is the same for both sets of graphs. The direct-light curves show no reflection effect, of course.

In Fig. 22 each left-hand diagram is to be compared with its counterpart on the right-hand side. The left-hand curves assume local N_2^+ production and consequent fluorescent emission, whereas the right-hand curves are based on the more rigorous treatment of nonlocal emission above $\sim$100 km (Sec. III.B.4). In this latter situation it is seen that the curves are considerably depressed at early times; this is readily understood, because the early time signal is due to emission originating at high altitudes where the nonlocal effects are important and electron time-of-flight delays are involved.

In Fig. 23 the x-ray yield is only 15 kt, but there is still considerable enhancement of the higher bands. In Fig. 24 the x-ray yield is 300 kt, but the results do not differ substantially from 150 kt. The calculations in Fig. 25 are the same as in Fig. 24 except that the ground albedo is unity and consequently the reflection effect is obvious in Fig. 25; however, the random number sequence was not kept the same and statistical variations can be seen between respective graphs in the two figures.

Figure 26 gives the calculated "all sky" irradiances as observed from the sub-burst point on the earth's surface. The upper curve gives the total irradiance (direct plus scattered light), and the lower curve gives the direct light affected only by resonance-absorption. There are no tropospheric nor ground reflection effects included in these computations.

Figure 27 gives the calculated intensity as observed from the sub-burst point in a direction given by a zenith angle of 20°. The yield is 150 kt. The photometer FOV is 2°. The forward Monte Carlo results are given by the histogram, and the backward Monte Carlo results are shown by the continuous but somewhat jagged curves (total above and direct-attenuated below). Tropospheric extinction, scattering, and ground reflection are included. For narrow FOV detectors the calculations using the forward Monte Carlo show considerable statistical fluctuations in intensity vs time; this is due to the relatively small number of fluorescent source and scattering points that have their circles of axial symmetry intercepted by the FOV cone. The backward method does not have this problem, yet it produces more deviations than anticipated; the explanation is that the Monte Carlo photon paths often intersect the boundaries of mesh cells across which the physical parameters, especially emission per unit volume and N_2^+ concentration, display discontinuous values; also for the total light the statistical effects are more pronounced, especially after the peak. In this regard both forward and backward methods share the same difficulty.

B. Burst Altitudes of 199, 599, and 2000 km

Figures 28-38 show how fluorescent irradiance-vs-time curves (computed for satellite-based detectors) change with burst altitude, yield, and zenith angle. For $H = 199$ and 599 km, the selected Y is 100 kt; for $H = 2000$ km, Y is 500 kt. In each case results are given in the four primary fluorescing wavelengths for three satellite zenith angles.

Figures 28-30, 32-34, and 36-38 have similar format. The ordinate gives irradiance in units of [photons/cm^2·s], and the abscissa gives the retarded time in seconds. Three curves are given on each diagram: (1) the top curve gives total irradiance including direct-attenuated plus scattered fluorescent light, tropospheric attenuation and scattering, and Lambert ground reflection with albedo 0.3; (2) the middle curve gives direct-attenuated plus scattered fluorescent light with only tropospheric attenuation; and (3) the bottom curve gives direct-attenuated fluorescent light also attenuated by the troposphere. Results are given in each of the four molecular bands for satellite zenith angles of 21.4°, 56.7°, and 84.2° relative to the sub-burst point. Tropospheric scattering and ground reflection produce the differences between the upper two curves, sometimes resulting in two maxima [for example, Figs. 22(d) and 30(a)]. It will also be noticed that the time of peak brightness regresses to earlier times as the zenith angle increases. This is readily understood by constructing single scattering ellipsoids for given retarded times with foci at the burst and detector positions (refer to Sec. IV.C) and realizing that the peak brightness in the direct light occurs when the ellipsoid first touches the ~80-km atmospheric layer where the N_2^+ concentration, and consequently emission per unit volume, is highest. For large detector zenith angles, the ellipsoid touches the 80-km level earlier than for small detector zenith angles. When the ellipsoid axis is nearly horizontal, attenuation of the emitted light along the 80-km layer causes the λ 3914 band (which has the highest absorption) to peak even earlier [Figs. 30(a) and 34(a)].

Figures 31 and 35 compare local left-hand side vs nonlocal right-hand side modes of calculating the fluorescence (Sec. III.B.4 and also Fig. 22), but for only one wavelength, λ 4278 Å. The left-hand graphs have the same format as Figs. 28-30, but the right-hand graphs were computed with another code written for checking purposes that doesn't include tropospheric effects and ground reflection. The upper curve in each right-hand graph gives the total fluorescent signal (scattered plus direct light), while the lower curve gives the direct light diminished by resonance-absorption. For the cases shown the tropospheric effects are small, but the ground reflection with 0.3 albedo is still quite pronounced. As expected, the early-time portion of the right-hand curves are severely depressed because of the nonlocal fluorescent emission.

Figures 36-38 show the effects produced by a relatively high burst altitude. The rise to maximum is not as rapid as might first appear because of the nature of the logarithmic time scale. Our results also show very little difference between local and nonlocal effects, at least within four to six decades of the peak.

VI. CONCLUSIONS AND SUGGESTED FUTURE WORK

We have developed a computer program that performs calculations of resonant-fluorescent scattering in the upper atmosphere induced by x rays from a high-altitude nuclear explosion. Our emphasis is on the bands of N_2^+ ($\lambda\lambda$ 3914, 4278, 4709, 5228 Å), which fluoresce brightly. We have taken into account the important physical processes and chemical reactions. The scattering of the light is simulated by the Monte Carlo method, which can be applied in either the "forward" or "backward" mode.

Many examples and problems have been run on the Los Alamos CRAY computers. A typical output gives the time-dependent irradiance incident on a satellite-based detector. We have obtained results for various explosion yields, detonation altitudes, and detector positions (satellite, ground, and air based).

Further development of the code will be mainly laborious because the principles are now well understood. Our suggestions for future work include (1) a more detailed treatment of the initial conditions; (2) the explicit inclusion of the Meinel bands in the fluorescent light scattering (probably important only for high yields), which will require further laboratory work as there are no data on the Meinel band deactivation branching rates at this time; and (3) further studies of the backward Monte Carlo method.

ACKNOWLEDGMENTS

We wish to thank Harold Gardiner at the Air Force Cambridge Research Laboratories for furnishing us with a magnetic tape of his N_2^+ first negative band transmission program.

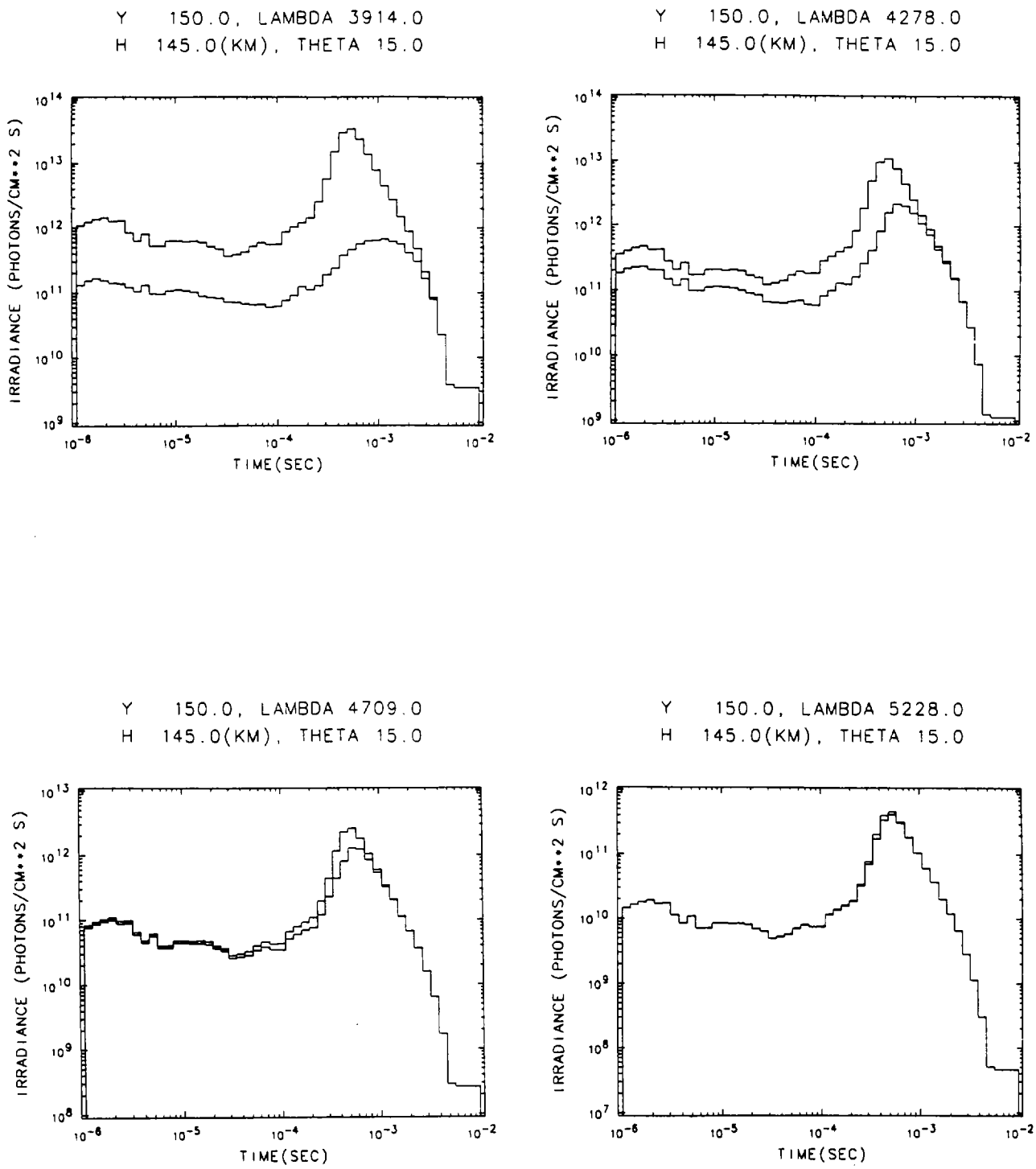

Fig. 18. The calculated irradiance vs retarded time at a synchronous satellite (~6.6 earth radii) located 15° from the zenith of the sub-burst point. The upper curve gives the unattenuated signal; the lower curve gives the signal attenuated by resonance-absorption only.

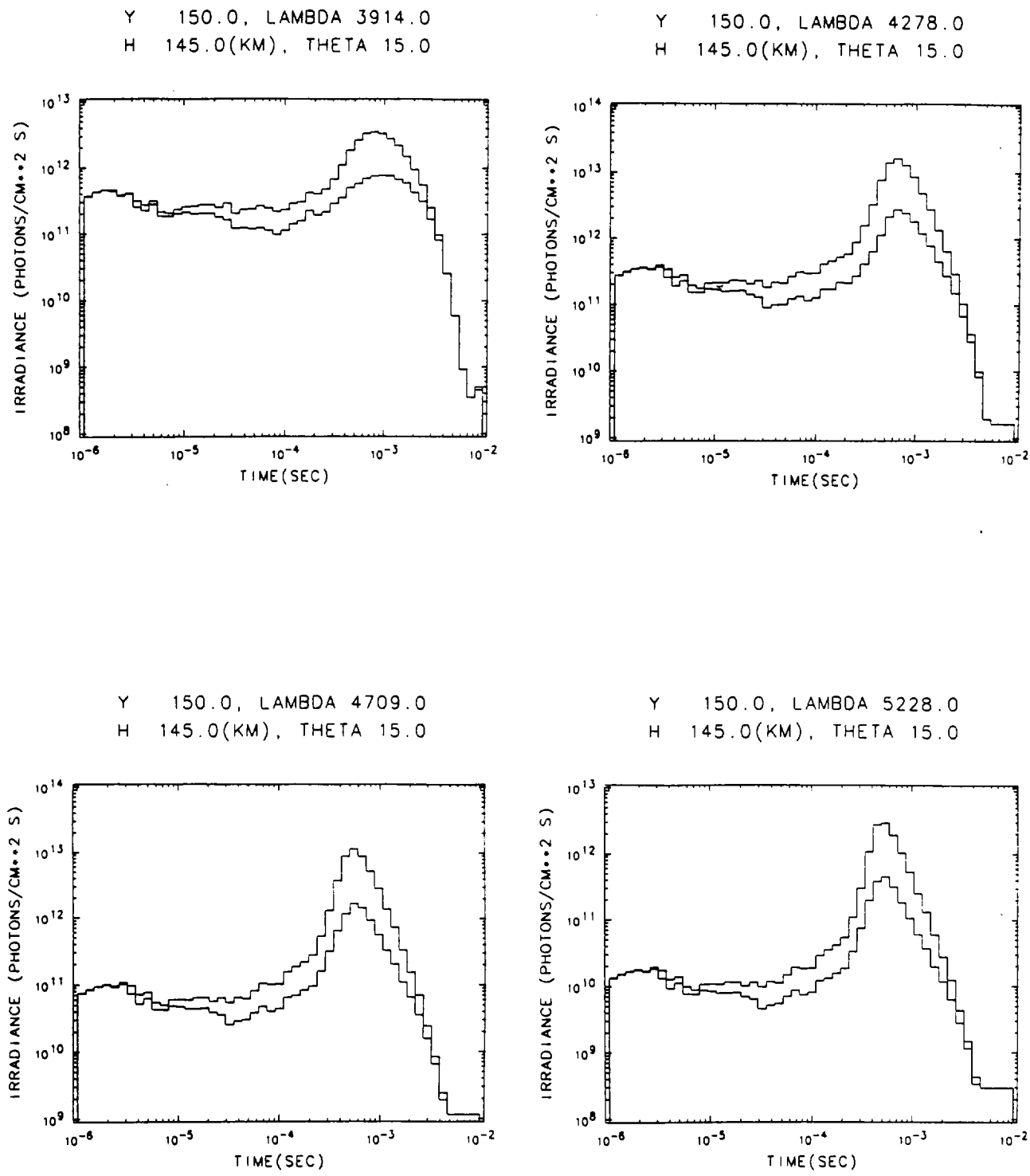

Fig. 19. Conditions are similar to Fig. 18, however the upper curve gives the total signal that includes the direct-attenuated signal (lower curve) plus the scattered light.

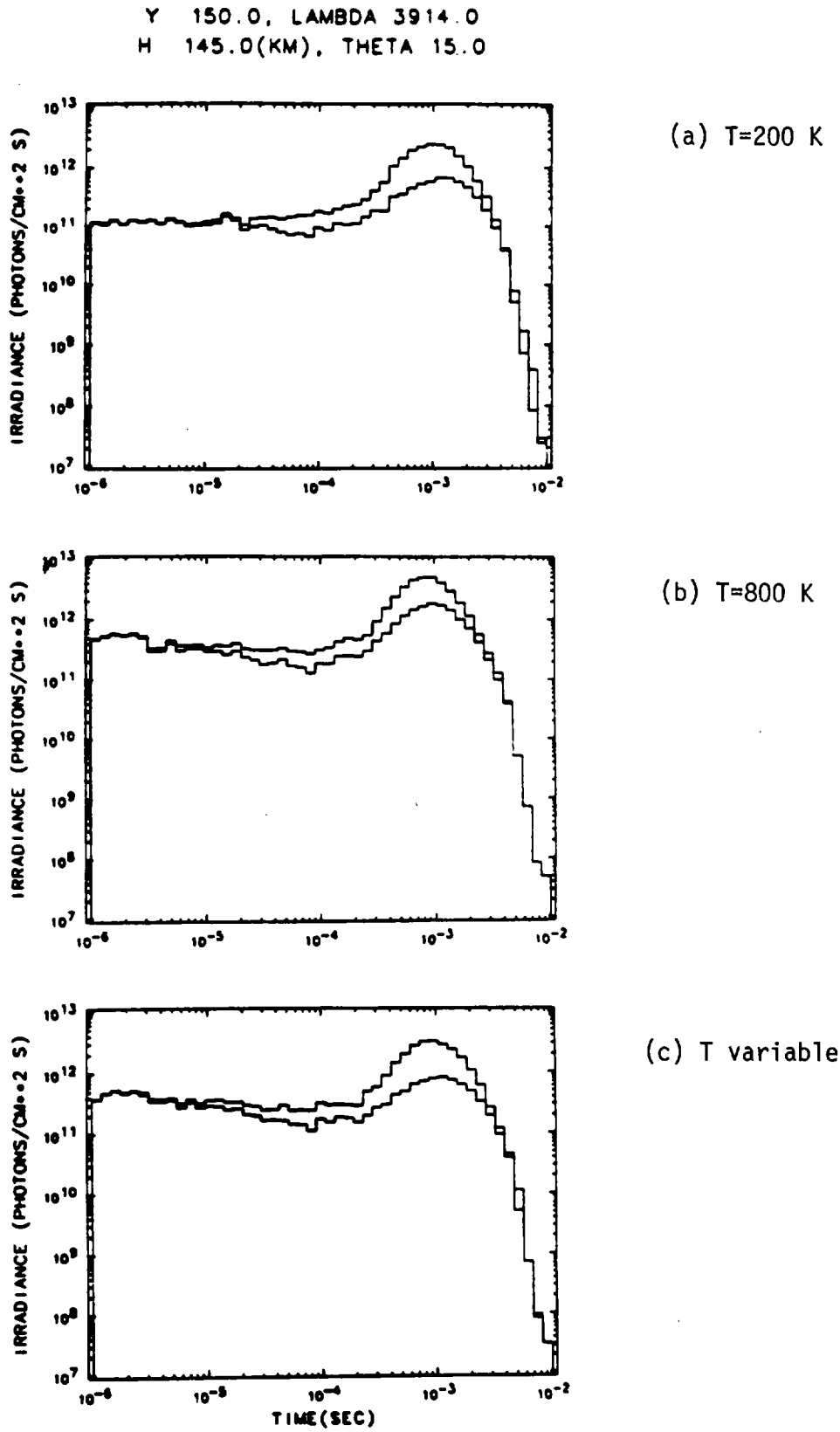

Fig. 20. Similar to Fig. 19 but shows the effects of assuming different temperatures in the fluorescent layer: (a) $\mathbf{T}= 200$ *K; (b)* $\mathbf{T}= 800$ *K; (c)* $\mathbf{T}$ *is variable, being assigned its mean value along each segment of a Monte Carlo history.*

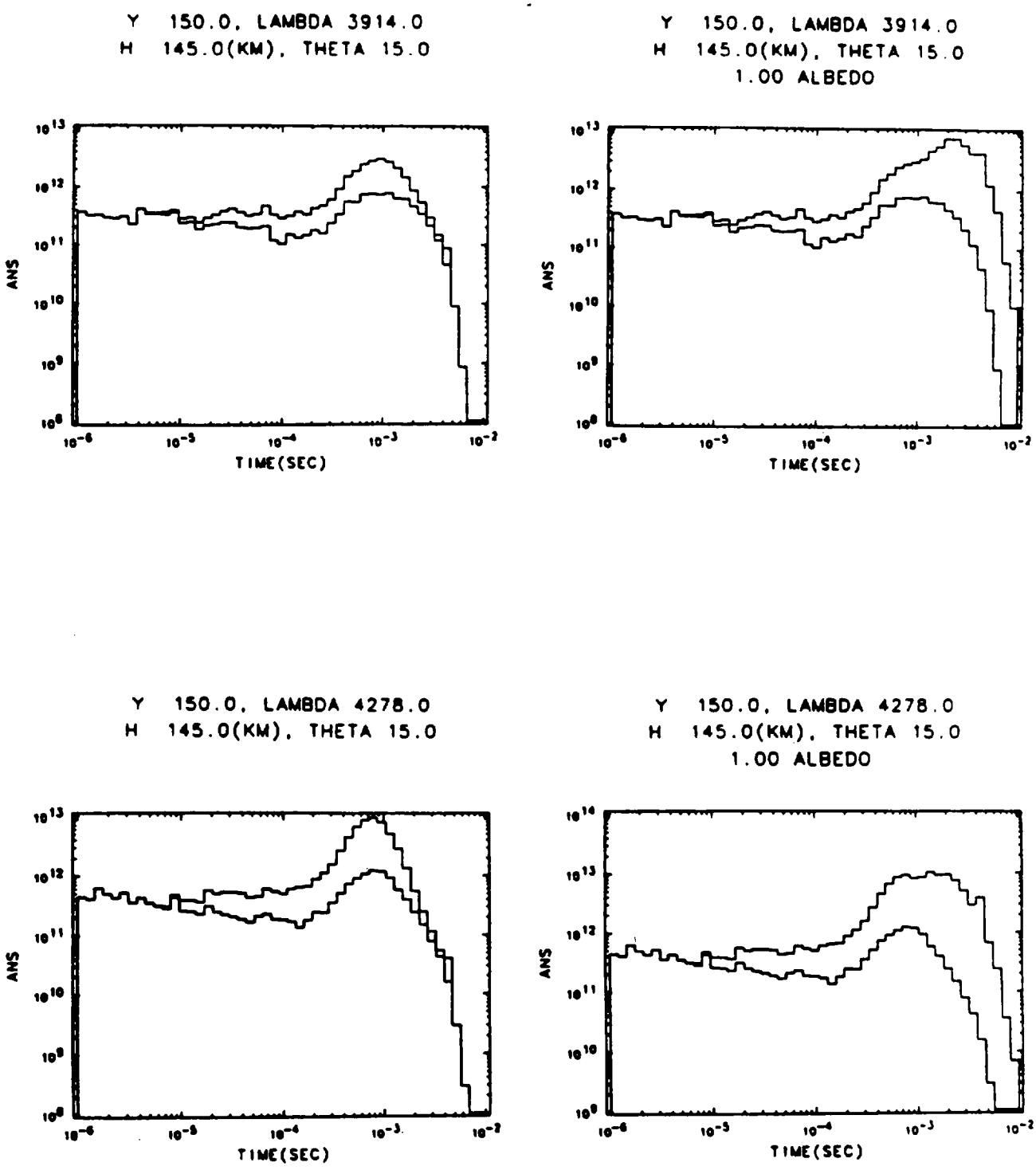

Fig. 21. Similar to Fig. 20(c) but includes the effects of tropospheric scattering combined with Lambert ground reflection in the results presented on the right. The ANS *label means IRRADIANCE (photons/cm^2· s).*

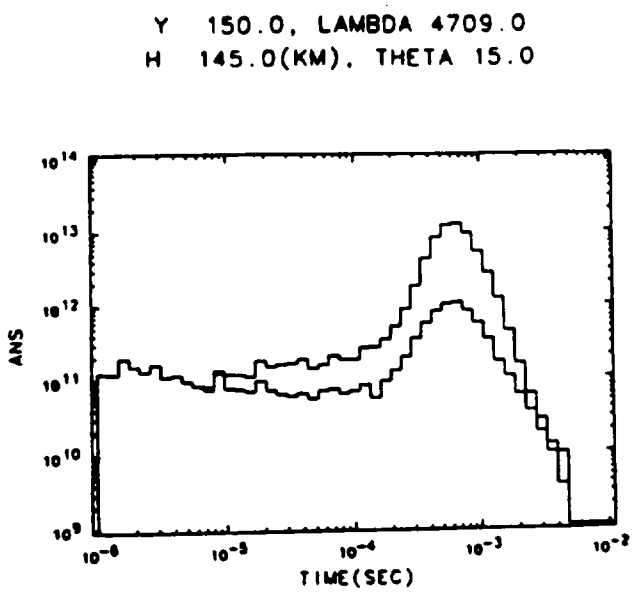
Y 150.0, LAMBDA 4709.0
H 145.0(KM), THETA 15.0
ANS
TIME(SEC)

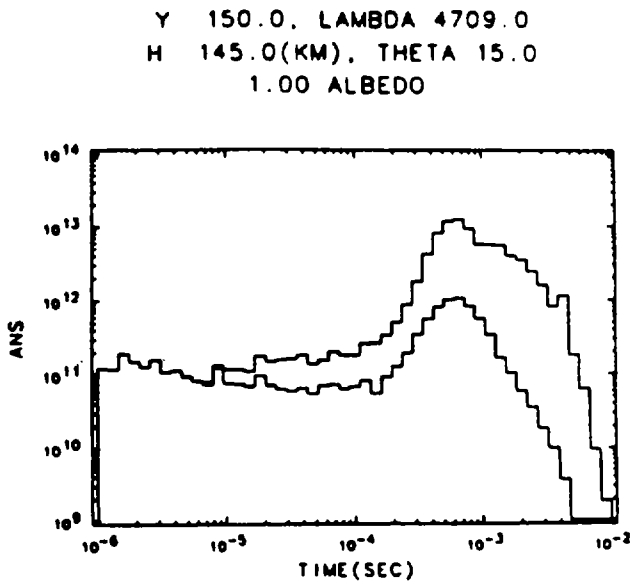
Y 150.0, LAMBDA 4709.0
H 145.0(KM), THETA 15.0
1.00 ALBEDO
ANS
TIME(SEC)

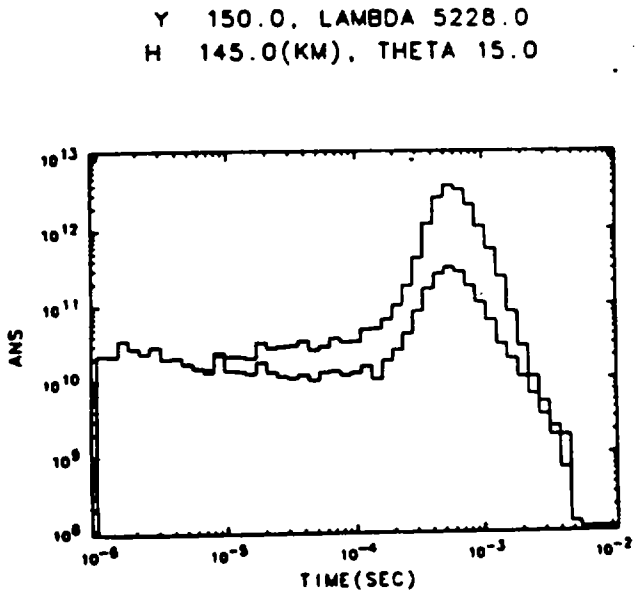
Y 150.0, LAMBDA 5228.0
H 145.0(KM), THETA 15.0
ANS
TIME(SEC)

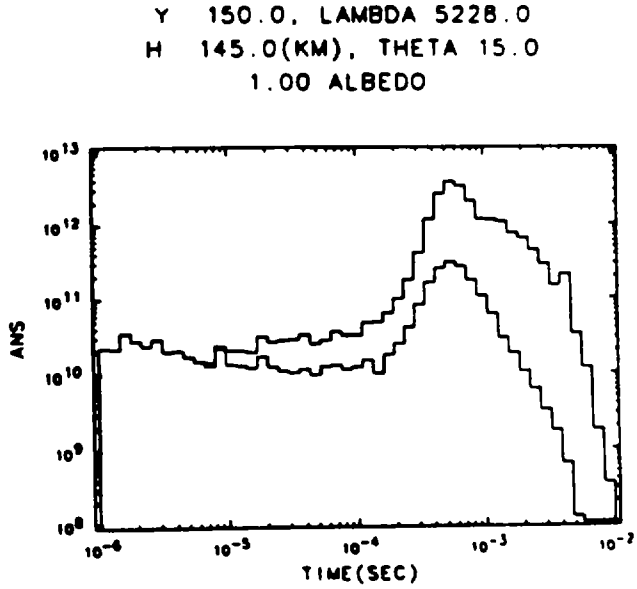
Y 150.0, LAMBDA 5228.0
H 145.0(KM), THETA 15.0
1.00 ALBEDO
ANS
TIME(SEC)

Fig. 21. (cont)

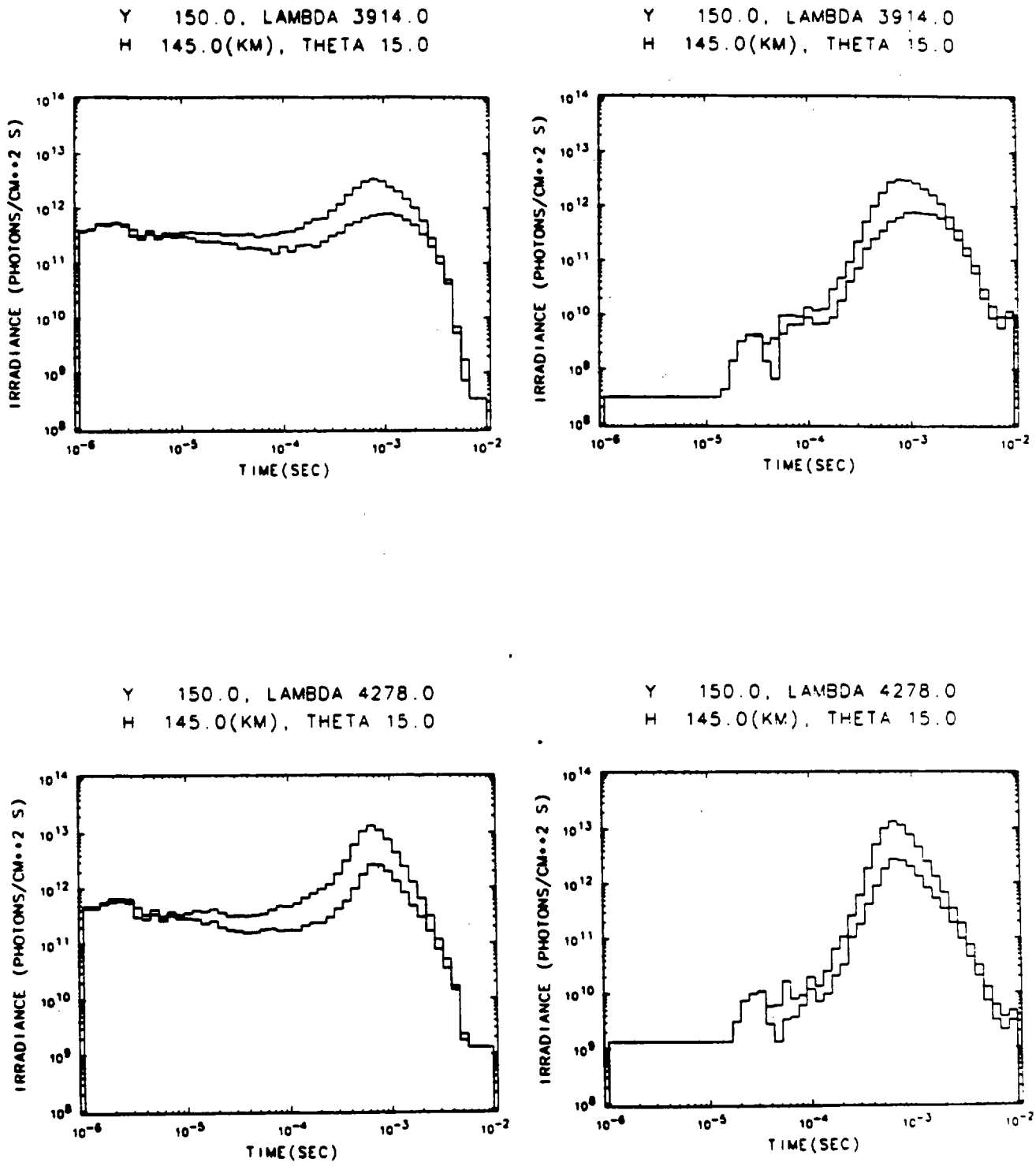

Fig. 22. Conditions are similar to Fig. 20(c) but tropospheric and reflection effects are not included. The diagrams compare local (left) with nonlocal (right) creation of fluorescence.

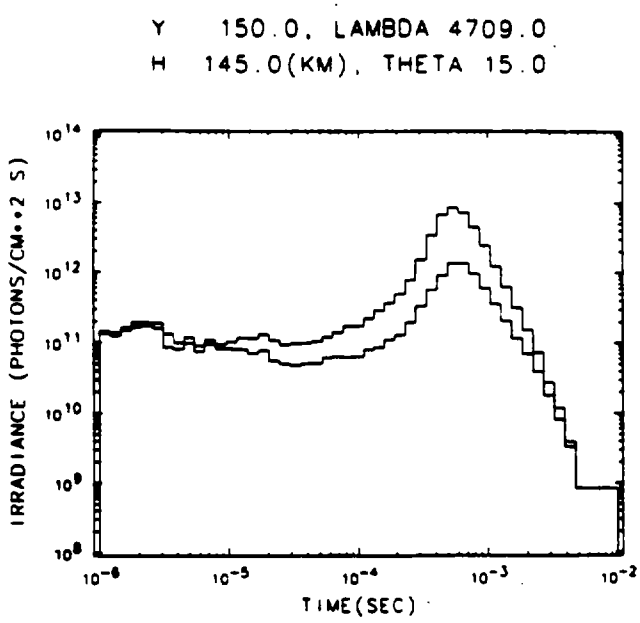
Y 150.0, LAMBDA 4709.0
H 145.0(KM), THETA 15.0
IRRADIANCE (PHOTONS/CM••2 S)
TIME(SEC)

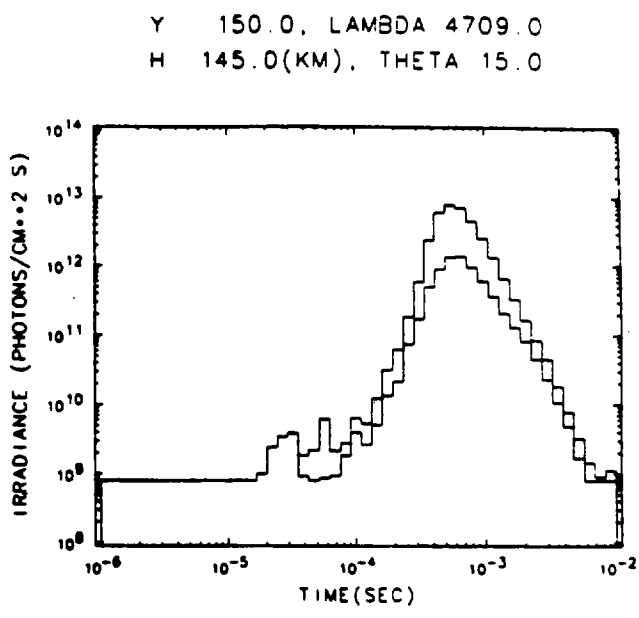
Y 150.0, LAMBDA 4709.0
H 145.0(KM), THETA 15.0
IRRADIANCE (PHOTONS/CM••2 S)
TIME(SEC)

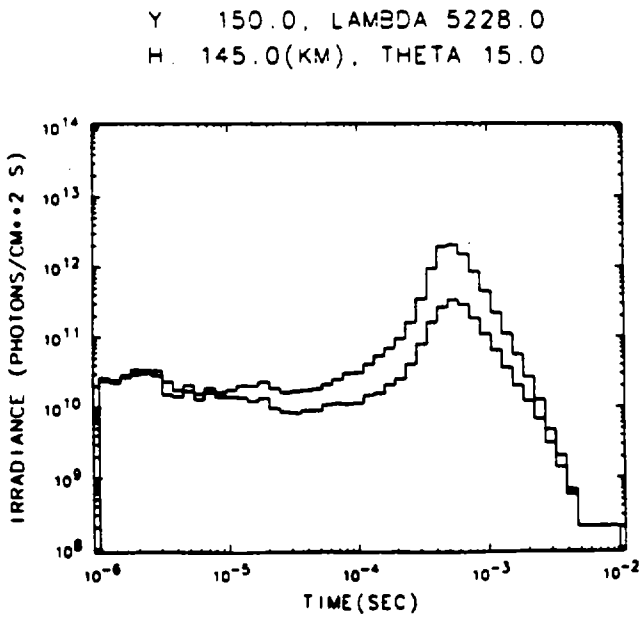
Y 150.0, LAMBDA 5228.0
H 145.0(KM), THETA 15.0
IRRADIANCE (PHOTONS/CM••2 S)
TIME(SEC)

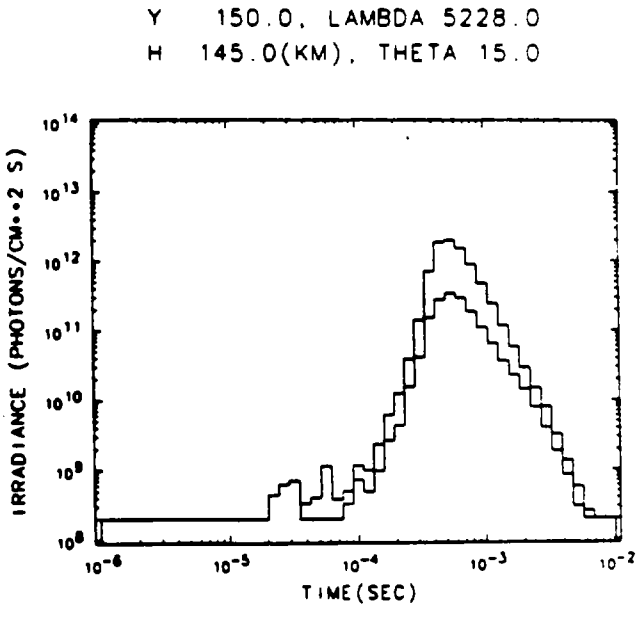
Y 150.0, LAMBDA 5228.0
H 145.0(KM), THETA 15.0
IRRADIANCE (PHOTONS/CM••2 S)
TIME(SEC)

Fig. 22. (cont)

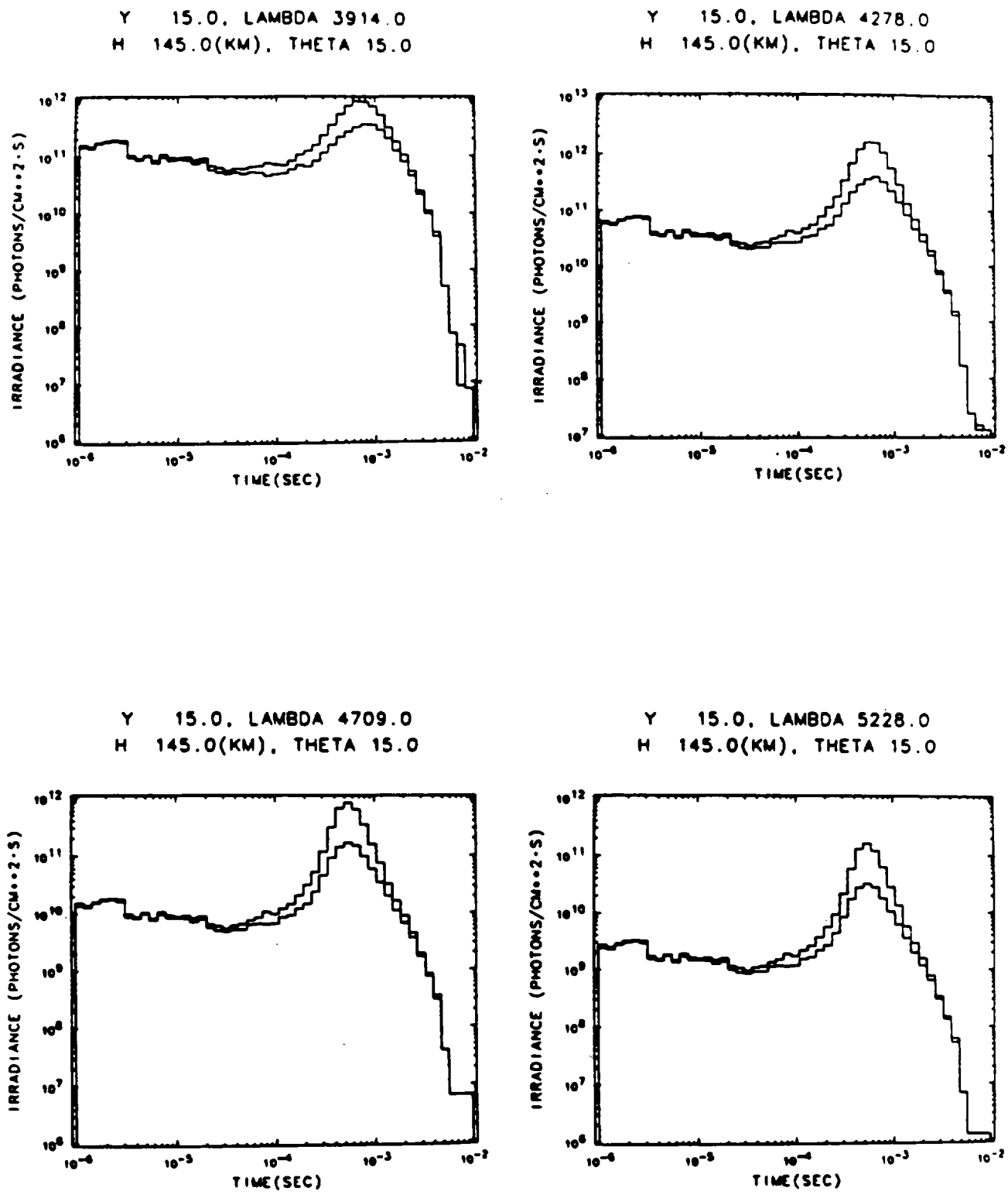

Fig. 23. Similar to Fig. 20(c), but the x-ray yield is only 15 kt.

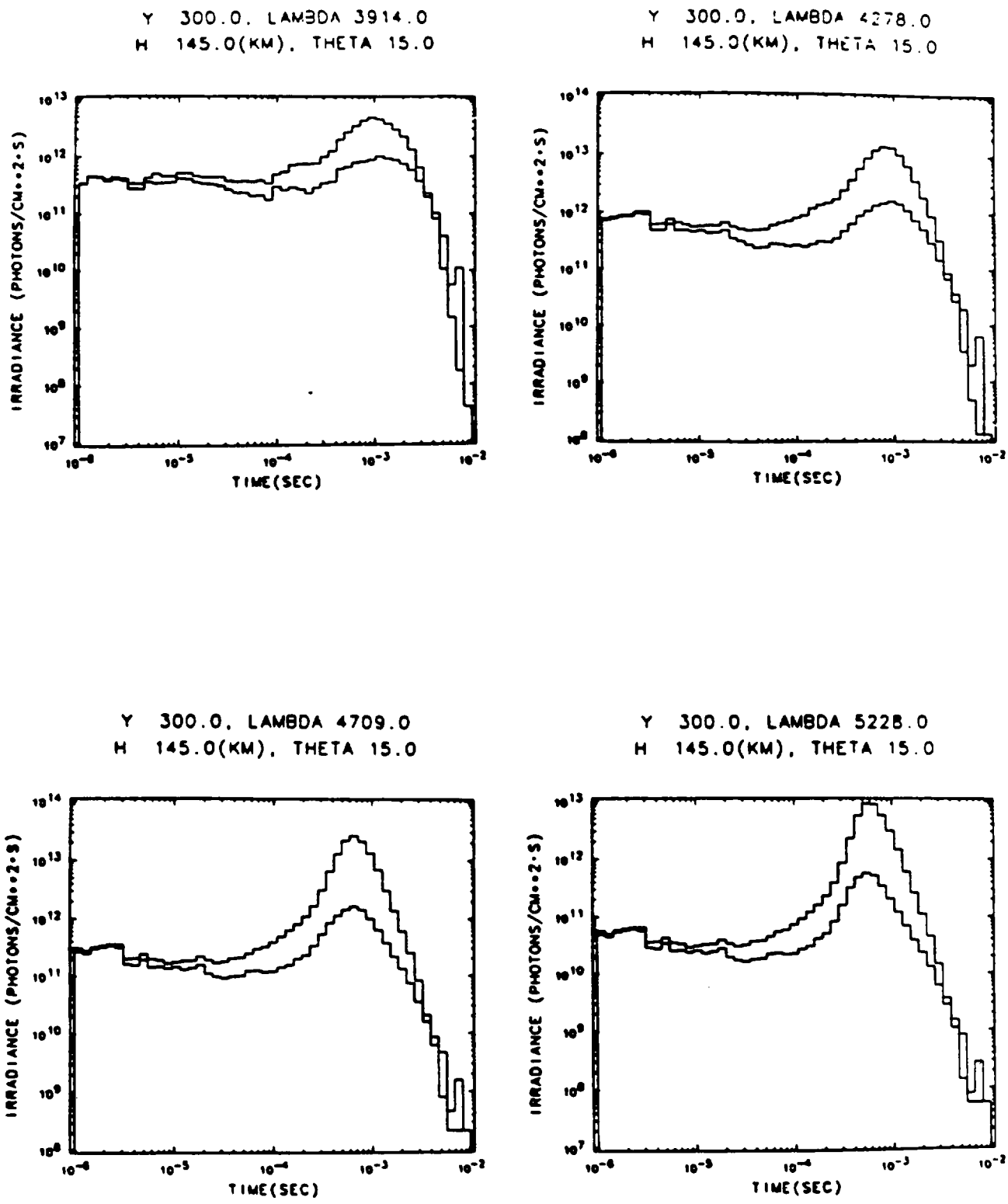

Fig. 24. Similar to Fig. 23, but the x-ray yield is 300 kt.

Albedo 1.0

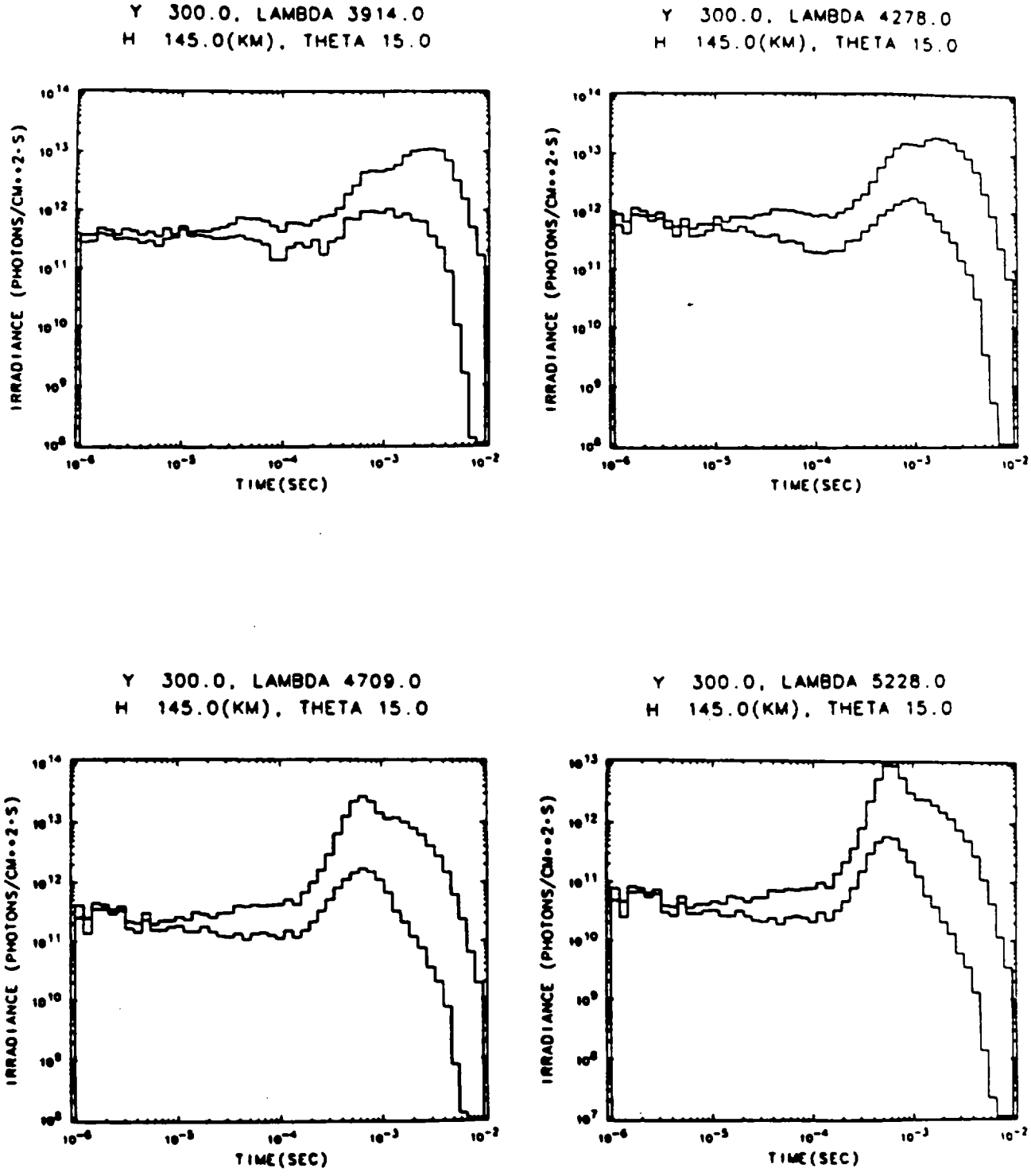

Fig. 25. Similar to Fig. 24, but tropospheric and reflection effects are included.

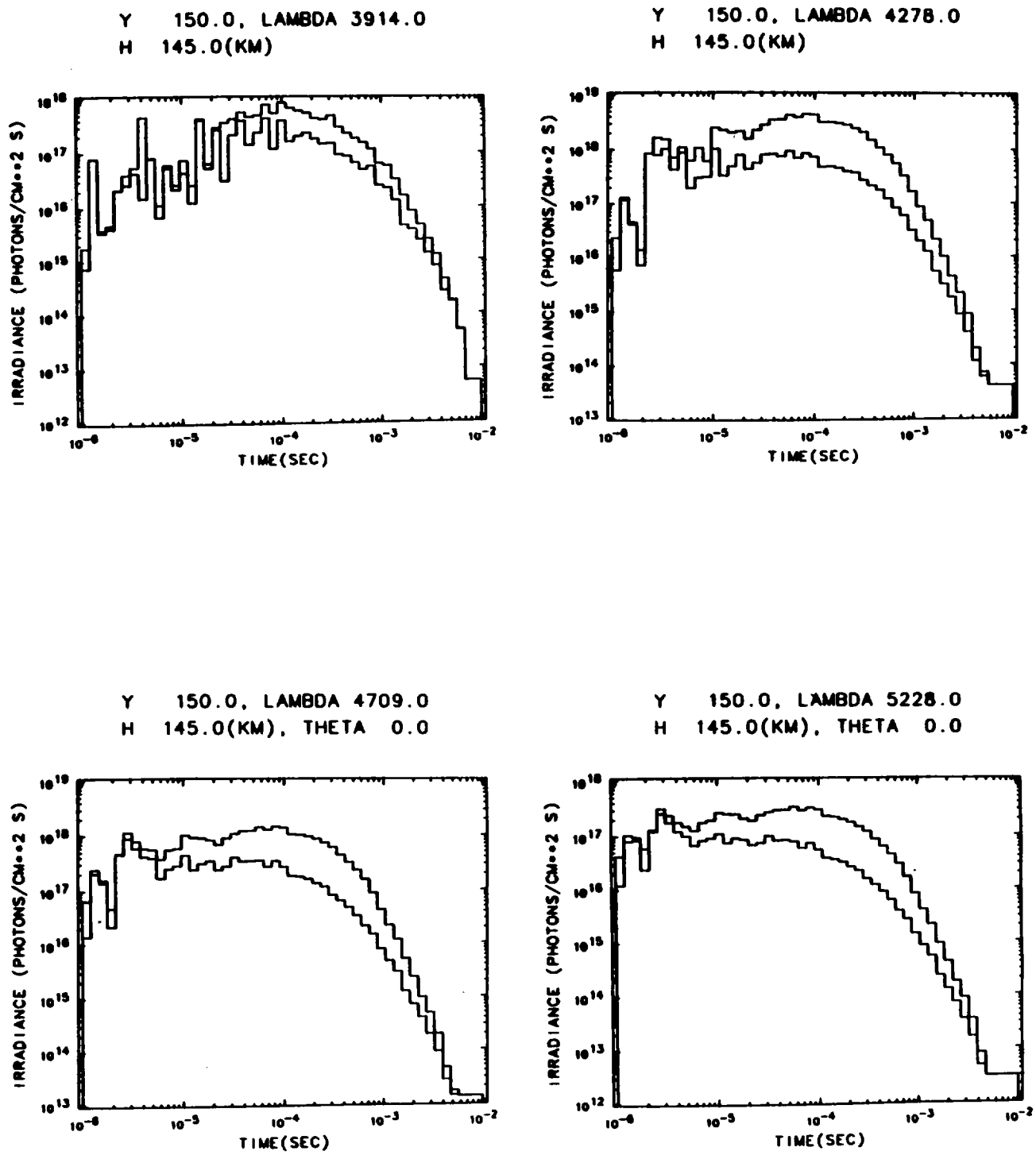

Fig. 26. Calculated "all sky" irradiances vs retarded time as observed from the sub-burst point on the earth's surface (no tropospheric or ground reflection effects).

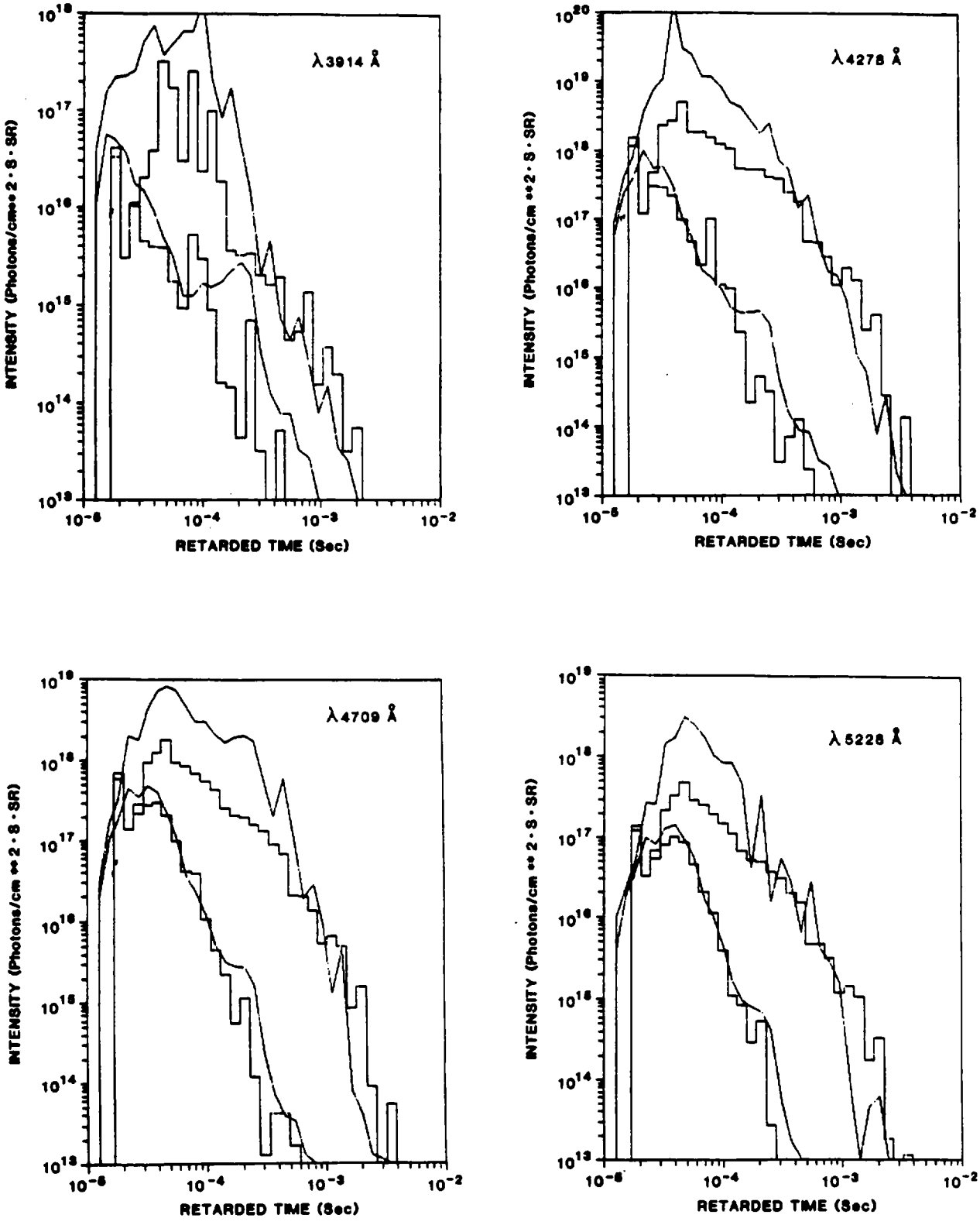

Fig. 27. Forward (histograms) and backward (continuous curves) Monte Carlo results are compared in computing the zenith intensities (radiances) for an observer located at the sub-burst point.

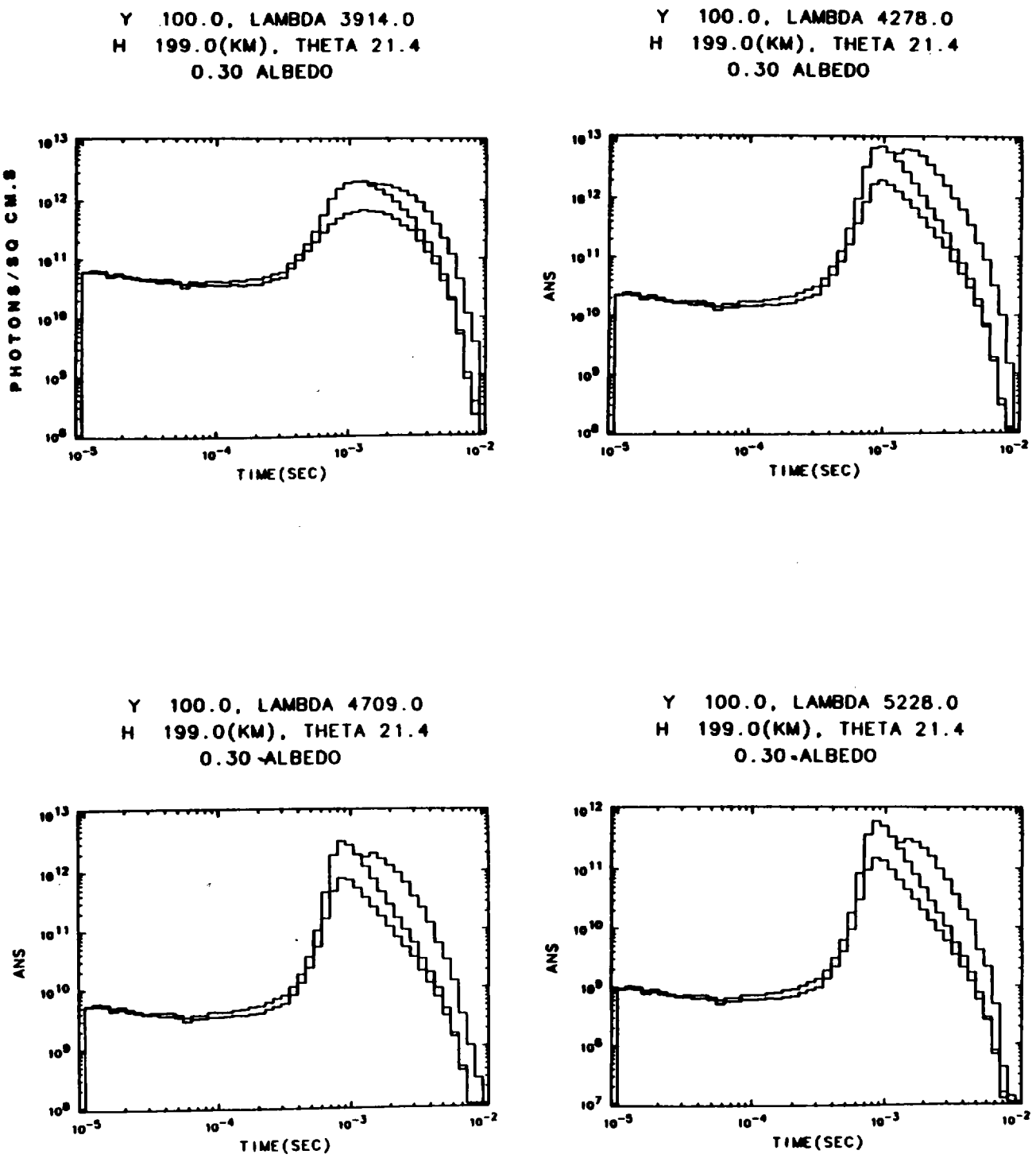

Fig. 28. Calculated irradiance vs time curves are shown for a geosynchronous satellite at a zenith angle of 21.4° relative to the sub-burst point. The yield (Y) is 100 kt, and the height of burst (H) is 199 km. The upper curve includes tropospheric and reflection effects, whereas the next curve below does not. The lowest curve gives the direct-attenuated light.

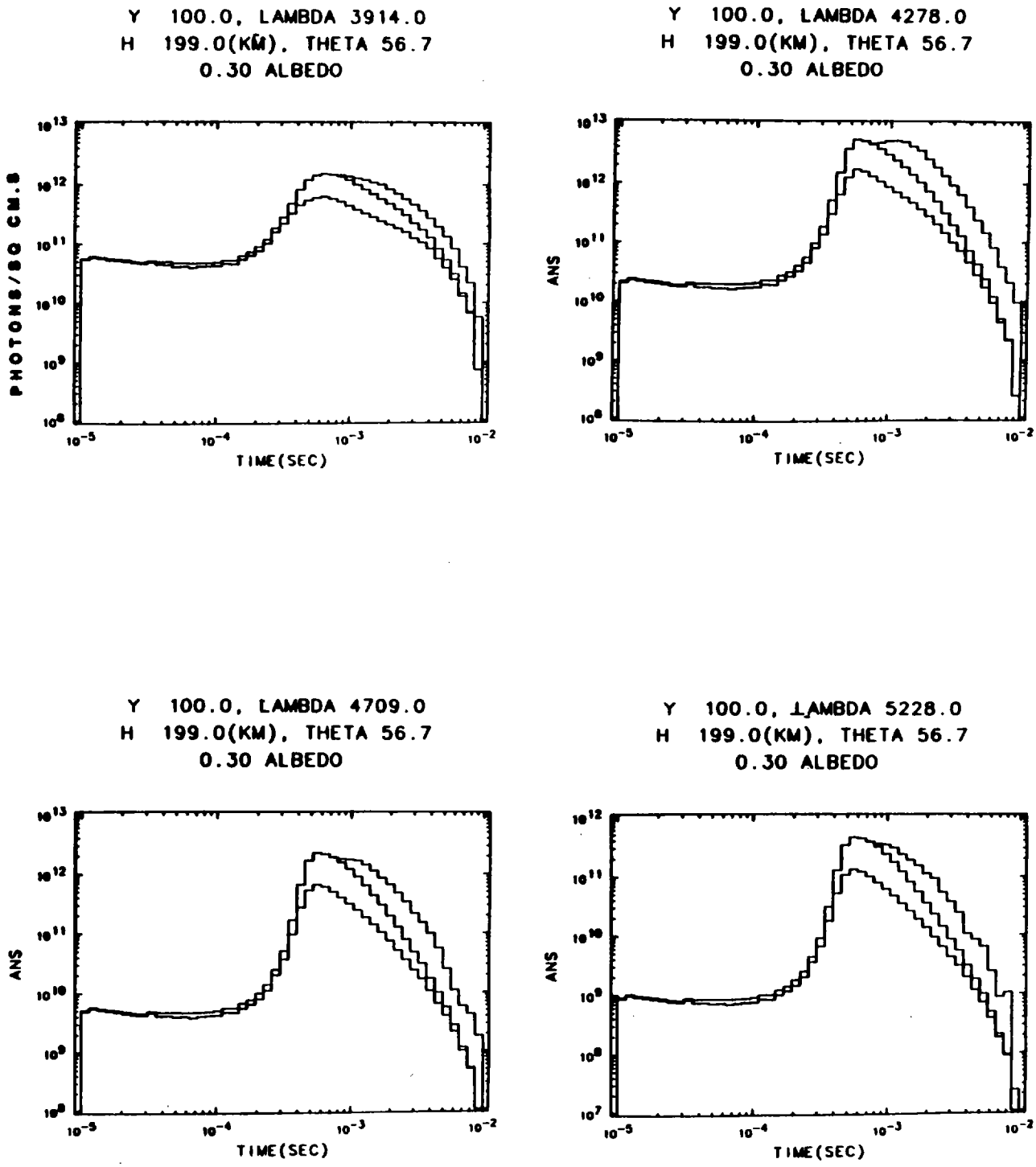

Fig. 29. Similar to Fig. 28, but the satellite zenith angle is 56.7°.

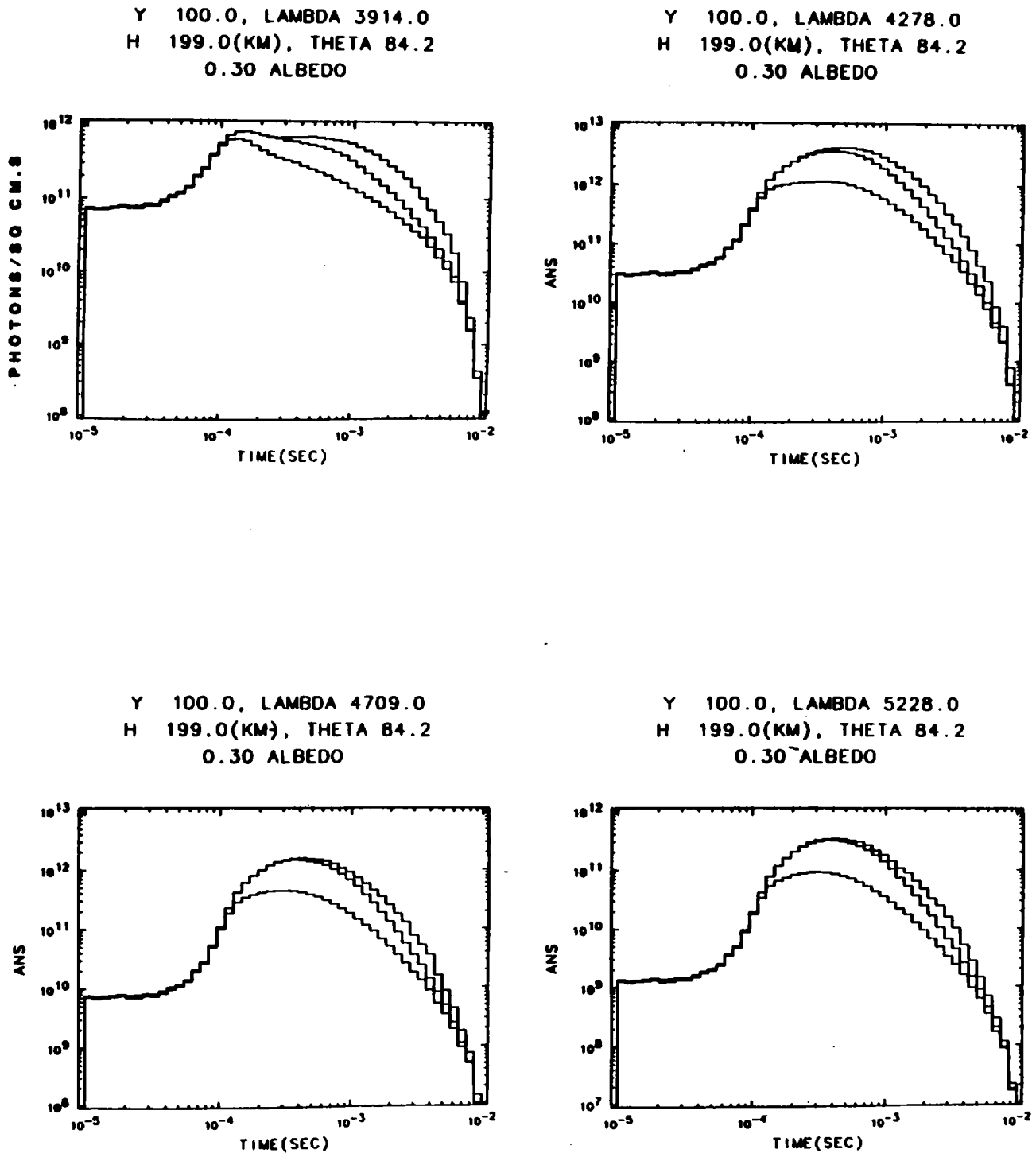

Fig. 30. Similar to Fig. 28, but the satellite zenith angle is 84.2°.

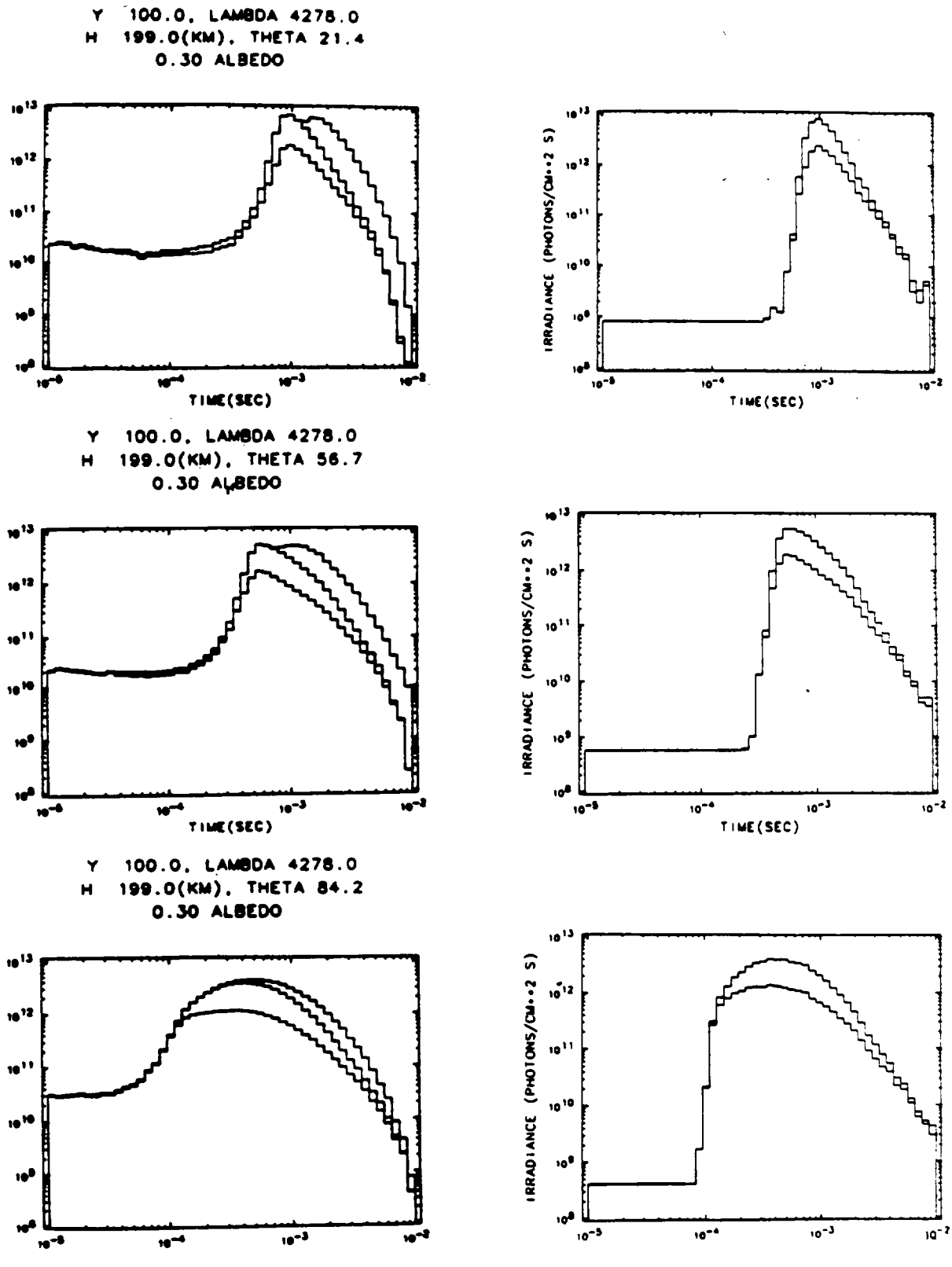

Fig. 31. A comparison of local vs nonlocal creation of fluorescence.

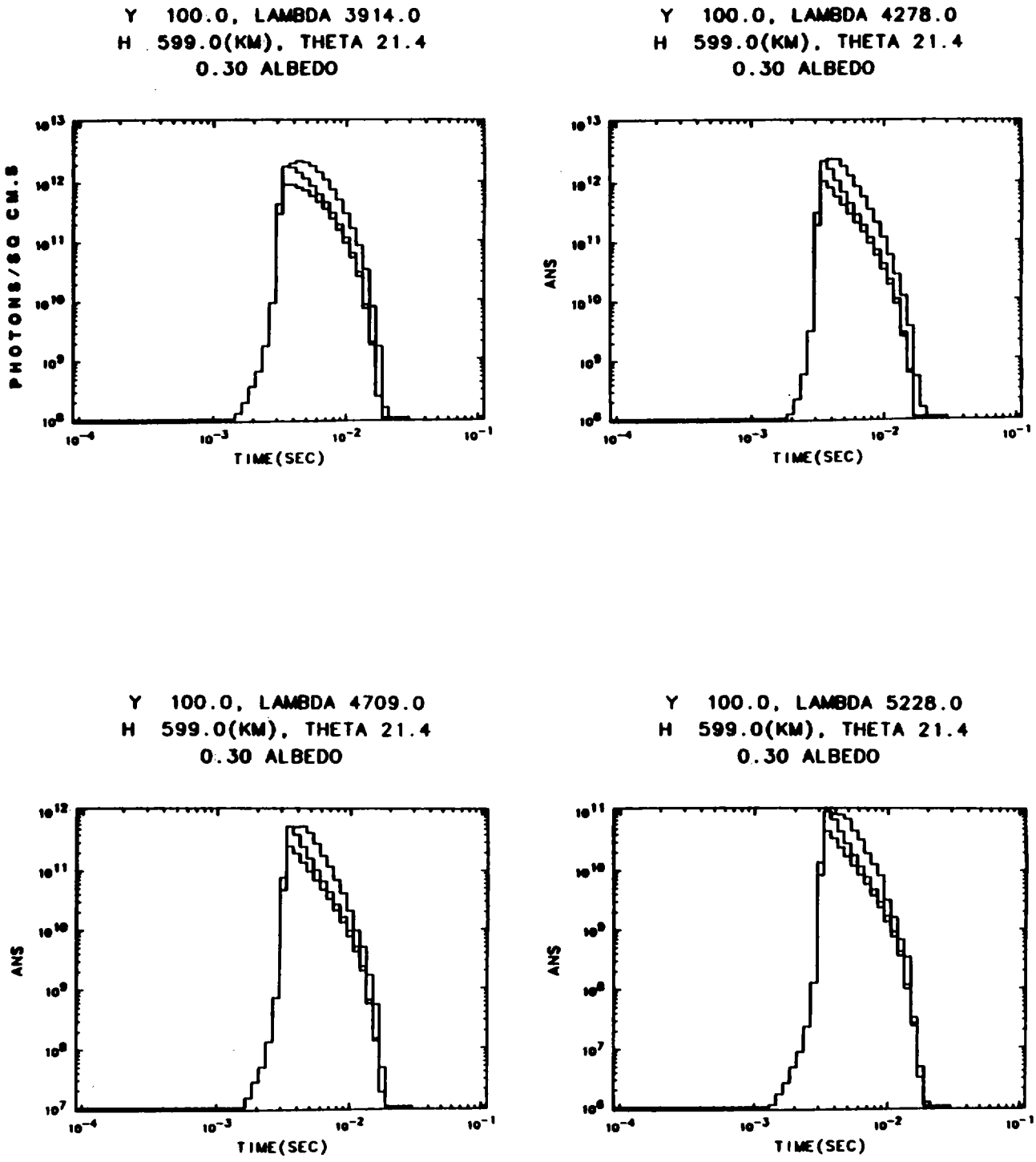

Fig. 32. Similar to Fig. 28, but the burst altitude is 599 km.

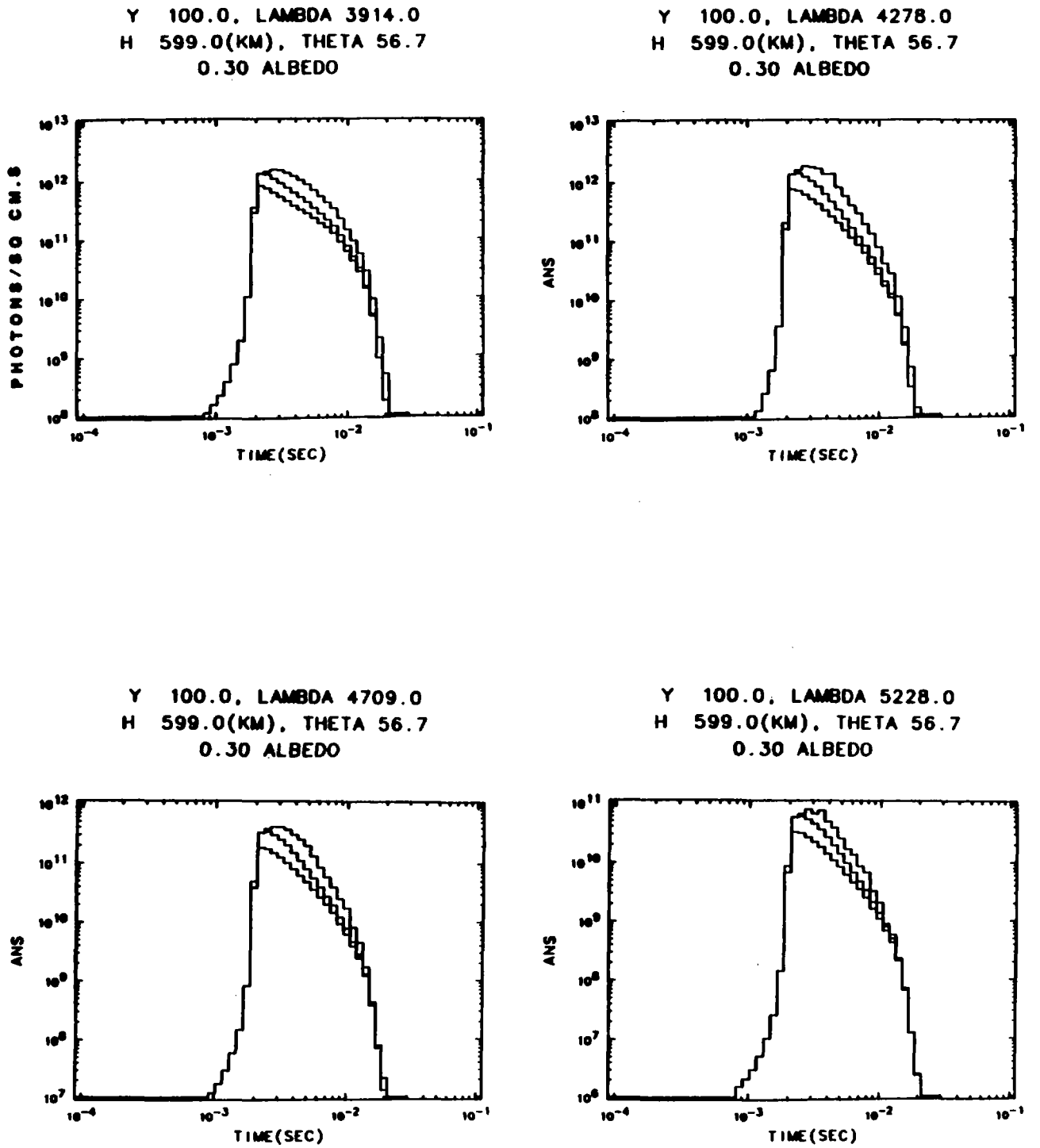

Fig. 33. Similar to Fig. 29, but the burst altitude is 599 km.

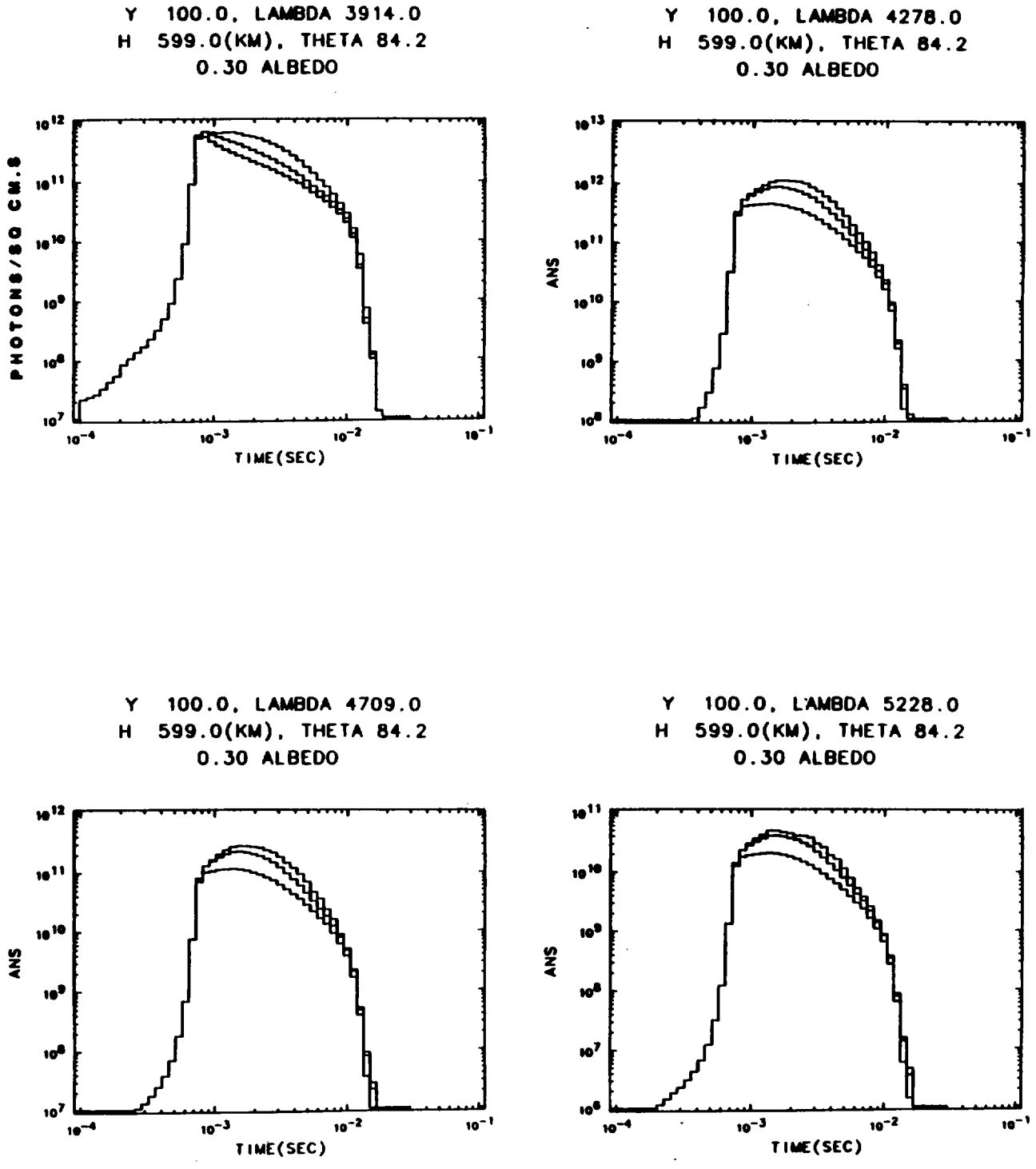

Fig. 34. Similar to Fig. 30, but the burst altitude is 599 km.

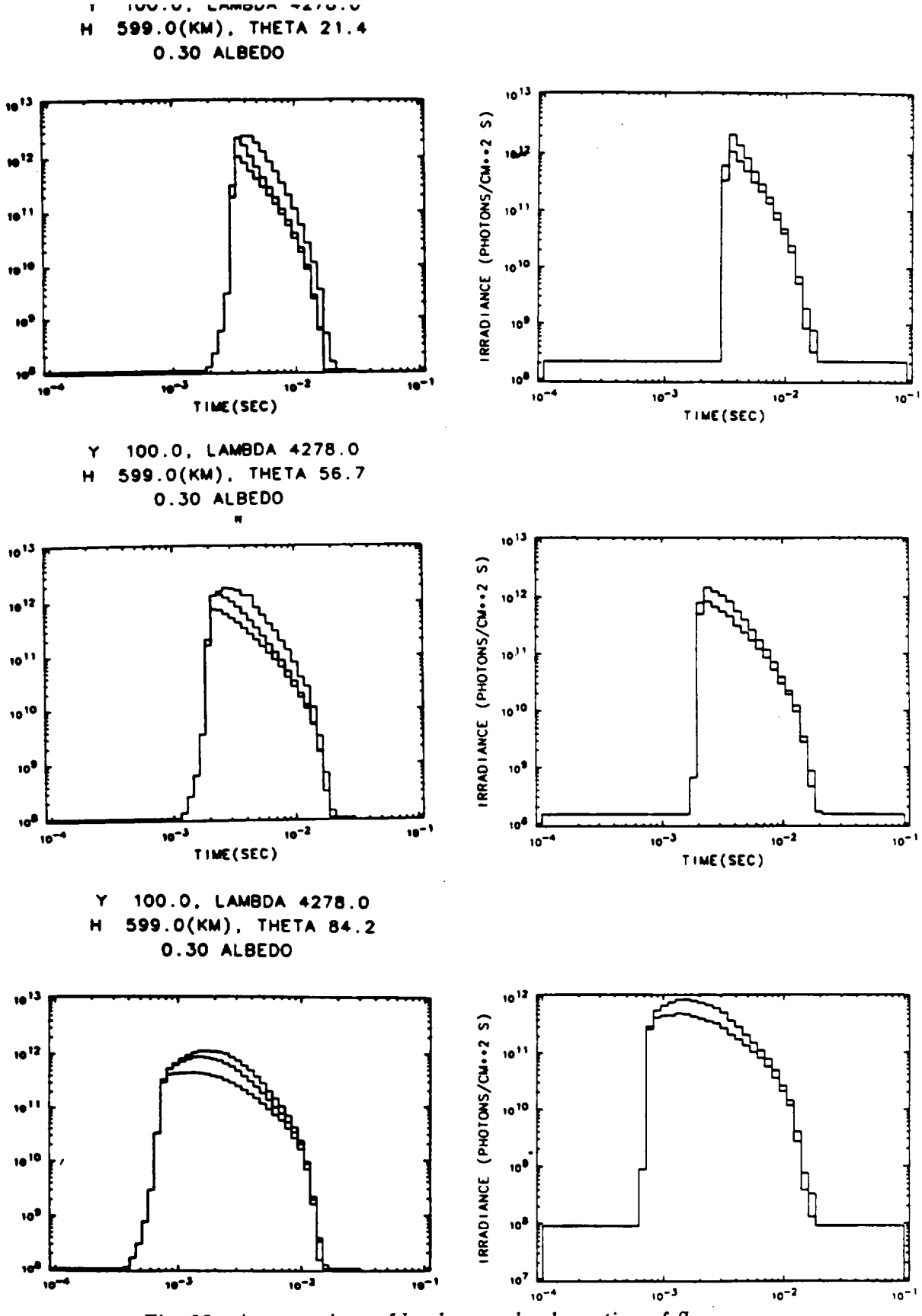

Fig. 35. A comparison of local vs nonlocal creation of fluorescence.

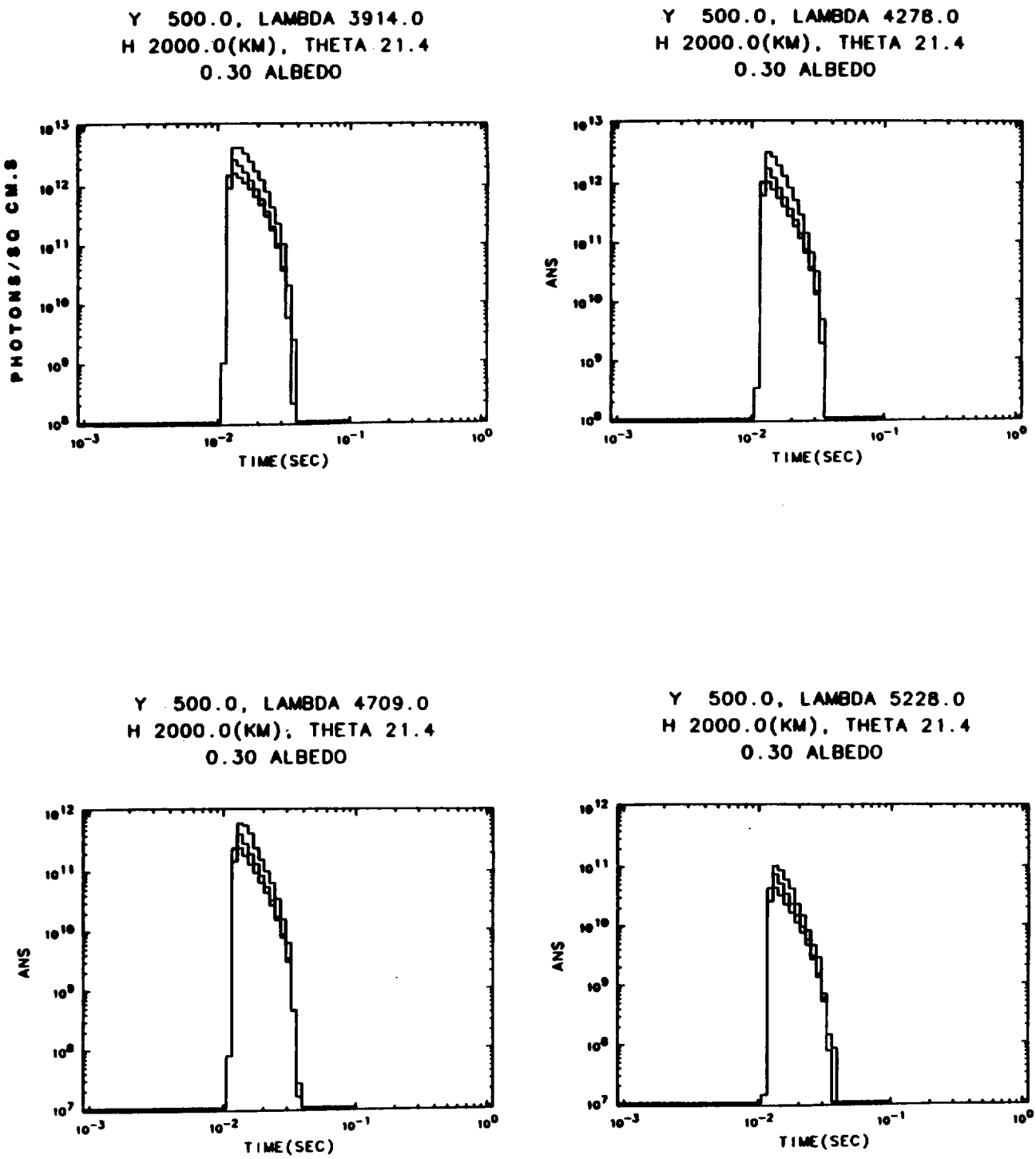

Fig. 36. Similar to Fig. 28, but the burst altitude is 2000 km.

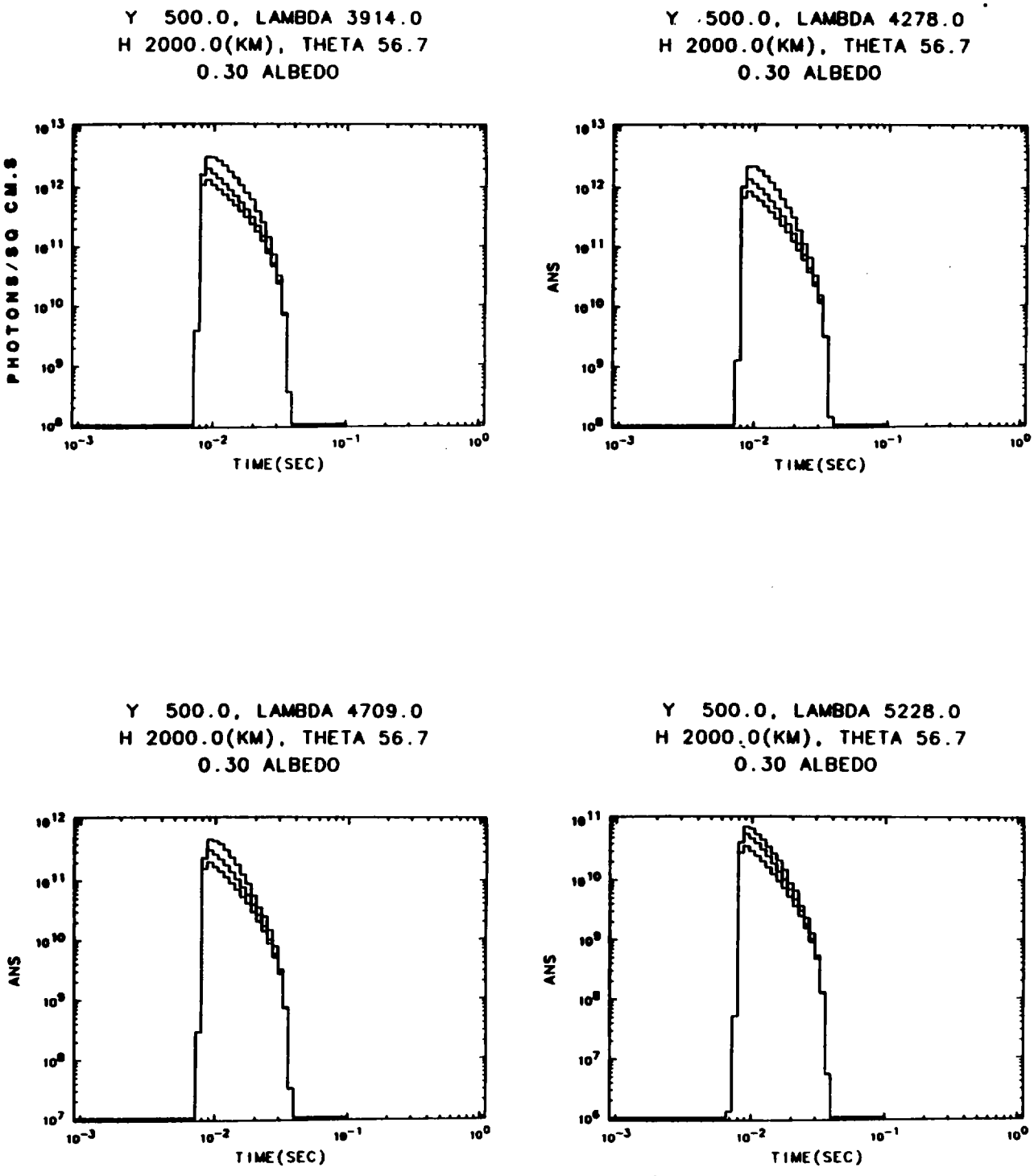

Fig. 37. Similar to Fig. 29, but the burst altitude is 2000 km.

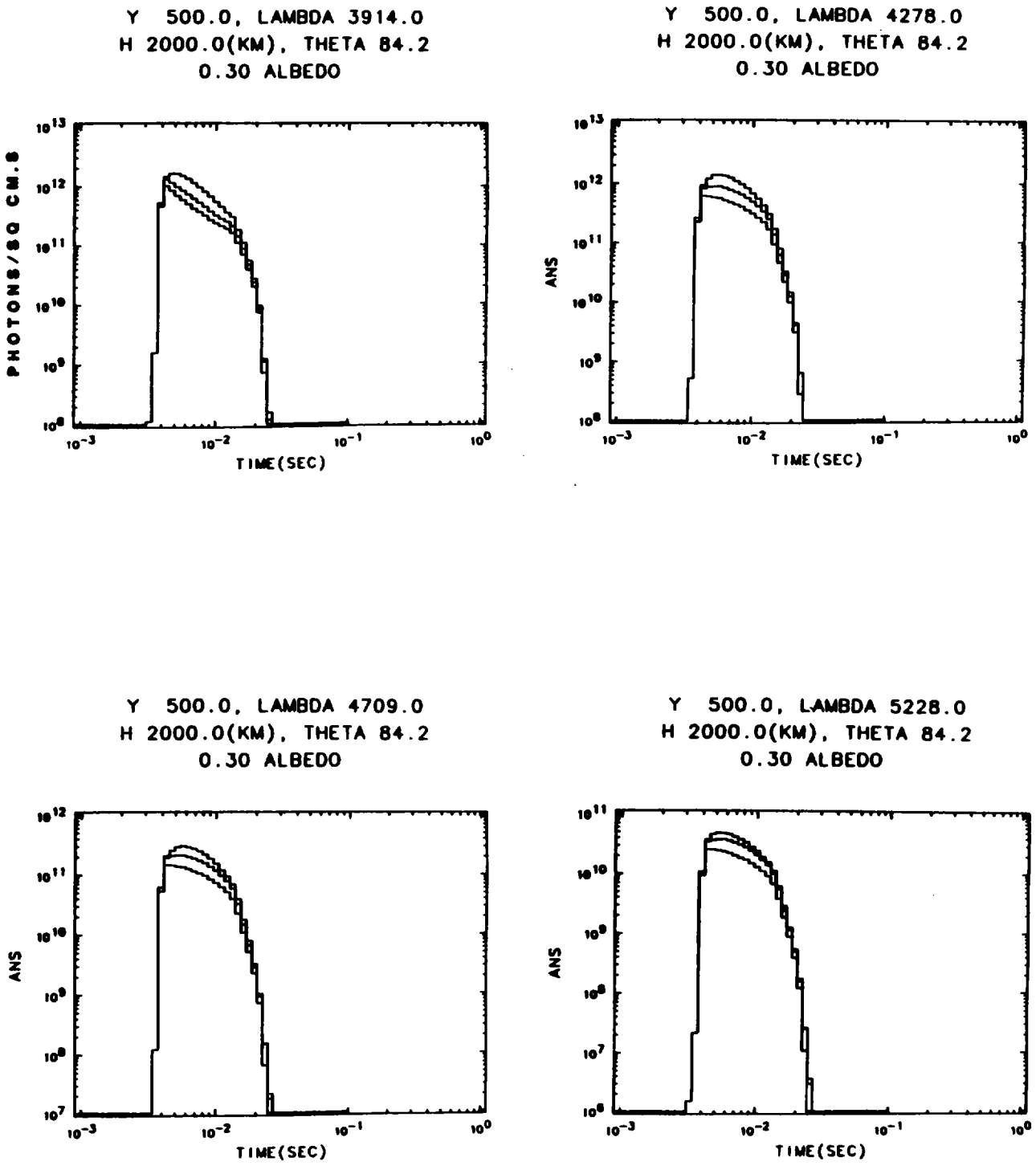

Fig. 38. Similar to Fig. 30, but the burst altitude is 2000 km.

REFERENCES

Albritton, Schmeltekopf, and Zare, *Diatomic Intensity Factors* (Harper and Row, New York, 1972).

Bennett, E. W., and R. F. Holland, "Prompt Air Fluorescence Excited by High Altitude Nuclear Explosions," Los Alamos Scientific Laboratory report LA-3409-MS Supplement (May 1966).

Bennett, R. G., and F. W. Dalby, "Experimental Determination of the Oscillator Strengths of the First Negative Bands of N_2^+, *J. Chem. Phys.* **31**, 434 (1959).

Berger, M. J., and S. M. Seltzer, "Tables of Energy Losses and Ranges of Electrons and Positrons," National Bureau of Standards, NASA report SP-3012 (Office of Technical Services, Department of Commerce, Washington, DC, 1964).

Bortner, M., and J. Baurer, Eds., *Defense Nuclear Agency Reaction Rate Handbook*, DNA 1948H, revision No. 7 (1978).

Briesmeister, J. I., "MCNP—A General Monte Carlo Code for Neutron and Photon Transport," Los Alamos National Laboratory report LA-7396-M, Rev. 2 (September 1986).

Cartwright, D. C., W. R. Pendelton, Jr., and L. D. Weaver, "Auroral Emission of the N_2^+ Meinel Bands," *J. Geophys. Res.* **80**, 651 (1975).

Childs, W. H. J., "Perturbations and Rotation Constants of Some First Negative Nitrogen Bands," *Proc. Roy. Soc.* (London) **137A**, 641 (1932).

Collins, D. G., and M. B. Wells, "Radiation Model Development," Air Force Technical Applications Center report AFTAC-TR-82-166 (1982).

Cospar Working Group IV, *CIRA 1965* (North Holland Publishing Co., Amsterdam, 1965).

Elterman, L., "UV, Visible and IR Attenuation to 50 km, " Air Force Cambridge Research Laboratories report AFCRL-68-0153 (1968).

Fischer, J., "Beiträge zur Theorie der Absorption von Röntgenstrahlen," *Ann. Physik* **8**, 821-850 (1931).

Fox, J. L., and A. Dalgarno, "The Vibrational Distribution of N_2^+ in the Terrestrial Atmosphere," *J. Geophys. Res.* **90**, 7557 (1985).

Gardiner, H. A. B., "Resonance Absorption at Altitudes Above 60 km in N_2^+ First Negative Bands," Air Force Geophysics Laboratory report AFGL-TR-82-0355 (1982).

Gear, C. W., *Numerical Initial Value Problems in Ordinary Differential Equations* (Prentice-Hall, Inc., Englewood Cliffs, New Jersey, 1971).

Gilmore, F. R., "Potential Energy Curves for N_2, NO, O_2, and Corresponding Ions," *J. Quant. Spectrosc. Radiat. Transf.* **5**, 369 (1964).

Glasstone, S., Ed., *The Effects of Nuclear Weapons* (Superintendent of Documents, Washington, DC, 1962).

Green, A., and P. Wyatt, *Atomic and Space Physics* (Addison-Wesley, Inc., Reading, Massachusetts, 1965).

Herzberg, G., *Molecular Spectra and Molecular Structure I: Spectra of Diatomic Molecules* (Van Nostrand Reinhold Co., New York, 1950).

Holland, R. F., and W. B. Maier II, "Study of the $A \rightarrow X$ Transitions in N_2^+ and CO^+," *J. Chem. Phys.* **56**, 5229 (1972); Erratum: **58**, 2672 (1973).

Holstein, T., "Imprisonment of Resonance Radiation in Gases," *Phys. Rev.* **72**, 1212 (1947).

Huber, K. P., and G. Herzberg, *Molecular Spectra and Molecular Structure IV: Constants of Diatomic Molecules* (Van Nostrand Reinhold Co., New York, 1979).

Ivanov and Shcherbakov, *Astrofizika* **1**, 22 (1965).

Jain, D. C., and R. C. Sahni, "Einstein A Coefficients, Oscillator Strengths, and Absolute Band Strengths for the First Negative System, and Franck-Condon Factors for the Second Negative System of N_2^+," *Int. J. Quantum Chem.* **1**, 721 (1967).

Jeunehomme, M., "Oscillator Strengths of the First Negative and Second Positive Systems of Nitrogen," *J. Chem. Phys.* **44**, 2672 (1966).

Leopard, F. O., D. G. Collins, and M. B. Wells, "Monte Carlo Studies to Study the Transport of X-Rays and Fluorescent Light in the Atmosphere," Radiation Research Associates report RRA-T7012 (1970).

Livesay, R. B., "Photon Cross Sections for $10\,\text{eV} \leq E \leq 100\,\text{MeV}$," Radiation Research Associates report RRA-T7506 (1975).

Lofthus, A., and P. H. Krupenie, "The Spectrum of Molecular Nitrogen," *J. Phys. Chem. Ref. Data* **6**, No. 1, 113 (1977).

Maier II, W. B., and R. F. Holland, "Visible and Near Ultraviolet Light Produced by the Radiative Decay of Long-Lived States in a Nitrogen Ion Beam," *J. Chem. Phys.* **59**, 4501 (1973).

Mitchell, K. B., "Fluorescence Efficiencies and Collisional Activation Rates for N_2 and N_2^+ Bands Excited by Soft X-Rays," *J. Chem. Phys.* **53**, 1795 (1970).

Myers, B., and M. Schoonover, "UV Photon and Electron Deposition in the Atmosphere," Science Applications, Inc., report SAI-76-696-LJ, DNA 4068F (1976).

Nicholls, R. W., "Franck-Condon Factors to High Vibrational Quantum Numbers I: N_2 and N_2^+," *J. Res. Nat. Bur. Stand.* **65A**, 451 (1961).

Sauter, F., *Ann. Physik* **11**, 454 (1931).

Shampine, L., and C. W. Gear, "A User's View of Solving Stiff Ordinary Differential Equations," University of Illinois at Urbana-Champaign, Department of Computer Science report UIUCDCS-R-76-829 (1976).

Shemansky, D. E., and A. L. Broadfoot, "Excitation of N_2 and N_2^+ Systems by Electrons," *J. Quant. Spectrosc. Radiat. Transf.* **11**, 1385 (1971).

Skumanich, A, and S. Stone, Los Alamos Scientific Laboratory memorandum (August 1960).

Spencer, L. V., "Energy Dissipation by Fast Electrons," National Bureau of Standards Monograph 1 (Superintendent of Documents, Washington, DC, 1959).

Stanton, P. N., and R. M. St. John, "Electron Excitation of the First Positive Bands of N_2 and of the First Negative and Meinel Bands of N_2^+," *J. Opt. Soc. Am.* **59**, 252 (1969).

"US Standard Atmosphere" (US Government Printing Office, Washington, DC., 1962).

Wallace, L. V., "Photoelectric Intensity Measurements of Molecular Band Systems," Ph.D. Thesis, University of Western Ontario (1954).

Wallace, L. V., and R. W. Nicholls, "The Interpretation of Intensity Distributions in the N_2 Second Positive and N_2^+ First Negative Band Systems," *J. Atmos. Terr. Phys.* **7**, 101 (1955); Erratum: **24**, 749 (1962).

*U.S. GOVERNMENT PRINTING OFFICE 1990-0-573-036/20123

Los Alamos National Laboratory
Los Alamos,New Mexico 87545